PLANAR-FLOW MELT SPINNING: PROCESS DYNAMICS AND DEFECT FORMATION

A Dissertation

Presented to the Faculty of the Graduate School

of Cornell University

in Partial Fulfillment of the Requirements for the Degree of

Doctor of Philosophy

by

Brenton Lee Cox

August 2011

PLANAR-FLOW MELT SPINNING: PROCESS DYNAMICS AND DEFECT FORMATION

Brenton Lee Cox, Ph.D.

Cornell University 2011

The focus of this study is process dynamics and defect formation in planar-flow melt spinning (PFMS), a single-stage metal casting process characterized by rapid solidification and thin product. PFMS is particularly attractive for the manufacture of magnetic materials due to very high cooling rates. However, this technique has seen limited commercial adoption and virtually no portability between alloys due to an incomplete understanding of how cast parameters manifest into final ribbon properties. The ability to predict and control these properties, particularly product thickness, is essential to make a single-stage process viable. In this thesis, several parametric influences on thickness are explored, ranging across many length-scales.

A millimeter-scale periodic thickness variation is characterized, wherein it is established in what parameter range and at what frequency these defects appear. This inspires the study of a simplified capillary/inertia dynamical system, whose stability and dynamics are analyzed. Also, we revisit a larger-scale variation in

thickness, attributed to the expansion of the wheel and subsequent changes in cast-geometry. This study yields a physical model that captures dynamics that were previously accessible only through an empirical fit. Recently acquired equipment and newly developed experimental methodologies allow for a better characterization of some cast parameters, which are described in depth.

Biographical Sketch

The author was born and raised in Northeast Texas. During high school, he moved to Central Florida, and then attended the University of Florida, where he majored in Chemical Engineering. His freshman year, he performed experiments for Kerry Johanson at the Particle Engineering Research Center. He was then awarded an REU fellowship that allowed for research under Jani Matisons at the Ian Wark Research Institute at the University of South Australia in Adelaide, South Australia, Australia. After a year of tutoring Chemistry, Mathematics and Physics at the University Tutoring Center at UF, the author was awarded a University Scholars Research Fellowship and began research for Atul Narang in the Department of Chemical Engineering. He graduated from UF in 2005 with high honors.

In August 2005 he arrived in Ithaca, NY, to begin the Ph.D. program in Chemical Engineering at Cornell University, where he joined Paul Steen's research group. He began his thesis research with the study of capillary phenomena related to droplets before becoming interested in the planar-flow melt spinning process. He defended this thesis on the 21st of April, 2011.

This document is dedicated to my wife, my parents, and all of my other teachers.

Acknowledgements

I would like to thank my advisor, Paul Steen, whose insight, encouragement and critique have made this thesis possible, and hopefully more intelligible. In addition, I would like to thank Abraham Stroock, Steven Weinstein, and Richard Rand for serving on my committee and providing their expertise and insightful critique. I have been supported by the National Science Foundation, with material support from both Alcoa and Hitachi-Metglas, Inc. I would especially like to think Dr. Eric Theisen of Metglas for continued support, advice and discussion, which helped steer my research from the beginning. Much of the work herein is founded on previous work done by Eric and Dr. Cormac Byrne, and both were very generous with their advice.

I would like to thank Michael J. Davis for training me to cast, helping operate the lab initially, and significant research discussions well beyond the expectations of an undergraduate researcher. Anthony Altieri has aided in operating the lab, casting, and advising undergraduate students for several years, and made an occasionally arduous job much more enjoyable. His mathematical acumen ha been invaluable since we began to collaborate, and I am confident that under his leadership, the casting lab will thrive. Undergraduate assistance is a crucial part of operating the lab while simultaneously analyzing the data, and I would like to

thank Mike Davis, Si Chen, Jeffrey Fisher, Bo Hu, Christopher Jakobson, and Brian Carroll for all of their efforts.

Henrik van Lengerich and I joined the Steen group concurrently, and his friendship and tireless curiosity have been invaluable professionally and personally. Other members of the Steen group, especially Dr. Mike Vogel and Dr. Dominik Barz, have provided significant guidance, as well. The Chemical Engineering community at Cornell is a warm, inviting place, and I thank all of the friends I have made, fellow graduate students and professors alike.

Lastly, I would like to thank the three people to whom I owe the most: my parents, for inspiring, encouraging, and supporting me in some way, every day of my life, and my wife, for brightening every day I've known her.

Table of Contents

List of Tables

List of Figures

Chapter 1

Introduction to Planar-Flow Melt Spinning

1.1 Overview

Planar-flow melt spinning (PFMS), also known as single-roll melt spinning or spin casting, is a single-stage continuous casting method known for rapid solidification of thin metal sheets, ribbon or wires. Cast products typically range between 10 μm to 2 mm thick in the dimension normal to the substrate, but may be over 15 cm wide and hundreds of meters long; e.g. a continuous spool of 25 μm thick sheet used for transformer cores weighs over 25 kilograms.

The method, shown schematically in Figs. [1.1(a)] and [1.1(b)], comprises forcing molten metal through a planar orifice onto a nearby moving substrate. The molten metal forms a puddle between the orifice nozzle and the substrate, in

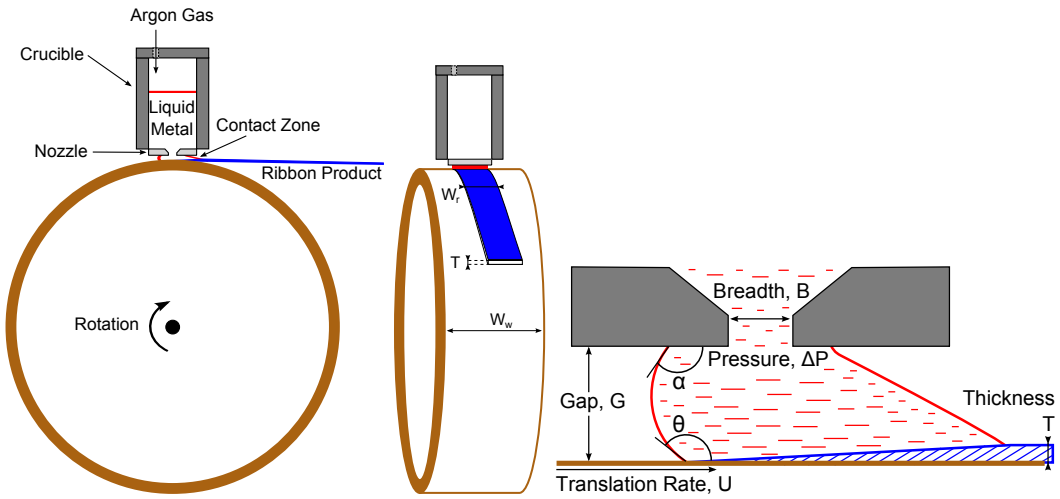

(a) (b) (c)

Figure 1.1: Diagram of the casting apparatus from (a) a side view and (b) a front view. (c) Detailed diagram of contact-zone displaying puddle region.

which the substrate removes sensible and latent heat from the metal, causing it to solidify rapidly. As the metal translates with the substrate, the liquid layer is depleted and then the metal begins to cool. Cooling leads to thermal contraction, which detaches the product from the substrate. Continuous product is formed as long as the puddle, shown in Fig. [1.1(c)], is stable. The puddle region is subject to a variety of instabilities, which generally result in variations in thickness in the product. The primary purpose of this study is to better understand and suppress these instabilities and thus the defects associated with them.

Section [1.2] recapitulates the history of PFMS. Sections [1.2.1]-[1.2.3] review the literature, revealing the physical regimes of PFMS. Section [1.3] briefly describes PFMS at Cornell University. Section [1.4] details the objectives of this study.

1.2 Background

In this study, the metals are aluminum alloys and the substrate is a rotating CuBe wheel. However, a variety of alloy and substrate combinations have been studied since 1975, driven to varying degrees by both the metallurgical advantages of rapid solidification, up to order 10^6 K/s, allowing the production of microcrystalline and amorphous alloys (e.g. Hitachi-Metglas), and the single-stage manufacturing of thin products, which must otherwise be formed to the desired thickness (e.g. Alcoa, RSP Technology). PFMS has seen limited commercialization primarily due to the challenge of stabilizing the puddle region.

Traditional (batch) near-net casting techniques comprise solidfying material into an ingot orders of magnitude larger than the desired thickness that is then formed to specification using a series of hot and cold rolling steps, represented by Fig. [1.2(a)]. Continuous single-stage casting emerged from a patent by Bessemer in 1865, who proposed that liquid metal be fed between two water-cooled rollers to recover a strip of steel, whose thickness would be determined by the spacing of these rollers. The study of continuous casting focused primarily on iron and steel alloys for the next century. However, the first major breakthrough was in 1929, when C.W. Hazelett designed and operated the first commercial continuous casting line, wherein a twin-roll caster and in-line stamping was used to produce lead components for automotive batteries. In 1949, Hazelett invented the first twin-belt caster, but it was not until 2002 when Nucor Steel first commissioned a commercial twin-rolling plant for steel. Through this process, known as Castrip, Nucor can produce steel strip as thin as 1.6 mm at speeds around 1 meter per second. The production speed is limited by the need to hot and cold roll the product in-line.

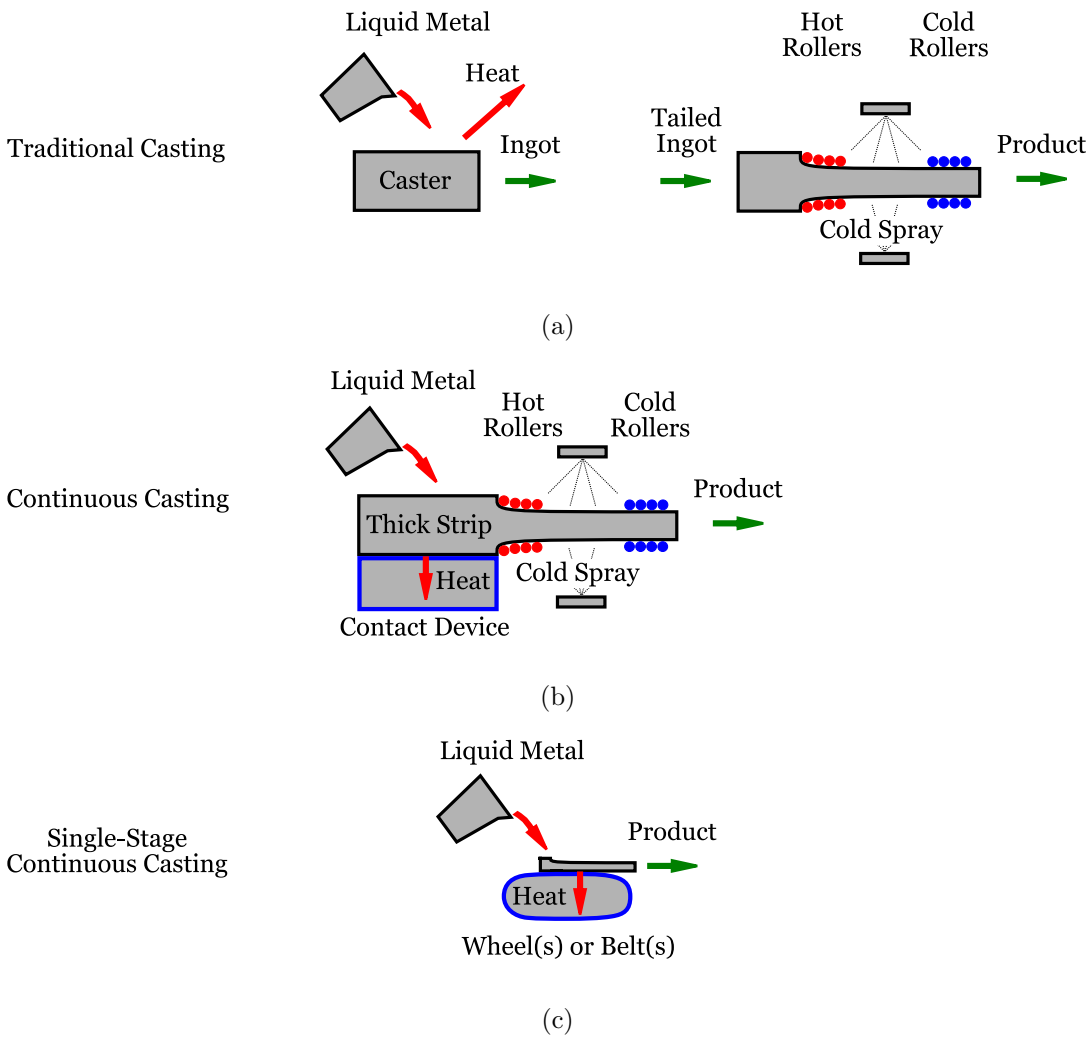

Figure 1.2: Various casting methods.

The multi-stage continuous casting process is represented schematically in Fig. [1.2(b)].

In the mid 1950s, J.L. Hunter introduced twin-roll casting for the production of aluminum Venetian blinds, allowing cast gauges of near 6 mm and eliminating the need for hot rolling[15]. This single-stage casting technology, c.f. Fig. [1.2(c)], through the company now known as FATA Hunter, has supplied over 150 machines to 29 countries. Beginning in the 1960s, the Aluminum Corporation of America (Alcoa) patented new continuous casting techniques specific to aluminum

and magnesium alloys. From this research, which helps support the current study, and acquisitions such as the Kaiser Micro-Mill, which was an important variant of the Hazelett process[15], Alcoa had deployed 22 continuous casters by 1999. Allied Chemical Corporation began producing amorphous metals in 1970, and patented one version of planar-flow melt spinning by the end of the decade[55]. Now known as Hitachi-Metglas, this company has advanced PFMS throughout the past three decades, and is the leading producer of amorphous metal ribbon. However, even for established commercial single-stage casting, and particularly in PFMS, product quality remains a challenge. A major detriment to product quality is failure of the dynamic contact line involved with melt/substrate wetting.

In practice, deterministic models for process dynamics in PFMS are only recently emerging in a field dominated by heuristics, and changing alloys can change everything. Despite this, the physics of PFMS exhibit a wide variety of interesting dynamics, making it an attractive system to model. The following sections describe the physical regimes involved and relevant literature results. These conclusions are drawn based upon the parameters involved in the process, listed in Table [1.1] and the substrate properties given in Table [1.2]. Resulting dimensionless groups and approximate ranges are in Table [1.3]. The abbreviations used throughout the following sections are collected in Table [1.4]. The wide variety of length scales in PFMS are often physically coupled. Some of these length scales, ranging from 100 m to 1 μm, and their physical sources, are listed in Fig. [1.3].

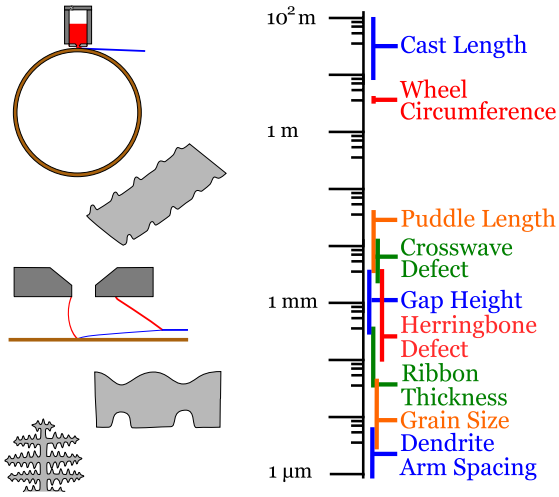

Length Scale	Physical Source
Cast Length	Thermal Expansion
Wheel Circumference	Variation in Gap
Crosswave Defect	Interfacial Dynamics
Puddle Length	Mass Balance in Puddle
Gap Height	Hydrodynamic Resistance
Herringbone Defect	Interfacial Dynamics
Ribbon Thickness	Process Parameters
Ribbon Roughness	Various Defects
Grain Size	Solidification Rate
Dendrite Arm Spacing	Solidification Rate

Figure 1.3: Length scales in PFMS.

1.2.1 Fluid Mechanics

The fluid mechanics of PFMS has been extensively reviewed[72, 41, 42], wherein it is shown that solidification is limited by the rate at which material is supplied to the solidification front (i.e. feed-limited). It is also established that heat and momentum transfer decouple at linear order in PFMS, as their respective lines of flux are almost orthogonal. The order of this decoupling is determined by the so-called solidification parameter $\epsilon = T/L << 1$, the slope of the solidification front[19]. As $\epsilon \to 0$, the heat flow into the solidification front aligns normal to the substrate, and the fluid flows tangent to the substrate. This becomes evident upon examination of the puddle mass balance, $TU = L\bar{V}$, which implies that $\epsilon = \bar{V}/U$, and thus the solidification velocity and substrate translation effects on the fluid are decoupled by scale[42].

As $Re = O(10^5)$, inertia dominates viscous effects, and viscous length scales are very small. However, despite the high Re, the flow is laminarized by the suction boundary layer that feeds solidification, suppressing turbulence and stabilizing the

Process and product parameters		
Process variables		
G	$0.5 - 1.3$ mm	nozzle-wheel gap
U	$4 - 15$ m/s	substrate translation rate
ΔP	≈ 4000 Pa	pressure at nozzle inlet
T	$50 - 200$ μm	ribbon thickness
L	$5 - 20$ mm	puddle length
θ_h	987 K	initial temperature of melt
Puddle geometry		
B	$1.6 - 3$ mm	nozzle breadth
W	$25 - 50$ mm	nozzle width
Feed material properties (Al-7% Si unless otherwise noted)[34]		
η	10^{-3} kg m^{-1}s^{-1}	kinematic viscosity (1033 K)
ρ	2.3 x 10^3 kg m^{-3}	density of liquid metal
ρ_s	2.7 x 10^3 kg m^{-3}	density of solid metal
θ_m	887 K	melting temperature of metal
σ	0.86 N m^{-1}	surface tension of liquid metal
$C_{p,l}$	1080 J kg^{-1}K^{-1}	heat capacity of liquid metal
$C_{p,s}$	938 J kg^{-1}K^{-1}	heat capacity of solid metal
ΔH_f	3.87 x 10^5 J kg^{-1}	latent heat of fusion of metal (0.99% Al)

Table 1.1: Process variables and material parameters.

puddle region. The fluid must turn and accelerate to the substrate velocity, U, stretching the streamlines and creating a scenario in which Bernoulli-type characteristics dominate. In this regime, dynamic pressure is conserved along Bernoulli streamlines throughout the puddle. Recognition of this led to the discovery of a relationship between ribbon thickness and gap height, $T/G \propto \sqrt{\Delta P/U^2}$, and subsequent modeling has refined this scaling and resulted in empirical, predictive models[38, 63, 75].

Substrate parameters		
Substrate geometry		
R_w	30 or 45 cm	radius of wheel
C_w	188 or 283 cm	diameter of wheel
d	1.27 cm	wheel depth
W_w	13.5 cm	wheel width
Substrate material properties (Cu-% Be)		
ρ_w	8.96 x 10^3 kg m^{-3}	density of substrate
$C_{p,w}$	385 J kg^{-1} K^{-1}	heat capacity of substrate
α_L	1.65 x 10^{-5} K^{-1}	coefficient of linear thermal expansion
ν	0.3	Poisson ratio
E	1.28 x 10^5 Pa	Young's modulus

Table 1.2: Substrate geometry and material properties.

In reality, the flow is not irrotational, and previous works have investigated the vorticity transport across the puddle[64]. Vorticity is generated through the history of the flow (e.g. at the inlet due to expansion and flow past a corner, and through transients as the flow is established) and is advected across the control volume, but generation of vorticity in the bulk is negligible. Any vorticity must vanish as the last material solidifies. In [64] it is shown the solidificication boundary adds or removes vorticity from the flow as necessary to satisfy diffusive and advective material flux requirements. It is also shown that a constant vorticity can advect through the bulk unaltered, which led to the approach in [10], wherein a constant vorticity is introduced as a deviation from irrotational flow. This method predicts recirculation in the puddle region, and a relationship between vorticity and detachment of the DSM. However these models have yet to find closure, and thus the study of the relationship between vorticity and puddle stability continues.

Dimensionless groups		
Geometry		
B/G	$1.5-3$	breadth-to-gap ratio
W/G	$25-100$	width-to-gap ratio
Process		
T/G	$0.1-0.3$	thickness-to-gap ratio
$Re \equiv UG/2\eta$	10^5	Reynolds number
$We \equiv \rho U^2 G/2\sigma$	$25-200$	Weber number
$PI \equiv \Delta P G/2\sigma$	$0.4-3$	pressure index
$Ca \equiv \rho\eta U/2\sigma$	10^{-2}	capillary number
$\epsilon \equiv T/L = \bar{V}/U$	10^{-2}	solidification parameter
$(\theta_h - \theta_m)\,/\,(\theta_h - \theta_c)$	0.14	sensible heat fraction
$(\theta_m - \theta_c)\,/\,(\theta_h - \theta_c)$	0.86	latent heat fraction
$Ste_L \equiv C_{p,l}\,(\theta_h - \theta_m)\,/\Delta H_f$	$0.1-0.3$	liquid Stefan number,
$Pe_i \equiv \rho_i C_{p,i} UG/k_i$	10^2	Peclet number in solid (i=s) and liquid (i=l)

Table 1.3: Dimensionless groups and typical values.

Of particular interest is the detachment of the menisci from the slot inlet[42, 5], which experiment has associated with defect formation[14]. This will be discussed in more depth in Section [1.2.3].

1.2.2 Heat Transfer

The melt enters at a temperature above θ_m, and must cool before it can solidify. As the melt quenches, it generates latent heat. The majority of this thermal energy goes into the substrate, causing it to heat up. Heat-up causes thermal stress, and can lead to thermal fracturing of the substrate, both inconvenient and dangerous. An in-depth treatment of the thermal expansion of the wheel can be found in

Abbreviations	
PFMS	planar-flow melt spinning
USM	upstream meniscus
DSM	downstream meniscus
CW	crosswave casting-defect
HB	herringbone casting-defect

Table 1.4: Abbreviations.

Chapter 4.

Because the bulk flow and the solidification are decoupled, the rate at which the substrate can absorb this heat determines the solidification velocity. Despite the high Pe_l, high thermal gradients between the puddle and the substrate result in conduction-dominated heat transport, especially in the solidification region, where the latent heat must be removed. This latent heat represents almost 90 % of the thermal energy that must be absorbed by the substrate. The limiting thermal resistance is the heat transfer between the product and the solid substrate, and there have been many attempts to establish a heat transfer coefficient H_W between these two solids[29, 74, 21, 53, 17, 30, 61, 83, 45, 46]. A brief review of these methods appears in Byrne (2007).

The need for a heat-transfer coefficient arises from the imperfect contact between the product and the wheel. In an idealized case, the solid product would perfectly conform to the substrate and $H_W \to \infty$. However, for this to be the case, the melt would have to completely wet the substrate. Wetting-failure and air-entrainment result in heat-transfer interruptions and lower this heat transfer coefficient. Non-uniform air entrainment results in local variations in H_W and defect formation, the subject of the next section.

1.2.3 Defect Formation

Fluid flow, heat transfer, and interfacial instabilities lead to variations in solidification velocity and product thickness. These variations, known as casting-defects, appear across many length-scales. The longest-scale thickness variation results from thermal expansion of the substrate, which reduces the nozzle-wheel gap, and manifests as a gradual decrease in thickness over the length of the cast. This casting-defect can be avoided, however, if the substrate is cooled sufficiently to remain isothermal. Eccentricities of the wheel change the gap spacing, as well, and appear on the scale of the circumference. Machining (e.g. diamond polishing immediately before casting) can reduce the amplitude of this defect to a desired tolerance, but there can be no perfectly circular substrate.

Shorter-scale defects have been observed, as well. Several previous studies have focused on the parameter windows in which shorter-scale casting-defects appear[18, 60, 14]. Interfacial instabilities are a major source of these defects. The basis of PFMS lies in the suppression of jet instabilities often associated with other melt spinning processes[55], but other sources of instability persist. The puddle is generally free to spread along the nozzle, and the pressure inside the puddle, nozzle geometry and chemistry, and wheel-speed influence the behavior of the puddle meniscus. From the analysis of experimental results by Carpenter & Steen (1992) emerged an empirical window of operability, based on the Weber number $We \equiv \rho U^2/(2\sigma/G)$ and the pressure inside the puddle scaled by capillarity, called the Pressure Index, $PI = \Delta P/(2\sigma/G)$. This window established a regime in which the puddle is robust to "blow-out"- and "pull-under"-related casting-defects, two interfacial instabilities where the upstream meniscus experiences excessive or

insufficient pressure, respectively. However, these results were only quantitative for the material properties and geometry in question. This was refined by theoretical considerations by Byrne, et al (2006)[14], which allowed extensions to different experimental circumstances, informed by similar investigations in extrusion and bead coating[67, 36].

Failure of melt/substrate wetting has also been associated with defect formation. Early methods of suppression reduced the density of the ambient gas in the vicinity of the upstream meniscus, and a brief history of these methods is provided in Liebermann (1986)[47]. These methods aimed to suppress the so-called "gas pocket defect" caused by air entrainment between the metal and substrate. Entrapped gas pockets slow the heat transfer, and thus the local solidification rate is reduced, sometimes perforating the product. The failure of the dynamic contact line is not unique to PFMS, and wetting has been the subject of extensive study as summarized by several reviews[24, 26, 27, 6]. Also of interest are the studies of coating flows, recently the subject of review[84], which often has strong geometric similarities to PFMS. Also, the coating of rough surfaces has lead to the examination of dynamic contact line failure[22].

The sources of some defects have remained mysterious, despite empirically discovered means of suppression. Praisner et al (1995), using a 50/50 Pb-Sn alloy, observed that two casting-defects, termed the "dimpled" and "striated" defects, are suppressed when the liquid Stefan number, $Ste_L = C_p \left(\theta_h - \theta_m\right) / \Delta H_f$ is constrained to the range $0.1 \leq Ste_L \leq 0.3$. Here, C_p, θ_h, θ_m and ΔH_f are the heat capacity of the liquid, the feed temperature of molten liquid, the melting temperature and the heat of fusion, respectively. The investigators proposed that this

suppression may be a balance of reduced surface tension at high temperature and an increased viscosity at low temperature. However, since surface tension and viscosity do not appear in Ste_L, this explanation seems suspect.

More recently, the crosswave defect was associated with oscillations of the upstream meniscus, resulting in entrained rows of pockets in the cross-stream direction, spaced at a wavelength corresponding to this oscillation[12]. Despite the understanding of this defect, methods of its suppression are not well-established. One means of suppression is by casting at low pressures, such that the puddle remains pinned to the inlet nozzle. However, this typically results in the herringbone defect, the focus of Chapter 2.

1.3 PFMS at Cornell University

The planar-flow spin casting apparatus comprises a sealed graphite crucible, surrounded by induction heating coils, seated an adjustable distance above a substrate, represented in Fig. [1.1(a)]. From the bottom of the crucible extends a nozzle, through which molten metal is introduced to the substrate. A nozzle insert containing a slot through which the metal flows during the cast allows the precise machining of the breadth, B, width, W, and other geometric characteristics bounding the fluid flow into the contact zone, as shown in Fig. [1.1(c)]. The substrate is a copper-berrylium wheel whose rate of rotation is set before the cast and then measured throughout the cast by a tachometer, in rotations per minute, which is then reported as a linear velocity, U. The distance between the bottom of the nozzle and the substrate, henceforth referred to as the gap G, is set before

the cast begins. As the cast progresses, heat is absorbed by the wheel causing it to expand. For casts after 2006, the resulting deviation in the substrate is measured by a capacitance gauge and subtracted from the initial gap to provide pointwise gap measurement throughout the cast.

A supply of pressurized Argon is applied, via a pressure regulator, to the inside of the crucible to prevent oxide formation and incease the inlet flow rate. Prior to casting, an initial pressure is applied to evacuate oxygen, water vapor, and other potentially reactive gases, and then the crucible is sealed. This initial pressure remains constant until the cast begins, when the pressure is increased to compensate for the loss of metallostatic head as the metal reservoir is depleted. The reported pressure ΔP is the average of the sum of the applied and hydrostatic pressures experienced at the beginning of the nozzle entry, which remains fairly constant throughout the cast. After a cast, the ribbon product is cut into segments whose width and mass are measured. The average thickness T of each segment is then calculated and temporally associated with other measured casting parameters. For many casts, high speed imaging of the puddle region is performed. Casts prior to the summer of 2008 are imaged using a Kodak EktaPro high-speed video system, after which a Redlake MotionXtra HG-100K is utilized. Video is captured between 3000 and 50,000 fps, with resolutions up to 6 μm per pixel using a 90 mm macro lens. A 150 Watt incandescent bulb shines through the gap between nozzle and wheel toward the camera, backlighting the puddle during a cast. Direct visual observation of the contact zone allows for characterization of the upstream meniscus (USM) as 'unpinned', where the USM contact line may move along the nozzle and maintains a fixed contact angle, or 'pinned', where the USM contact line is constrained on the nozzle slot. Video analysis also allows direct observation of

the motion of both the USM and the downstream meniscus (DSM). More specific descriptions of the experimental apparatus and methodology appear in previous works [18, 12].

1.4 Objectives

In this study we aim to better understand the defects that appear in planar-flow melt spinning.

Chapter 2 focuses on the herringbone casting-defect, a periodic variation in product thickness which appears at a short wavelength during some casts. Data from many casts examining herringbone defect are examined through scaling analysis. Also, a necessary condition for the appearance of herringbone defect is established: a pinned upstream meniscus. Comparison to the crosswave defect, and from this, the operating window is partitioned into expected herringbone and crosswave defect regions. These results lead to speculation about sufficient conditions for the appearance of herringbone defect.

Chapter 3 examines the dynamics of a simplified dynamical system inspired by motion of the upstream meniscus. Two menisci of circular-cap cross section are coupled through a conduit. The stability and finite-amplitude dynamics of center-of-mass motion are examined, and previous studies are used to bound where center-of-mass motion is expected.

In Chapter 4 is a study of the thermal expansion of the substrate. Expansion changes the geometry of the puddle region and effects the product thick-

ness. Previous studies have examined this phenomenon assuming uniform thermal expansion[76], but here a derivation of the thermo-elastic governing equations along with assumptions is presented for the first time. Further, a new model allowing for non-uniform thermal expansion is presented.

Chapter 5 describes in-depth the changes to the experimental apparatus and methodologies made since Spring 2007.

Appendices presenting relevant supplemental information are included. Appendix A summarizes the cast data since Spring 2007. Appendix B examines the dynamics of the downstream meniscus and compares to previous predictions. Appendix C presents the analysis of a gravity-capillary oscillator inspired by the PFMS geometry.

Chapter 2

High-Frequency Defect Formation in Planar-Flow Melt Spinning*

2.1 Introduction

In single-stage casting, process dynamics dictate product properties. In this study, we examine how process parameters influence short-wavelength (or high-frequency) variations in product thickness in the planar-flow melt spinning (PFMS) casting process. PFMS is a single-stage metal casting process characterized by rapid solidification and thin product[55]. Local variations in product thickness can result from disturbances to the fluid flow[76] or to heat transport[12] from the melt. Here, we examine two thickness variations that have been associated with periodic interruptions to the heat-transfer between the product and substrate. These heat-

*Manuscript to be submitted for publication as: B.L. Cox and P.H. Steen, 'Short-wavelength herringbone lines produced in Planar-Flow Melt Spinning'.

transfer interruptions result in cosmetic, mechanical and material variations in the ribbon product, and are typically considered 'defects'. We aim to predict when and where these defects appear in parameter space so that they may be anticipated or avoided. Further, understanding these heat-transfer disturbances presents an opportunity for controlled patterning of the product at short length-scales[11].

Predicting variations in product properties is essential to any single-stage casting process, where post-solidification processing is minimal or non-existent. This is particularly true in PFMS, where ideal conditions result in very high cooling rates, ranging from 10^4 to 10^8 Kelvin per second[43]. A major commercial application of PFMS is the manufacture of magnetic materials where rapid solidification produces amorphous alloys with attractive properties. Rapid solidification allows microcrystalline and amorphous microstructures inaccessible to slower processes[56]. Amorphous molecular configurations provide advantages in a variety of induction-based electromagnetic applications[33], from electro-acoustic surveillance devices[35] to the latest generation of high-efficiency transformer cores[32]. However, unexpected disturbances to heat-transfer reduce the efficacy of PFMS in this setting by slowing solidification.

The PFMS process was patented in 1979[55] and has been subject to significant study. Of particular interest to this study is a review of the process fluid mechanics[72]. An indepth summary of recent PFMS literature appears in Byrne et al (2006a)[12]. Previous studies of defects in PFMS have primarily used scaling analysis to examine the regime in which various defects appear. Empirical bounds have been identified for the surpression of several casting defects[18, 60]. Semi-empirical models have refined some of these bounds by including the physics of

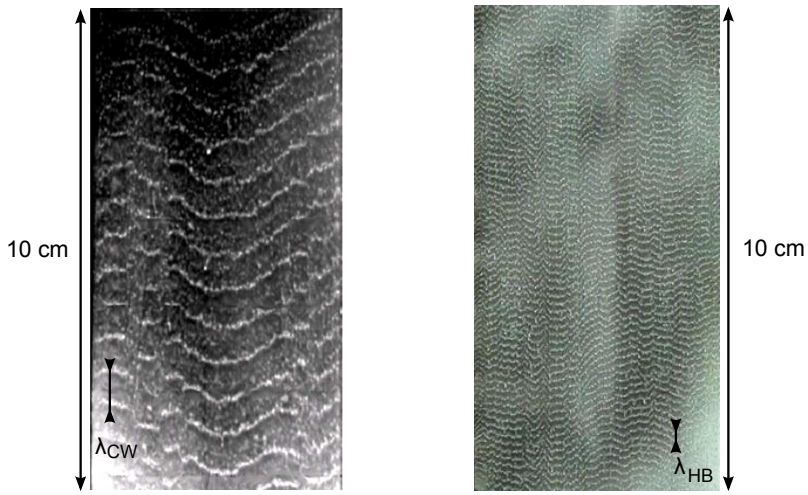

(a) (b)

Figure 2.1: (a) Wheel-side of Al-Si ribbon exhibiting the crosswave defect, where $\lambda_{CW} \approx 7$ mm. (b) Wheel-side of Al-Si ribbon exhibiting the herringbone defect, where $\lambda_{HB} \approx 1.5$ mm. The dimensions of each are 5 cm by 10 cm.

the puddle region[14]. However, some defects have thus far eluded suppression, including a type of casting defect known as crosswave (CW), which was the focus of a recent, in-depth investigation[12]. This defect appears as cross-stream rows of microscopic dimples of depths O(10 μm) on the substrate-side of the ribbon product. These rows appear macroscopically as patterned cross-stream markings, as shown in Fig. [2.1(a)]. This row of dimples impedes the heat-transfer from the melt to the substrate, resulting in troughs on the air-side of the ribbon. These dimples coincide with oscillations of the upstream meniscus (USM) of the melt puddle. This defect is seen in a large region of otherwise stable parameter values.

Similar to CW but shorter in wavelength, the herringbone (HB) defect is the focus of this article. A photograph of typical HB on the wheel-side of a ribbon is shown in Fig. [2.1(b)]. This defect was first reported by Carpenter and Steen[18],

and was also discussed in Praisner, et al[60] and Byrne, et al[12]. In his thesis, EA Theisen presented characteristics of HB observed during the study of CW[75]. Theisen observed that HB frequency has a capillary scaling, and that it appears at a higher frequency than CW. It was also reported that HB coincides with low overpressure. It was speculated that this low overpressure results in a puddle that is pinned at the nozzle slot. Unlike CW, high-speed video (up to 60,000 fps) did not reveal an oscillation of the meniscus coinciding with the HB frequency.

Relevant to PFMS is the study of flows near contact-lines, which have also been subject to significant review[26, 24, 6, 27]. The conditions governing the liquid metal/vapor interfaces determine the nature of the contact-lines, with several possible configurations[71], shown in Fig. [2.2]. The liquid puddle is bounded above, by nozzle through which it is delivered, and below, by the substrate upon which it will solidify, shown in Fig. [2.2(a)]. The interfaces of the puddle are influenced by the geometry of the nozzle, which is 5 cm wide and 1.6 mm in breadth, B, an aspect ratio of almost 50. The upstream meniscus (USM) and downstream meniscus (DSM) are the liquid metal/vapor interfaces into the plane. Fig. [2.2(b)(top)] shows two possible states for the nozzle/puddle/vapor line, CL 1. The contact-line between the puddle and the nozzle may be confined (i.e. pinned, the left schematic) to the inlet slot of the nozzle, e.g. at low pressure. If this contact-line unpins from the slot (i.e. unpinned, the right schematic), it then forms a contact angle as dictated by hydrodynamics and interfacial energies between the metal, the nozzle and the surrounding vapor. At sufficiently high pressure, this contact-line will migrate to the extremes of the nozzle, eventually becoming unstable[14]. Fig. [2.2(b)(bottom)] shows two possible states for the substrate/puddle/vapor contact-line. If the flow at this boundary feeds directly into solidification (i.e.

non-wetting, the left schematic) the contact angle is determined by the ratio of densities between solid and liquid metal[71]. In this case, there is a four-phase contact-line (quad-junction) composed of substrate, solidified metal, liquid metal and surrounding vapor. Alternatively, if some liquid near the contact-line turns up toward the nozzle, the contact-line is a moving contact-line (i.e. wetting, the left schematic). In this case, there will be a three-phase contact-line (tri-junction) between liquid metal, the surrounding vapor and the solid substrate, with a singularity in stress due to a multivalued velocity field[26].

Due to small, highly-curved liquid menisci, interfacial forces play an important role in many of the process dynamics, including casting defects[12]. Despite a high Reynolds number, the rapid solidification of the metal is thought to laminarize the flow[71] and this laminarization, along with capillarity, is credited with stabilizing the puddle region[55]. The geometry of PFMS is similar to many liquid film coating processes. This literature is represented in extensive reviews, e.g. Ruschak (1985) and Weinstein & Ruschak (2004)[68, 84]. Potentially relevant are stability results regarding fluid interfaces in liquid (e.g. slide, slot and sheet) coating[36, 67, 20], and the connections established between interfacial instabilities and defect formation in coating processes[25]. However, unlike PFMS, coating flows are often characterized by low Reynolds number flow. Thus, dynamics of the fluids can be significantly different. In general, many studies of coating flow with similarities to PFMS utilize analytical methods and numerical simulations that explore the flow dynamics and stability. These publications serve as a guide for the study of PFMS.

In Sec. [2.2], we describe two common classes of periodic defects and compare the HB casting defect to these classes. We briefly describe the experimental

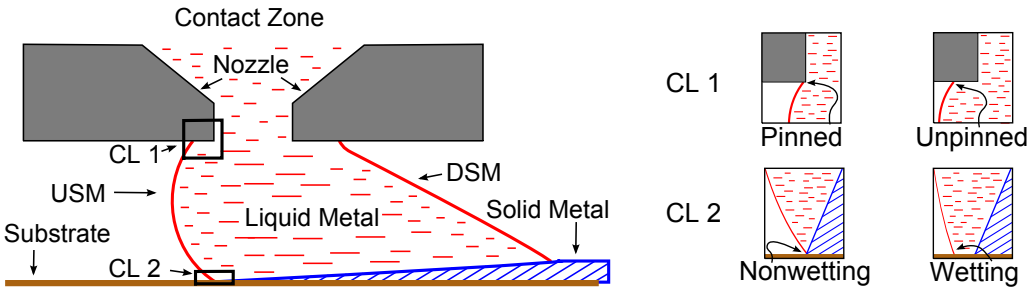

(a) (b)

Figure 2.2: (a) Schematic representation of the puddle indicating different material regions. The vertical dimension is stretched from a typical aspect ratio of 1:10 height to length. A fixed nozzle (grey) and moving substrate (brown) bound a solidifying metal. Liquid metal (red) forms an upstream meniscus (USM) between the nozzle and substrate. a downstream meniscus (DSM) between the nozzle and solidified metal (blue, horizontal shading). The upstream contact-line between the metal and vapor (CL 1) and between the substrate, liquid metal and vapor (CL 2) are indicated and shown in insets. (b) (top) Two possible states of CL 1 wherein (top, left) the contact-line is pinned at the nozzle edge and (top, right) it is free to move along the nozzle face. (bottom) Two possible states of CL 2 wherein (bottom, left) only solid metal contacts the substrate or (bottom, right) liquid metal wets the substrate[71].

methodology in Sec. [2.3]. In Sec. [2.4], we contrast HB with CW. Building on this comparison, Sec. [2.5] uses a dimensional argument to anticipate dimensionless groups involved in defect frequencies. Here, we establish a correlation between cast and material parameters and casting defect frequencies. In Sec. [2.6], we use the observations of Sec. [2.4] to propose a threshold for the transition between the HB and CW casting defects.

2.2 Classification Scheme for Periodic Defects in Continuous Casting

Observed wavelength λ of periodic defect marks or lines that appear in product cast by PFMS can be reported as a frequency f through the relationship to the prescribed substrate velocity U,

$$\lambda f = U. \tag{2.1}$$

Even though λ is the primitive observable, we shall report periodic features as a frequency f in the remainder of this chapter.

Defects can be formed by disturbances of various sources. A useful distinction is whether the defect arises from a lab- or wheel-frame source, or some combination thereof. An example of a lab-frame disturbance source is a jet of ink-droplets of constant frequency f aimed at the wheel. (These produce a wavelength λ proportional to U, according to 2.1.) In contrast, the source could be a wheel-frame variation. For example, suppose the machining of the wheel-surface leaves two high-spots in the circumference. These high-spots result in a periodic low-gap which results in a repeating thickness variation. For such a lab-frame disturbance, the observed f is proportional to U, according to 2.1. Transferring a template from the wheel to the product, as occurs in gravure printing, is another example of a lab-frame source. In summary, assuming a power-law scaling for the dependence of f on U,

$$f \propto U^k, \tag{2.2}$$

the lab-frame source corresponds to $k = 0$ and the substrate-frame source to $k = 1$. The terminology *pulse-transfer* and *template-transfer* have been introduced by Byrne et al (2006a) to bring to mind the ink-jet example for lab-frame and the printing example for substrate-frame sources, respectively. In this paper, we shall expand this classification terminology.

Template-transfer thickness variations are observed in our product. Since the circumference of our typical wheel is of order meters, these defects due to wheel out-of-roundness tend to have wavelengths of many centimeters (a large fraction of the circumference) and are easy to distinguish from the shorter wavelength herringbone and cross-wave patterns. Byrne et al (2006a) demonstrated that the cross-wave is a defect of pulse-transfer origin arising from the oscillations of the molten metal puddle which remains fixed in the lab frame below the nozzle. The puddle oscillates with a natural frequency determined by the inertia of the liquid and the restoring force of surface tension.

The proposed classification scheme is summarized in Table 2.2. *It can be used to classify any periodic defect observed in any continuous casting process.*

A finding of this paper is that the HB defect is neither of pulse- nor template-transfer in origin. In particular, even though the patterns shown in figure 2.1 may appear to differ only in scale, they are of very different physical origins. Indeed, it will be shown that the HB frequency scales with U^2 and, partly on this basis, it will be argued that wheelspeed U influences the HB in an essential hydrodynamical

Formation class	$f \propto U^k$, $\lambda \propto U^{1-k}$
pulse (lab-frame)	$k = 0$
template (wheel-frame)	$k = 1$
hybrid	$k = 2$

Table 2.1: Classes of periodic pattern formation, characterized by $f \propto U^k$ and $\lambda \propto U^{k-1}$.

way (Sec. [2.5]). In contrast, for the CW defect, U influences only as a purely convective effect though the 'change-of-frame'. The fact that $k = 2$ for the HB means that wavelengths get shorter with higher wheelspeeds since $\lambda \propto U^{1-k}$. In some applications, small scale features may be desirable, in which case this scaling-down of feature size with substrate speed may be advantageous.

2.3 Apparatus and Experimental Methods

The PFMS apparatus used in this study comprises a sealed graphite crucible, surrounded by induction heating coils, seated an adjustable distance above a substrate, represented in Fig. [2.3(a)]. From the bottom of the crucible extends a nozzle, through which molten metal is introduced to the substrate. A nozzle insert containing a slot through which the metal flows during the cast allows the precise machining of the breadth, B, width, W, and other geometric characteristics bounding the fluid flow into the contact zone, as shown in Fig. [2.3(b)]. The substrate is a copper-berrylium wheel whose rate of rotation is set before the cast

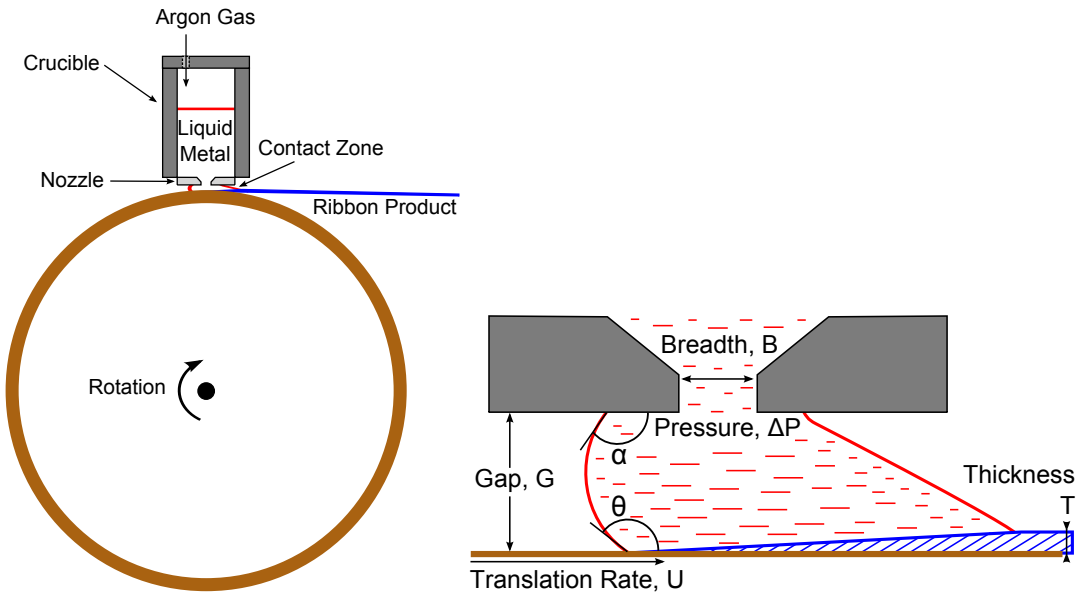

(a) (b)

Figure 2.3: (a) Sketch of the casting process. (b) Enlarged view of the contact-zone showing liquid metal (dashed), solidified metal (hatched), and rim beneath (solid). Metal enters through a nozzle of breadth B and width W in the direction perpendicular to the cross-section. The metal enters with an overhead pressure ΔP. The nozzle is spaced a distance G from a rotating rim, with outer translation rate U. Solidified ribbon exits the contact-zone with thickness T. Upstream contact-lines between the melt, vapor, and nozzle, and between the melt, vapor and substrate, have contact angles of α and θ, respectively.

and then measured throughout the cast by a tachometer, in rotations per minute, which is then reported as a linear velocity, U. The gap G between the bottom of the nozzle and the substrate is set before the cast begins. The gap decreases as the cast progresses. This results from heat being absorbed by the wheel, causing it to expand toward the nozzle[76]. For casts after 2006, the resulting deviation from the initial gap is measured by a capacitance gauge and to provide instantaneous

gap throughout the cast. The G reported is the average gap for these casts.

Pressurized Argon is applied, via a pressure regulator, to the inside of the crucible to prevent oxide formation and incease the inlet flow rate. Prior to casting, an initial pressure is applied to evacuate oxygen, water vapor, and other potentially reactive gases, and after which the crucible is sealed. This initial pressure remains constant until the cast begins, at which time the pressure is ramped to compensate for the loss of hydrostatic head as the metal reservoir is depleted. The reported pressure ΔP is the average of the sum of the applied and hydrostatic pressures experienced at the nozzle inlet (c.f. Fig. [2.3(b)]). After a cast, the ribbon product is cut into segments whose width and mass are measured. The average thickness T of each segment is then calculated and temporally associated with other measured casting parameters. For casts exhibiting a periodic defect, a wavelength λ is calculated by manually counting the cross-stream waves on a segment and dividing by segment length. Typically λ is measured for one out of every ten or fifteen segments of ribbon. Cast average values of data collected for HB casts appear in Appendix [2.9], and CW data is taken from [12].

For many casts, high speed images of the puddle region are recorded. Casts prior to the summer of 2008 use a Kodak EktaPro high-speed video system, while those after use a Redlake MotionXtra HG-100K. Images are captured between 3000 and 50,000 fps, with resolutions up to 6 μm per pixel using a 90 mm macro lens. A 150 Watt incandescent bulb shines through the gap between nozzle and wheel toward the camera, backlighting the puddle during a cast. Direct visual observation of the contact zone allows for characterization of the upstream meniscus (USM) as 'unpinned', where the USM contact-line may move along the nozzle face,

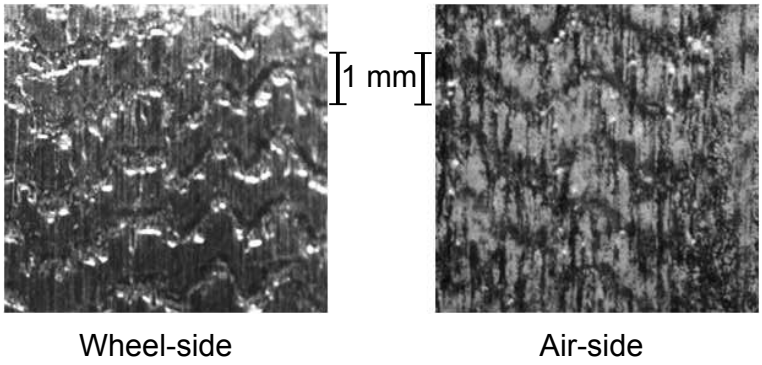

Figure 2.4: Enhanced view of herringbone defect with physical scale.

or 'pinned', where the USM contact-line is constrained on the nozzle slot. Video analysis also allows simultaneous observation of the motion of both the USM and the downstream meniscus (DSM). Further descriptions of the experimental apparatus and methodology appear are available [18, 12].

2.4 Comparison of Herringbone and Crosswave Defects

Here, we examine HB by means of comparison to CW. We observe qualitative similarities and establish the fundamental differences. A more detailed view of HB is shown in Fig. [2.5]. HB is visibly similar to CW, as evident from Fig. [2.1]. However, most striking are the similarities at the microscopic scale. Byrne et al acquired the detailed morphology of ribbon surface exhibiting CW, shown in Fig. [2.5(a)], using a MicroXam Interferometric Profilometer (ADE Phase Shift, Tuscon, AZ)[12]. The morphology of HB was acquired in the same way, shown in Fig. [2.5(b)]. A row of in-line dimples is evident on the wheel-side of both CW and

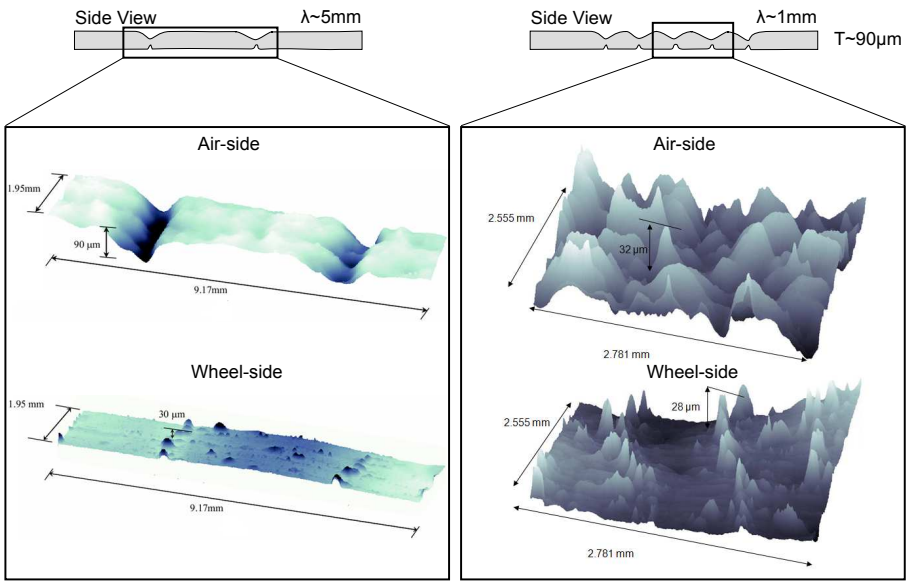

(a) (b)

Figure 2.5: Profile of (a) crosswave defect[12] and (b) herringbone defect as captured through optical profilometry with stretched height to emphasize topography. Note that the scales differ, with (a) encompassing over three times the cast-wise distance of (b). The maximum depth of the wheel-side dimples are 30 μm for CW and 28 μm for HB, whereas the air-side troughs are 90 μm and 32 μm in depth, respectively.

HB. These dimples serve as heat-transfer interruptions and reduce the thickness of the ribbon above them[12, 11]. The reduced thickness results in troughs on the air-side of the ribbon, shown for HB in Fig. [2.4]. This similarity in morphology suggests that the formation mechanisms of CW and HB may be related.

However, HB and CW differ significantly. In most cases, either HB or CW will appear but not both simultaneously. A transition between HB and CW often occurs, as cast parameters are often transient. Much less often, a CW mark will be followed by a few shorter wavelength HB-like marks and then a stretch of HB-free

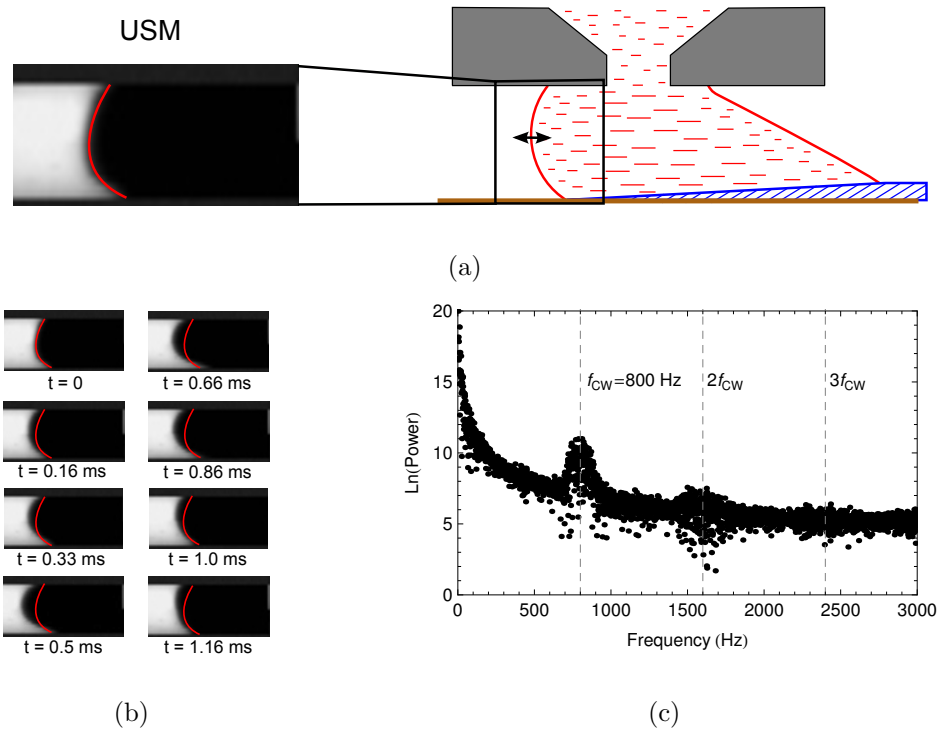

Figure 2.6: (a) Schematic of puddle including high-speed images of USM and DSM. One row of pixels including the USM was analyzed, capturing the horizontal motion of the meniscus in time. An example image is shown (left) with the USM traced in red. (b) Time-sequenced photographs of USM sequenced over 1.16 ms, with the initial meniscus location traced in red. (c) Fast Fourier Transform of the displacement of the USM versus time. Frequency f_{CW} and two harmonics are shown (dashed) for comparison.

ribbon before the next CW mark appears. Based on the rarity of this event, we consider this case anomolous behavior, possibly switching between HB and CW midway between a CW oscillation. Here, we treat CW and HB as distinct, but related phenomena, as supported by literature and observation.

In [12], three criteria are speculated to suppress CW in favor of HB. These criteria were (1) low U or G, (2) nominally pure Al, and (3) a constrained puddle.

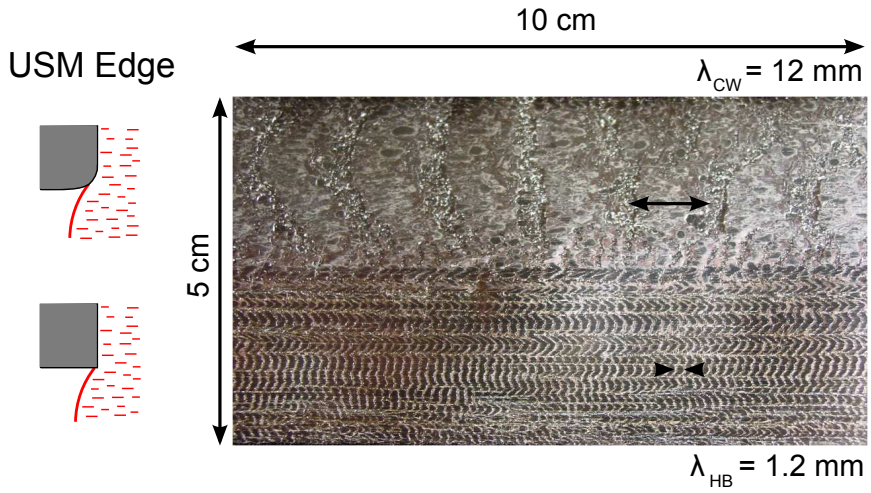

Figure 2.7: Ribbon product from a nozzle where the upper-half (rounded nozzle edge) exhibits crosswave and the lower-half (sharp nozzle edge) shows herringbone. Schematic representations of the corresponding nozzle edges are shown on the left.

Here, we present a single experiment demonstrating that (3) is a necessary condition for CW suppression and HB expression. The nozzle geometry was slightly modified to disallow pinning on half of the nozzle. This resulted in HB on the unmodified (pinned) side and CW on the modified (unpinned) side. This is illustrated in Fig. [2.7], where schematics of the nozzle edge appear to the left of the image of the wheel-side of the image, adjacent to the half of ribbon originating from that half of nozzle. From this observation, we conclude that the puddle must be pinned for HB to appear or unpinned for CW to appear. Thus, at sufficiently high $PI \equiv \Delta P/(2\sigma/G)$, the USM will be unpinned from the nozzle inlet, and CW is expected. Thus the threshold is associated with wetting/pinning, for which we present a semi-empirical model in Sec. [2.6].

In [12], it was found that CW formation corresponds to oscillation of the unconstrained USM[12]. This claim was supported by high-speed video imaging of

the upstream meniscus, which was shown to oscillate at a frequency corresponding to the measured f_{CW}. These findings are reproduced in Fig. [2.6]. A schematic of the puddle, including images of the USM and DSM, is shown in Fig. [2.6(a)]. Motions of the USM, shown through time-sequenced photographs in Fig. [2.6(b)] were analyzed by tracking the motion of the puddle in a single row of pixels on the USM. A Fast Fourier Transform (FFT) of the motion of the USM is shown in Fig. [2.6(c)], where f_{CW} is included for comparison. The same analysis on a column of pixels on the DSM also found motion corresponding to this frequency. These oscillations coincide with the $O(10\mu m)$ air pockets formed from air captured at the substrate/metal interface.

The oscillation of the USM seen in CW is not observed for the constrained USM in HB. Video analysis was performed on casts exhibiting HB, in a similar manner to the analysis presented in Byrne et al (2006a). Higher frame-rates were required for the higher frequency HB, and analysis here was performed on images captured at $50,000$ fps at a resolution of 42 μm per pixel. In Fig. [2.8(a)], a representative high-resolution puddle image is shown, indicating the USM and DSM, and the a row and column of the USM and DSM, respectively. The power spectra of the motions of these menisci are shown in Figs. [2.8(b)] and [2.8(c)]. In contrast to the CW defect, video analysis of the USM does not reveal oscillations corresponding to f_{HB}, but waves appear on the DSM at this frequency. The DSM waves are likely a result of the wheel-side dimples decreasing the solidification rate and influencing the puddle. Thus the DSM waves are a probably a secondary effect of the defect. However, if USM oscillations are the cause of air-entrainment for HB, then the oscillations are not observed in our images. Oscillations would not have been detected if they were either sufficiently small in amplitude or sufficiently

local to the substrate/melt contact-line.

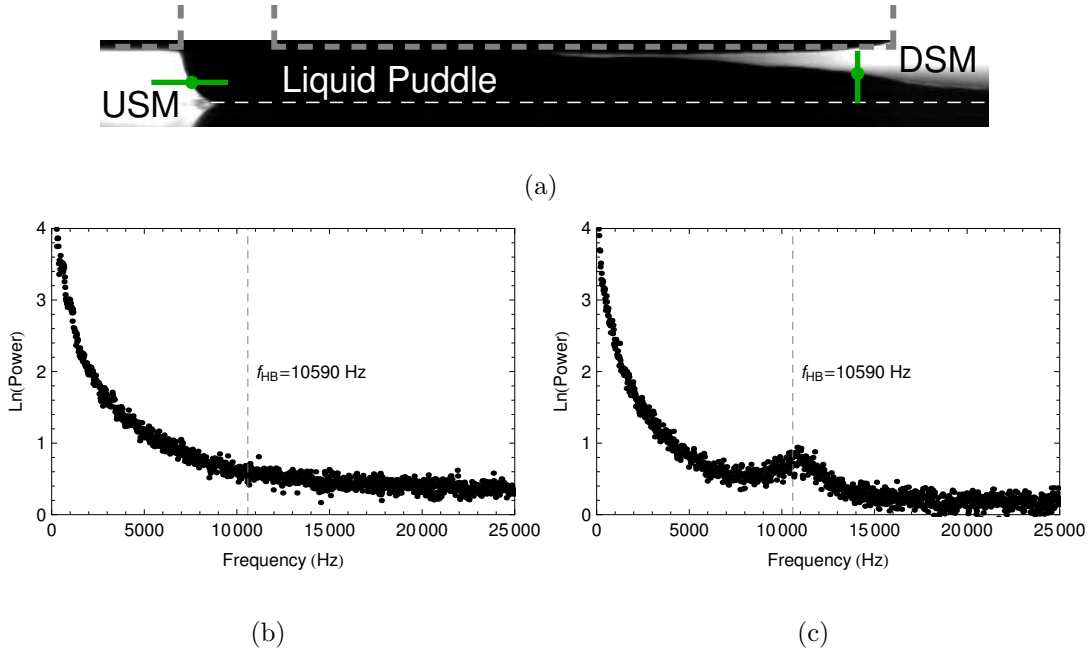

Figure 2.8: (a) Example puddle image captured from high-speed video. One row of pixels including the USM and one column of pixels including the DSM were analyzed, capturing the horizontal and vertical motion of the menisci in time. Fast Fourier transform results of these motions are plotted for (b) the USM and (c) the DSM.

2.5 Dimensional Reasoning

In Sec. [2.2], defect sources were classified by the influence of speed U, a general classification that could apply to any forming process. In this section, we specialize to solidification fed by a high-Reynolds-number flow. We use dimensional reasoning to motivate functional dependencies. The assumption is that five physical variables are involved: frequency f (the observable), speed U or, more generally,

a characteristic velocity u (to be specified), molten metal density ρ, surface tension σ, and gap G. This choice is consistent with an inviscid flow and interfacial instability. Amongst these physical variables, there are dimensional quantities: length, mass and time. Hence, one expects a $5 - 3 = 2$ dimensionless groups to account for the observations. The observable f can be scaled by a capillary time $\tau \equiv (\rho G^3/\sigma)^{1/2}$, leaving one group that must include u. (Note that this scaling of f rules out the trivial template-transfer case.) A natural choice is $We = \rho u^2 G/\sigma$, a Weber number. In summary, one expects function of a single variable $h(x)$ to be sufficient $f\tau = h(We)$. If furthermore, the physically reasonable $h(0) = 0$ is assumed, the functional dependence may be reduced further to a power law. Here, the constant C and exponent k are unknowns,

$$f\tau = C\ We^{k/2}. \tag{2.3}$$

Note that choosing $k = 0$ is consistent with pulse-transfer, Sec[2.2], and makes the specification of u moot. The scaling $f\tau = C$, corresponding to $k = 0$, was reported by [12] with a $C \approx 1.9$ and tested across a range of cast parameters. Using a different casting wheel (2/3 the circumference), we collect CW measurements from a different data set and confirm that We does not influence, as seen in Fig. [2.9]. We find that $C \approx 2$, well within the error bars for the reproducibility of the experiment. This demonstrates that CW formation frequency is a capillary oscillation as discussed in Sec. [2.4].

In contrast, according to Fig. [2.9], HB is seen to be strongly influenced by We. Choosing u to be U, this influence is characterized by an exponent $k = 2$ and

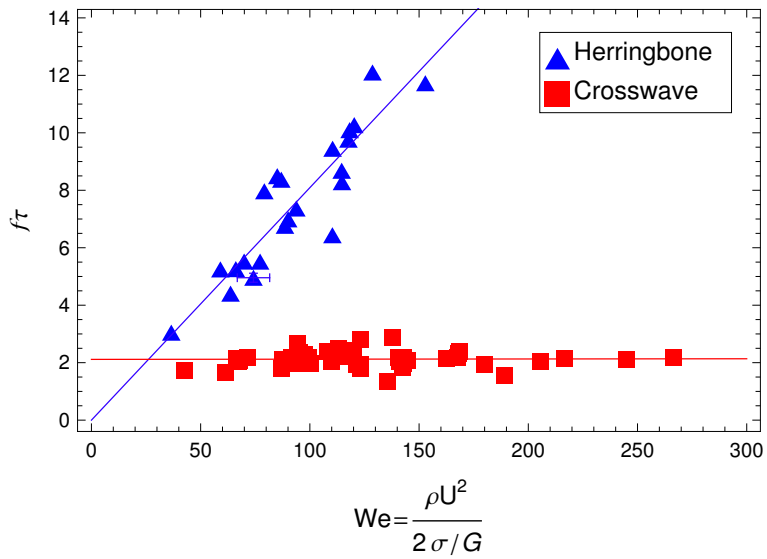

Figure 2.9: Nondimensional defect frequency versus Weber number, with associated by lines of best fit given by $f_{CW}\tau \approx 2$ and $f_{HB}\tau \approx 0.08We$.

a constant $C = 0.08$. There are a number of possible velocity scales u that can be tested for goodness of fit. These include the average flow-velocity through the nozzle of breadth B into the puddle, $u = (T/B)U$, a gap-averaged puddle puddle velocity $u = (T/G)U$, and the average solidification rate is $u = (T/L)U$ where L is the puddle length. The various factors T/B, T/G and T/L have typical values on order of 0.1, 0.1 and 0.01, respectively. All these have been tested using actual (measured) values of T and none show as good a correlation as that with $u = U$. In summary, the HB lines correlate with substrate speed as,

$$f_{HB}\tau = C_{HB}We, \tag{2.4}$$

The appearance of U in We indicates that the important flow contributing inertia to this phenomenon has a velocity $u \propto U$. The source of this U dependence is still a matter of speculation, but it is clear the inertia is interacting with the capillary interface in the case of HB and not CW. It is also clear that pinning

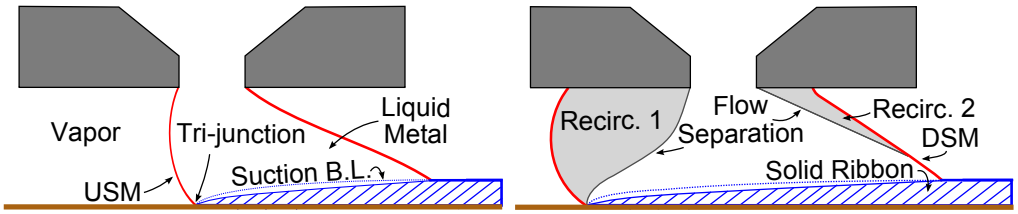

(a) (b)

Figure 2.10: Schematic representation of the puddle when (a) flow is not separated and (b) flow is separated in the upstream and downstream. Separation lines represent the streamlines dividing the flow in the puddle region. Region I is conserved from (a) but Regions II and III (shaded) emerge as distinct hydrodynamic regions.

must somehow be associated with HB formation. We now speculate as to the relationship.

Simulations from the literature [9] suggest that separation occurs upstream once flow is sufficient to unpin the USM. Separated and unseparated cases are sketched for contrast in Figs. [2.10(b)] and [2.10(a)]. These sketches are consistent with the limited observations we have from video analysis of the puddle. For the unpinned USM, the puddle accommodates a flow into an expansion. As a result, an adverse pressure gradient is generated along the nozzle edge. This pressure gradient promotes separation of flow[69] creating an upstream recirculation region which decouples the flow near the USM from the flow into the solidification front. As discussed in Sec[4], rounding the nozzle corned favors an unpinned USM which in turn favors CW over HB. The fact that both CW and HB can be achieved in the same piece of ribbon by varying the nozzle geometry suggests how strong this determinant is. This separation and decoupling may be the reason that CW is not dependent upon We. Any flow adjacent the meniscus must be parallel to the interface for the meniscus to be quasi-stationary. The scaling analysis indicates that

the dominant flow interacting with surface tension in the oscillation is proportional to U. If the meniscus is unpinned no such We dependence appears.

In summary, we argue here that the selection mechanism between the cross-wave and herringbone defects should be the separation of the flow in the upstream region. Other possible reasons such as the coincidence of unpinning and recirculation under the DSM has also been suggested[5], but the influence of the DSM on defect formation is not clear.

2.6 Thresholds for HB Appearance

Previous studies have focused on the parameter windows in which casting defects appear in PFMS [18, 60, 14]. Praisner et al (1995), using a 50/50 Pb-Sn alloy, observed that two casting defects, termed the 'dimpled' and 'striated' defects, are suppressed when the liquid Stefan number, $Ste_L = C_{p,l}\left(T_h - T_m\right)/\Delta H_f$ is constrained to the range $0.1 \leq Ste_L \leq 0.3$. Here, $C_{p,l}$, T_h, T_m and ΔH_f are the heat capacity of the liquid, the feed temperature of molten liquid, the melting temperature and the heat of fusion, respectively. For all casts studied here, Ste_L was approximately 0.2, and dimpled and striated defects were not seen.

An operating window based on We and the Pressure Index, $PI = \Delta P/(2\sigma/G)$, shows where hydrodynamical instabilities are suppressed[18]. These scalings were further refined by Byrne et al (2006b), whose construction we recapitulate here for later use[14]. PI enters from the balance between capillary pressure at the USM and the pressure applied at the inlet to the nozzle region. If PI is too low, the

pressure at the USM cannot be overcome by the inlet pressure, and a stable puddle is not formed. At the extreme, the low PI limit is comparable to a leaky faucet, creating discrete pieces of ribbon as the metal drips out. Until the applied pressure is sufficient, the ribbon contains pin-holes. In contrast, if PI is too high, then the USM will migrate to the furthest edge of the nozzle surface and eventually 'blow-out', developing a Plateau-Rayleigh-type instability in the cross-stream direction. This results in casting defects in the form of streaks. Metal can also pinch off or be ejected from the meniscus, solidifying upstream and then re-entering the puddle, where it remelts and disrupts puddle stability.

Semi-empirical bounds are derived from a mixture of capillary pressure and a loss-coefficient for the turning flow. Laplace pressure, $\sigma\kappa$, where κ is the mean curvature is utilized assuming the USM is a piece of a circle[14]. As in Higgins and Scriven[36] and Ruschak[67], the pressure drop across the meniscus is $\Delta P = (\sigma/G)(cos\alpha + cos\theta)$, where α and θ are the upper (nozzle-side) and lower (substrate-side) contact angles, respectively. A detailed derivation of this window can be found in Appendix [2.10]. The resulting bound is,

$$-\frac{1}{2}cos\theta \leq PI \leq \frac{1}{2}\left(1 - cos\theta\right) + \frac{1}{2}K\left(\frac{T}{G}\right)^2 We. \tag{2.5}$$

The value of θ used in [14], 150 degrees, is used here, and is within the range of contact angles observed in high-speed images. The coefficient K was experimentally fit by Byrne et al (2006b). A conservative and a liberal value of K were reported, 1.8 and 2.8, respectively. The conservative value of K results in the inclusion of more failures but excludes some successes. In plots in this article,

the liberal value $K = 2.8$ will be used, as many successes have been documented outside the $K = 1.8$ line.

With the operating window as an inspiration, we derive a threshold predicting unpinning of the USM from an ideal nozzle. As pinning is a necessary condition for HB (and for suppression of CW), this will serve as a necessary condition for HB expression. The threshold is then derived in the same way as high-pressure limit in the operating window[14], with $\alpha = 2\pi/3$, the angle at which the metal has been observed to wet the nozzle, and K_0, an empirically fit loss-coefficient from the turning flow required for unpinning. This yields,

$$PI \leq \frac{1}{2}\left(\frac{1}{2} - cos\theta\right) + \frac{1}{2}K_0\left(\frac{T}{G}\right)^2 We. \tag{2.6}$$

This threshold unites Byrne et al (2006a) criteria (1) and (3) through We. It is unclear the relationship of criterion (2) to unpinning, but it is possible that the nominally pure Al wets the nozzle insert in some way more conducive to pinning than the Al-Si alloys treated here. In Fig. [2.11], this line is drawn on the typical operating window described above, with $K = 2.8$ and $K_0 = 0.65$. Note that this is a threshold for unpinning. Any abnormality in the nozzle geometry may prevent pinning, as in slot coating[65]. This will result in CW appearing below this line (e.g. the cast shown in Fig. [2.7], which was well below the threshold).

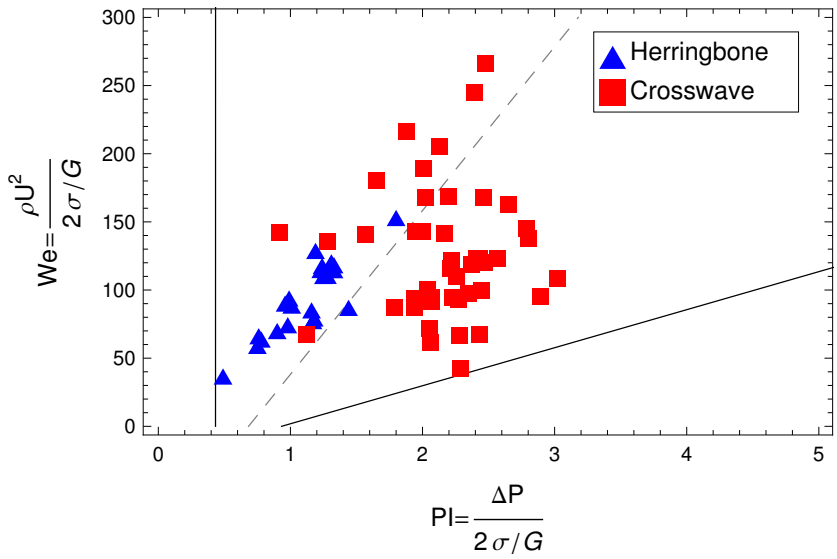

Figure 2.11: A plot of the operating window denoting HB and CW casts. Bounds on PI are plotted from Eq. [2.5]. The depinning limit (dashed line) is given by Eq. [2.6].

2.7 Conclusion

In this study, we report observations of a high-frequency periodic thickness variation known as the herringbone casting defect. This defect is compared to the previously-studied crosswave casting defect. A previous study of CW[12] speculated that some disturbance feeds energy into the upstream puddle region, which then oscillates at its natural frequency, i.e. $f\tau \equiv constant$, comparable to the oscillations of an inviscid sphere[62] or a meniscus above a rectangular channel[3, 54]. In fact, the scaled frequency $f\tau$ is consistent with an entire class of problems where a capillarity-dominated interface bounding an inviscid, quiescent fluid is perturbed from an equilibrium shape. The related herringbone defect appears with a scaled frequency $f_{HB}\tau \propto We$, indicating an inertial contribution from motion of the fluid.

The characteristic velocity which results in this We scaling is U, the substrate velocity. A possible source of inertial influence in HB is discussed. The threshold for transition between CW and HB are predicted based on cast and material parameters using established relationships for puddle stabiliy.

2.8 Acknowledgements

Experiments were supported by NSF Grant Nos. CMMI-0423791 and CMMI-0726813 and NSF sponsored REUs. The authors thank Anthony Altieri, Michael Davis, Si Chen, Jeffrey Fisher, Bo Hu, Chris Jakobson and Brian Carroll for help with experiments and measurements used in this study. Also, we thank Drs. Eric Theisen (Hitachi-Metglas), Steve Weinstein (Rochester Institute of Technology, Rochester, NY, USA) and Warren Smith (University of Birmingham, Birmingham, England, UK) for useful discussions. We thank ALCOA and KBAlloys Inc. for supplying materials for these experiments and Hitachi-Metglas Inc. for high-speed video equipment and software used in this study.

2.9 Experimental Data

The crosswave defect data used in this study appears in Byrne, et al (2006a)[12]. Data relating to the herringbone defect used in this study was collected from experiments performed between 2008 and 2010. This data is summarized here for reference.

Herringbone data								
Cast ID	PI	We	T (mm)	U (m s^{-1})	G (mm)	λ (mm)	f (s^{-1})	τ^{-1} (s^{-1})
ACSU08-01	1.18	79.16	0.12	7.94	0.94	1.47	5358	672.7
FHSU08-01	1.44	86.92	0.11	8.04	1.01	1.59	5065	605.4
FHSU08-02	1.16	85.08	0.12	8.01	1.00	1.54	5213	613.9
FHSU08-07	1.33	118.2	0.11	9.53	0.98	1.52	6417	635.9
FHSU08-08	1.31	120.32	0.10	9.5	1.00	1.52	6270	610.7
FHSU08-11	1.01	88.6	0.09	9.54	0.74	1.45	6594	974.8
FHSU08-12	0.76	66.1	0.07	9.51	0.55	1.21	7861	1495.7
FHSU08-13	0.78	63.69	0.08	9.65	0.52	1.32	7295	1657
FHSU08-14	0.98	74.19	0.09	9.55	0.62	1.53	6281	1267.5
FHSU08-15	0.99	93.81	0.07	9.83	0.73	1.35	7274	987.5
ACSU08-20	0.49	36.56	0.07	9.56	0.30	0.83	11345	3726.1
FHSU08-32	0.96	90.07	0.08	9.72	0.72	1.39	7034	1006.5
ACSU09-02	1.8	152.86	0.15	7.87	1.85	2.81	2859	243.8
ACSU09-03	1.17	77.22	0.12	7.94	0.92	2.08	3811	690.7
ACSU09-04	1.28	110.41	0.11	9.55	0.91	1.43	6695	708.9
ACSU09-05	1.33	114.57	0.10	9.55	0.95	1.65	5782	666.1
ACSU09-17*	0.9	69.91	0.08	7.96	0.45	0.97	8189	1483.7
ACSU09-19	1.19	128.68	0.1	9.62	0.94	1.23	7849.1	648.7
ACSU09-22**	0.75	59.04	0.05	8.01	0.47	0.92	8736.7	1665.2
CJSU09-01*	1.23	114.7	0.13	9.45	0.96	1.76	5355	646.6
CJSU09-05*	1.24	117.67	0.11	9.56	0.97	1.52	6295.9	644.9
CJSU09-06*	1.25	110.32	0.12	9.6	0.91	2.1	4571.4	710.3
All casts Al-7%Si and $*$ - 2.5 – 3.5% Bismuth, $**$ - 3.5% Magnesium								

2.10 Derivation of Operating Window

Higgins and Scriven[36] and Ruschak[67] used simple geometric formulations of Laplace pressure to bound the stability of coating flows. In Byrne et al (2006b)[14], this approach was adapted to PFMS. PI enters from the balance between capillary pressure at the USM and the pressure applied at the inlet to the nozzle region. We enters because a turning-flow loss becomes significant.

If PI is too low, the pressure at the USM cannot be overcome by the inlet pressure, and a stable puddle is not formed. At the extreme, the low PI limit is comparable to a leaky faucet, creating discrete pieces of ribbon as the metal drips out. Until the applied pressure is sufficient, the ribbon contains holes and remains incoherent. This lower bound is derived from the Laplace pressure assuming the USM is a piece of a circle. As in Higgins and Scriven[36] and Ruschak[67], the pressure drop across the meniscus is,

$$\Delta P = \frac{\sigma}{G}\left(cos\alpha + cos\theta\right), \tag{2.7}$$

where α and θ are the upper (nozzle-side) and lower (substrate-side) contact angles, respectively. A diagram of this geometry is shown in Fig. [2.12(a)]. At the lower pressure limit, video observation suggests that the USM is at an angle of $\alpha \equiv \pi/2$, as shown schematically in Fig. [2.12(b)]. This differs slightly from that presented in [14], where it is assumed that $\alpha \equiv \pi$ resulting in a slightly lower PI limit as compared to [14]. The value of $\theta = 150$ degrees is used, consistent with this author's observations.

In contrast, if PI is too high, then the USM will migrate to the furthest edge of the nozzle surface and eventually "blow-out", losing stability in the cross-stream direction. This results in casting defects in the form of streaks, and satellite drops forming, solidifying, and then getting pulled back into the puddle, remelting and disrupting solidification. Here, we assume that the USM is the upper quarter of a circle, i.e. $\alpha = \pi$ and $\theta = 150$, as shown in Fig. [2.12(c)]. Increased We discourages migration. This emerges from an engineering-type empirical pressure loss, given by

$$P_{over} - P_U \equiv 1/2\rho_l K' u^2, \tag{2.8}$$

where K' which is fit from data and u is the average velocity of fluid in the puddle. A mass balance about the puddle allows us to write $\rho_l G u = \rho_s U T$[76]. Substituting for u and identifying We allows us to write the operating window,

$$-\frac{1}{2}cos\theta \leq PI \leq \frac{1}{2}\left(1 - cos\theta\right) + \frac{1}{2}K\left(\frac{T}{G}\right)^2 We. \tag{2.9}$$

The combined coefficient $K = \rho_s^2 K'/\rho_l^2$ must capture the losses of the flow turning in the puddle region and traveling through the constricted gap to the edge of the nozzle insert. Byrne et al (2006b) analyzed 147 casts for "success", meaning coherent ribbon with well defined edges. This resulted in two proposed K values, $K = 1.8$ and $K = 2.8$, depending on the weighting given to successes and failures. The former captures fewer failures but excludes successes. In plots in this article, $K = 2.8$ will be used, as many successes have been documented outside the $K = 1.8$ line.

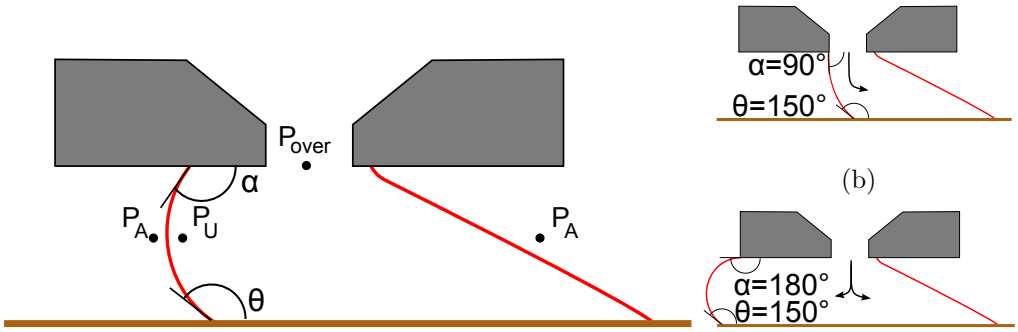

(a) (b) (c)

Figure 2.12: (a) A schematic of the puddle indicating the pressures used in the development of Eq. [2.5]. These pressures are P_{over} at the inlet, P_U inside the meniscus, and P_A in the ambient gas. USM contact angles α and θ are also represented. (b) A schematic representing the low-pressure limit of stability, with $\alpha \equiv 120^{\circ}$and $\theta \equiv 150^{\circ}$. (c) A schematic representing the high-pressure limit of stability, with $\alpha \equiv 180^{\circ}$and $\theta \equiv 150^{\circ}$. The average velocity in the puddle is u.

Chapter 3

Finite-Amplitude Dynamics of Coupled Cylindrical Menisci*

3.1 Introduction

The dynamics of menisci are important to applications as diverse as materials-processing flows[44, 73], microgravity liquid management[50, 85], oil recovery[70], printing processes[86] and respiratory mechanics[31]. Studies of meniscus dynamics are vast in number and reach back at least a century and a half. More recent relevant applications include liquid switches for controllable micro-adhesion [82] and fast-focusing lenses[49]. Static behavior of capillary surfaces has been reviewed [52] with more recent studies of menisci[66]. Static and linear dynamical stability of interfaces overlying inviscid flows are treated in depth by Myshkis et. al. [54].

*Manuscript accepted for publication in Journal of Colloid and Interface Science.

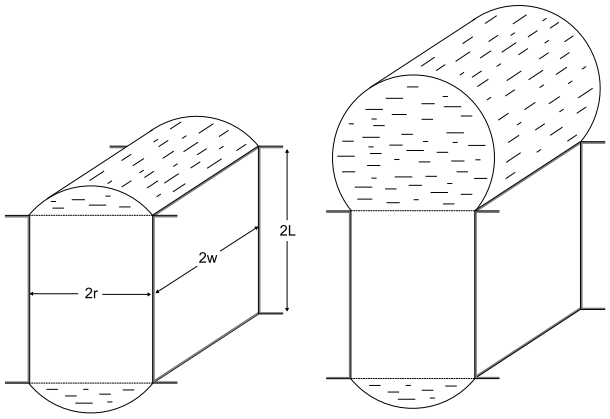

Figure 3.1: Schematic for the coupled cylindrical menisci. Slot halfwidth r, halflength w and halfheight L are indicated.

Application to rapid solidification of metals by planar-flow spin-casting[73] motivates our study. This process is favored for fabricating amorphous magnetic alloys, many of which are important in energy-efficient devices. In the planar-flow process, molten metal fills the gap between two horizontal planes - below is a moving substrate where heat is extracted while above is a nozzle through which the molten metal is fed. A meniscus of molten metal protrudes from the edges. Since the planar-flow region is much wider than long, it is often taken to be two-dimensional. Despite the simplifications, oscillations of the coupled meniscus may be relevant to the solidified product. For example, Rayleigh oscillations of a sphere - an even greater simplification - recently have been correlated with the formation of a defect in the solid product[13]. Observation confirms that, in a typical experiment, Rayleigh vibrations of the upstream meniscus can get frozen into the product as a stream-wise periodic defect. The model of this paper - pinned cylindrical capillary surfaces coupled together through an inviscid liquid - is introduced in this spirit of explaining a similar yet higher-frequency defect.

Two rectangular plates are arranged parallel to one another to make a slot (figure 1). This rectangular slot is overfilled with liquid such that a meniscus forms and pins at each pair of edges. The overfill volume can be low so that the meniscus is lens-like (figure 1, left top and bottom) or high so that it is bead-like (figure 1, right top). Lens-like menisci have planar profiles that are sub-semicircular and bead-like super-semicircular. Overfill volume will be the primary control parameter in our study. For large overfill, there can be a transition between bead-up and bead-down configurations, much as happens for the electroosmotic droplet switch (EODS)[81]. The EODS is an invention that uses an electroosmotic pump to "switch" between the stable states in a bistable energy landscape in the related geometry of coupled spherical-caps, much like a light switch can be flipped between the stable on and off positions.

In the absence of motion, each meniscus shape is a cylindrical-cap as determined by surface area minimization, appropriate when the surface tension force dominates gravity, as assumed here. When in motion, the deformation from cylindrical-cap shape is determined by the balance of surface tension and inertia with possible influence by viscosity. Studies on droplet deformation show that the effect of inertia is small with small Weber number[59], and viscosity can be neglected for large Laplace number[80]. The extent to which these conditions are satisfied for the spherical cap droplet oscillations is discussed in Theisen et al[77]. When inertia and surface tension dominate, the motions of centers-of-mass can be tracked ignoring details of internal flow.

The individual capillary surface of Figure 1 has been referred to variously in the literature as a capillary 'bead', 'ridge', 'fillet', or 'meniscus'. We shall use meniscus

to refer to both lens- and bead-like shapes. Brown and Scriven [8] studied the static stability of a single meniscus to small disturbances. These disturbances are classified as 'polar' and 'transverse' according to their planar and axial wavenumbers, respectively. Brown and Scriven found that the cylindrical lens-like equilibrium shape is stable to infinitesimal disturbances for all lengths. They showed that, for short lens- and bead-like menisci, polar non-zero wavenumber and all transverse disturbances decay. For longer bead-like menisci, transverse disturbances are the most dangerous. Transverse instability is to a Plateau-Rayleigh-like mode. However, pinning at the slot stabilizes the classical PR instability, and there is a widened stability envelope for this slot problem.

Generalizing this result, Bostwick and Steen[7] showed the lens-like state to be stable to a broad class of finite-amplitude disturbances using a Steiner symmetrization technique. This contrasts with the bead-like shape which Brown and Scriven [8] showed to be unstable to constant-pressure disturbances of zero polar wavenumber for short lengths and constant-volume disturbances for long enough menisci.

Coupled liquid/gas interfaces communicate through the intervening liquid and share the same pressure when in equilibrium. The static stability of a system of coupled interfaces, subject to constant system volume, can be determined from the stability of its components. Our approach is based on the work of Poincaré, which has been put into a modern context by Maddocks, and applied to capillary systems by Lowry and Steen although other approaches have been employed [4, 66]. For two coupled menisci, the individual menisci are subject to constant-pressure disturbances so that these become the relevant disturbance class. For

low overfill, both menisci are lens-like and both are stable to constant-pressure disturbances so the (constant-volume) system is stable. For large enough overfill, one meniscus becomes bead-like and the system becomes unstable owing to the zero polar wavenumber instability mentioned above. This instability mode takes on a 'volume-scavenging' nature since a slight pressure imbalance results in the pumping of volume from the meniscus of smaller to that of larger curvature. In summary, according to these stability analyses one expects that the motions of short-enough coupled menisci will remain within the class of cylindrical shapes. This will be taken as an assumption of the following analysis. Furthermore, according to these stability studies and the behavior of the analogous coupled spherical-cap problem [77] – supported by experiment - one expects switching. Study [77] also compares an inviscid model to experiments at $Re = 240$ and finds qualitative agreement of finite-amplitude predictions with observation and that this agreement becomes quantitative when weak dissipation is added to the model.

We find that three types of planar (axially-invariant) motions can occur. For large overfill, depending on initial condition, i) large-amplitude oscillations sweep around the three equilbria in the phase-plane or ii) smaller-amplitude oscillations circle about either of two stable equilibria (centers). For small overfill, there are iii) only oscillations about the globally-stable lens-like equilibrium state (a center).

Sec. [3.2] focuses on the stability and dynamics of sub-critical-length menisci, while the critical meniscus length is discussed in Sec. [3.3].

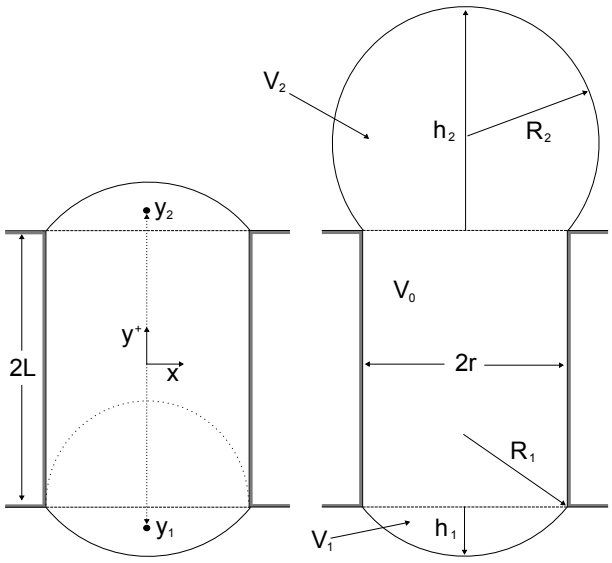

Figure 3.2: Schematic of 2D cylindrical section with labels defined in text. The limit for a negative component volume (dashed half-circle) is indicated.

3.2 2D Stability and Dynamics

3.2.1 Dynamical System

Newton's law is applied to the center-of-mass (COM) of a system of coupled menisci (x_c, y_c) where $x_c = 0$ because of assumed symmetry, shown in Fig. [3.2]. The system COM is related to the component COMs y_i by $V_t y_c = -V_1 y_1 + V_2 y_2$ where V_t is the total volume, and the difference in sign allows for an identical formulation of y_1 and y_2. The slot COM does not enter because it remains at $y = 0$. The component volume V_i can be expressed explicitly in terms of the component height by straightforward calculus[87]. Algebraic manipulation of the result appearing in [87] allows volume to continuously traverse zero as the height changes sign, given by $2\pi V_i = h_i - 1/h_i + (h_i + 1/h_i)^2 \arctan h_i$, where $i = 1,\ 2$. Here, we have scaled all lengths with r, volumes with $\pi r^2 w$ where $2r$ and $2w$ are the dimensions of the

slot opening parallel to the x and z axes, respectively. For example, $V_0 = (4/\pi)L$ with these scalings. Note that L is used for both unscaled and scaled length; the distinction will be clear from context. Later, in the dynamical equations, time will be scaled with $\sqrt{\rho r^3/\sigma}$ which will complete the scalings.

Like volumes, component COMs can be computed explicitly for cylindrical-cap menisci. We first define $\langle yV \rangle_i$, a volume-weighted length measured from the base of each meniscus, $\langle yV \rangle_i \equiv \frac{2}{3\pi} + \frac{1}{2}\left(h_i - h_i^{-1}\right) V_i$. Then, $y_i = \pm L \pm \langle yV \rangle_i / V_i$ where the sign is chosen to correspond with above/below component, as indicated in Fig. [3.2]. Finally, the system COM can now be written,

$$V_t y_c = L\left(V_2 - V_1\right) - \langle yV \rangle_1 + \langle yV \rangle_2. \tag{3.1}$$

Note that the right-hand-side is an explicit function of (h_1, h_2) since formulae for volumes and weighted length in terms of (h_1, h_2) have been provided. Moreover, there is a mapping between (h_1, h_2) and (V_1, V_2) which is nonlinear and everywhere invertible. However, in view of the constraint of total volume, h_1 and h_2 are not independent, which motivates the introduction of a new variable $\theta \equiv V_1 - V_2$ and a parameter $\lambda \equiv V_1 + V_2$. Finally, we give names to the functions $h_1 = H_1(\theta; \lambda)$ and $h_2 = H_2(\theta; \lambda)$ for later use. This formulation admits negative volumes. Negative volumes are concave shapes which are physically reasonable until they intersect the slot wall - the semi-circular shape (dotted) in Fig. [3.2]). This limit gives the constraint $V_i \geq -1/2$ for $i = 1, 2$, enforced for all further calculations. More specifically, any trajectory which violates $\lambda \geq -1$ and $|\theta| \leq \lambda + 1$ will be considered 'unphysical.'

We are now in a position to write down Newton's law for the system. The

balance of linear momentum for a general deforming boundary is available[57] and we specialize to the control-volume that includes both menisci and the channel. The force on the bottom and top slot openings is given by the pressures there which can be obtained via the Young-Laplace law, knowing that the radius of curvature R_i of each component, $2R_i = h_i + 1/h_i$. With this, the governing equation can be written,

$$\frac{d}{dt}\left[A(\theta;\lambda,L)\frac{d\theta}{dt}\right] + C\left(\theta;\lambda,L\right) = 0, \tag{3.2}$$

where

$$A\left(\theta;\lambda,L\right) = L + \frac{1}{2}\sum_{i=1}^{2}\left[\frac{3}{2}\left(H_i - H_i^{-1}\right) + \frac{\arctan(H_i)}{1 + \left(H_i - H_i^{-1}\right)\arctan(H_i)}\right]$$

and

$$C(\theta;\lambda,L) = \frac{4}{\pi}\left[\frac{(H_1 - H_2)(1 - H_1H_2)}{(1 + H_1^2)(1 + H_2^2)}\right].$$

The rate of volume redistribution is $d\theta/dt$ is multiplied by A which gives the influence of tube length and cap geometry on the inertia. The parameter L appears only in the term A, increasing the inertia of the system as it increases. The function C represents the restoring force. Static equilibria correspond to $C = 0$.

The system undergoes a bifurcation from one to three equilibria as the total volume λ traverses unity, corresponding to a shift from a single to double-welled

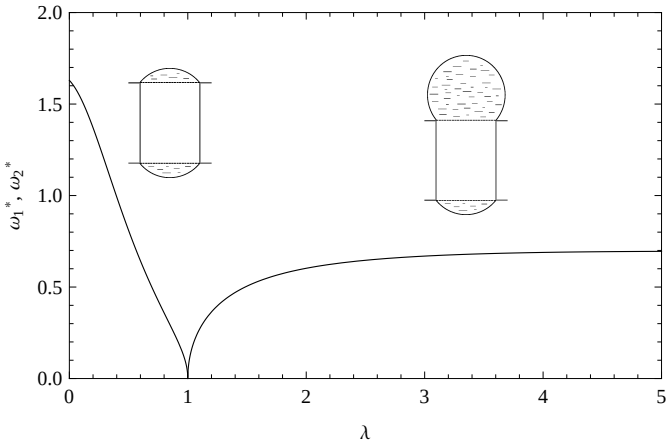

Figure 3.3: Frequencies of linear vibration for the case of cylindrical menisci, ω_1^* for lens-like $\lambda < 1$ and ω_2^* for bead-lens $\lambda > 1$ equilibria.

potential function. The location of this bifurcation corresponds to the volume necessary for the menisci to comprise a cylinder of radius r and length $2w$. The symmetric state $H_1 = H_2$, i.e. $\theta \equiv 0$, is stable for $\lambda < 1$, bifurcating into the two-member family of anti-symmetric states $H_1 H_2 = 1$ for $\lambda > 1$, a pitchfork bifurcation characterized by two equilibrium branches:

$$\begin{aligned} &Branch\ 1\ (H_1 = H_2) : \theta_1^* \equiv 0 \text{ for all } \lambda, and \\ &Branch\ 2\ (H_1 H_2 = 1) : \theta_2^* = \pm \frac{4\lambda}{\pi} \left[\frac{\sqrt{\lambda - 1}}{2\lambda} \right. \\ &\qquad \left. + \arctan\left(\sqrt{\lambda} + \sqrt{\lambda - 1}\right) - \frac{\pi}{4} \right] \text{for } \lambda \geq 1. \end{aligned}$$

Linearization of Eq. [3.2] about each steady state yields the equation for a harmonic oscillator, whose frequency of oscillation corresponds to the frequency of the menisci oscillations in response to infinitesimal disturbances. Along equilibrium branch 1, while λ¡ 1, the eigenvalues are a purely imaginary conjugate pair

of frequency ω_1^*. Letting $y \equiv H_1 = H_2$,

$$\omega_1^{*2} = -\frac{v}{u^3}\left[L + \frac{3}{2}v + \left(3v^2 + 6vL + 1\right)\arctan y\right]^{-1}, \tag{3.3}$$

where $2u = y + y^{-1}$ and $2v = y - y^{-1}$, and u and v may be related to λ by $\lambda = \frac{1}{\pi}\left(v + 2u^2 \arctan y\right)$.

For $\lambda > 1$ the eigenvalues $\pm\gamma_1^*$ are real and given by $\pm\gamma_1^{*2} \equiv \omega_1^{*2}$. Along Equilibrium Branch 2, $\lambda > 1$ and the menisci are asymmetric (one small, one large), and the eigenvalues are purely imaginary. The frequency $\pm\omega_2^*$ associated with the upper segment of Equilibrium Branch 2 may be obtained by now letting $y \equiv H_1 = H_2^{-1}$, yielding,

$$\omega_2^{*2} = \frac{v^2}{u^3}\Bigg[1 + \frac{4L}{\pi}\left(1 - 2v\arctan y^{-1}\right)\left(1 + 2v\arctan y\right)\Bigg]^{-1}, \tag{3.4}$$

where u and v are defined as before, and y and λ are related by $4\lambda = (y + 1/y)^2$. Restricting $y < 1$ and replacing y with $1/y$ recovers the frequency along the lower segment of Equilibrium Branch 2. Note that at $\lambda = 1$, i.e. $y = 1$, the system has a double-zero eigenvalue toward which both ω_1 and ω_2 branches approach as $\lambda \to 1$ from 0 and ∞, respectively, as shown in Fig. [3.3].

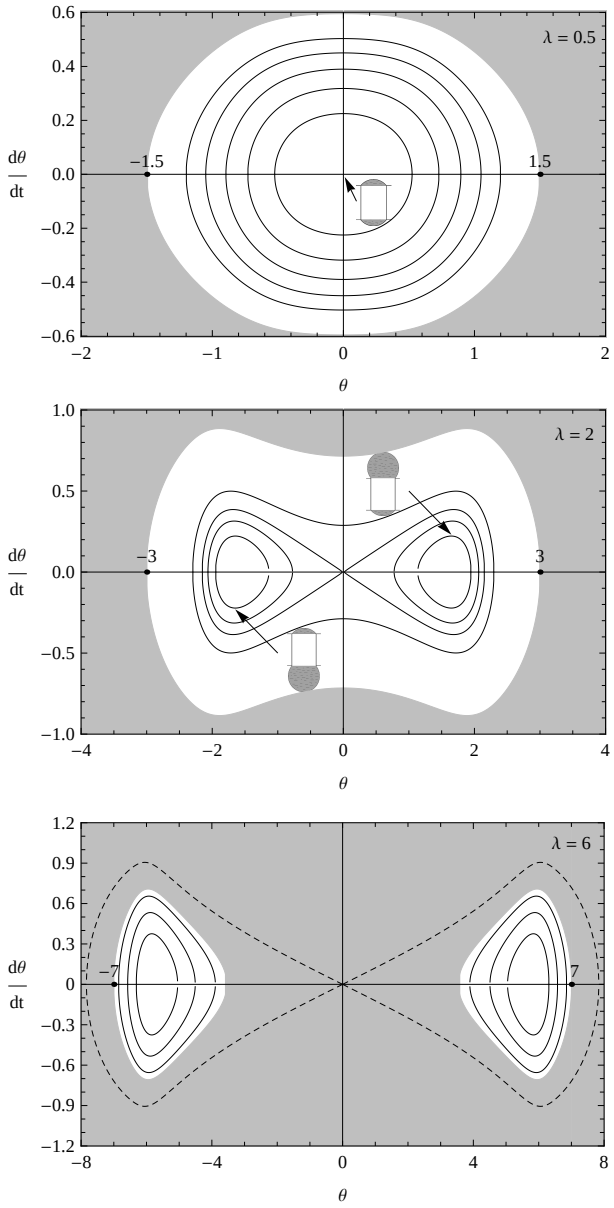

Figure 3.4: Phase portraits for coupled cylindrical menisci, for $\lambda = 0.5$, $\lambda = 2$, and $\lambda = 6$ (top to bottom). Unphysical phase-space is shaded, and the physical limits for θ^+ and θ^- are marked. The separatrix of $\lambda = 6$ (dashed), although unphysical, is shown for clarity.

3.2.2 Motions on the Phase-Plane

The phase portraits and the periods of corresponding orbits can be obtained from the first-integral of the system, which follows directly from Eq. [3.2],

$$\frac{1}{2}\left(A(\theta;\lambda)\frac{d\theta}{dt}\right)^2 + U(\theta;\lambda) = \text{constant} \equiv E, \tag{3.5}$$

where $U(\theta;\lambda)$ is obtained by quadrature,

$$U(\theta;\lambda) = \int_0^\theta A(s;\lambda)C(s;\lambda)ds. \tag{3.6}$$

Here, $U(\theta;\lambda)$ is the potential energy function, single or double-welled for $\lambda < 1$ or $\lambda > 1$, respectively, and is even about $\theta = 0$, analogous to the undamped Duffing equation. Physically, this system is comparable to a nonlinear spring with restoring force $\partial U/\partial\theta$[78], and analysis can be performed on the level curves of the energy[2]. Eq. [3.5] may then be solved for $d\theta/dt$, allowing the generation of the phase planes in Fig. [3.4]. Regions of the phase-plane with trajectories that have unphysical menisci $|\theta| \leq \lambda + 1$ are shaded. When λ is greater than approximately 4.28, the separatrix is unphysical.

Separating θ and t delivers the period of oscillation for an orbit corresponding to an energy E,

$$T = \sqrt{2}\int_{\theta^-}^{\theta^+} \frac{A(\theta;\lambda)d\theta}{\sqrt{E - U(\theta;\lambda)}}. \tag{3.7}$$

Here θ^- and θ^+ are the minimum and maximum deviation from the equilibrium value θ^* along the closed trajectory in the phase plane, where $\theta^- < \theta^* < \theta^+$. For all oscillations where $\lambda < 1$ and for the motions outside of the separatrix where $\lambda > 1$, the orbits are symmetric about $\theta = 0$, $\theta^- = -\theta^+ = \theta^m$, further simplifying Eq. [3.7].

3.2.3 Finite-Amplitude Disturbances

The period of oscillation for finite amplitude disturbances is given by Eq. [3.7]. For values of $\lambda < 1$, oscillations follow elliptical orbits symmetric about $\theta = 0$, each of which has a corresponding frequency as a function of total energy and total volume. In other words, for a given $\lambda < 1$, each orbit may be uniquely characterized by total energy, $E = U(\theta^{max}; \lambda)$ where $\theta^{max} \equiv \theta^+ = -\theta^-$ is the maximum deviation from $\theta = 0$ achieved by that orbit (c.f. Fig. [3.5]). For $\lambda > 1$, a double-well potential exists and there are three qualitatively different types of oscillations: those confined within one of the energy wells, where either $0 < \theta^- < \theta^+$ or $\theta^- < \theta^+ < 0$; those along the separatrix, i.e. the orbit containing the origin; or those outside the separatrix, where $\theta^+ > 0 > \theta^-$. The latter type of oscillations are symmetric about $\theta = 0$, and here again each orbit may be uniquely characterized by the total energy, $E = U(\theta^{max}; \lambda)$. However, for the double-well, each energy level corresponds to two orbits, one confined to each energy well. In these cases, θ remains in either the positive or negative half-plane for the entirity of an orbit[78]. In either case, orbits containing any unphysical θ are omitted.

Numerical integration (performed here by the Gauss-Kronrod method as fea-

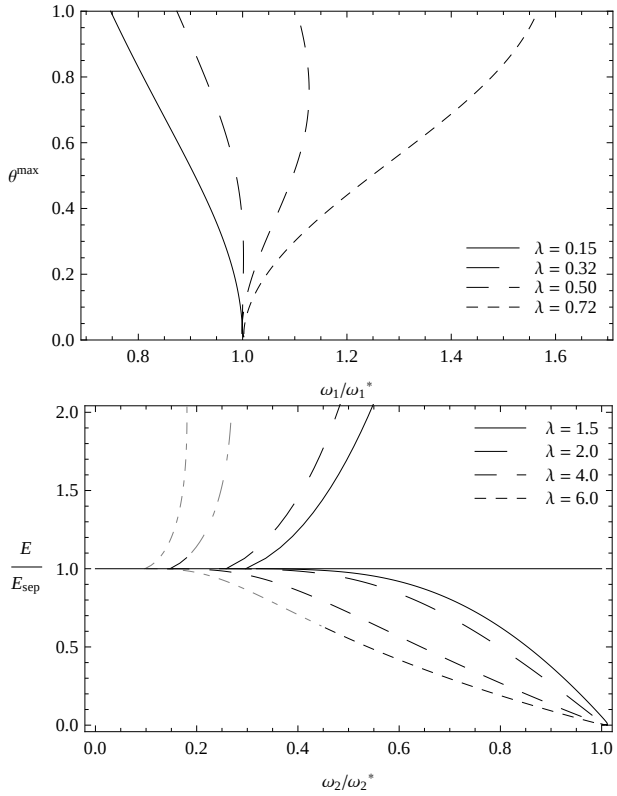

Figure 3.5: Response of frequency to (top) amplitude of disturbance for several values of $\lambda < 1$; (bottom) energy of disturbance for several values of $\lambda > 1$. Note that for $\lambda = 4$ and $\lambda = 6$, these calculations become unphysical in the range computed. This transition is indicated by a switch to lighter, double-dashed curves.

tured in *Mathematica*, Version 5.2) allows the evaluation of Eq. [3.7], except very near $\theta = 0$, where linearization and integration by parts was used to avoid the divergence of the integrand. The resulting frequencies, normalized by the linear frequency ω_1^*, are given for several values of $\lambda < 1$ in Fig. [3.5](top), plotted against θ^{max}, the magnitude of the disturbance. The same methodology was employed for several values of $\lambda > 1$, yielding the curves displayed in Fig. [3.5](bottom), where normalized frequency was plotted against the total energy E. Here E is normalized

by the energy corresponding to the separatrix, along which the frequency vanishes. Results indicate that increasing total volume causes a qualitative change in finite-amplitude response, behaving like a softening spring for smaller volumes but like a hardening spring for larger volumes. As evident in Fig. [3.5](top), for λ very small, frequency decreases with increasing amplitude of disturbance. However, at volumes approaching one, the frequency increases with increasing amplitude, for small θ. In fact, by computing the Taylor series approximation of the period $T(\theta^{max};\lambda)$, given by $A(\theta;\lambda)\partial/\partial\theta\,(C(\theta;\lambda))$, the cross-over volume occurs at $\lambda = 0.32$, where the quadratic term in the series changes sign. According to Fig.[3.5(bo- ttom)], the normalized frequency decreases from one to zero as energy increases from zero to one for all values of $\lambda > 1$. The normalized frequency decreases more rapidly as λ is increased, and larger volumes achieve a smaller normalized frequency in the range of energy considered.

3.2.4 Comparison to Spherical-cap Menisci

Suppose that the cylindrical menisci are replaced by spherical-cap interfaces (replace slot- by tube-support). The dynamics of the spherical-cap system have been previously studied and are qualitatively similar to the dynamics reported above [77]. They are quantitatively different, however, because of the presence of the additional principal curvature. This results in slightly higher-pitched oscillations for the coupled spherical-caps. In our study, finite-amplitude oscillations are found by numerically integrating Eq. [3.7], whereas [77] used a perturbation technique to estimate the frequencies of oscillation for $\lambda < 1$. Furthermore, for $\lambda > 1$, we report frequencies not reported for spherical-caps. An additional difference

between the systems is the susceptibility of cylindrical menisci to 3D instability.

3.3 3D Stability

The results of previous sections assume that the circular menisci remain uniform in the axial direction - only cylindrical-cap beads or lenses have been considered so far. However, cylindrical beads are susceptible to an axial instability of the Plateau-Rayleigh kind, as is well known[8]. Beads of extent $2w$ are unstable when longer than the critical wavelength $2w_c$ of this instability, which depends upon the volume and curvature of the bead. That is, for each total volume $\lambda > 1$, the bead of the lens-bead equilibrium state is axially unstable when $w > w_c$ where, adapting the result of [8] to our notation,

$$w_c = \sqrt{\lambda}\left[\frac{1}{\pi^2} - \frac{1}{4\left(\pi/2 + \arccos\lambda^{-1/2}\right)^2}\right]^{-1/2}. \tag{3.8}$$

According to this stability envelope, interfaces of volume and axial extent above the envelope are unstable, Fig. [3.6]. There is a most dangerous volume and slot halflength $(\lambda_m, w_m) = (1.35, 5.48)$. For $\lambda < 1.0$ or $w < 5.48$, the cylindrical menisci are stable. For volumes $\lambda > 1.0$, there are stable slot lengths above the most dangerous halflength for volumes above the most dangerous volume. Note that the limit of a full-cylindrical bead pinned along two axial line-constraints can be recovered from Eq.[3.8] by recasting in terms of unscaled variables w, R, and r, where R is the radius of the undisturbed cylindrical-cap interface and $2r$ is now the distance between the two line-constraints. The limit of a single axial line-constraint is found by letting $r \to 0$, yielding $w_c \to \frac{2}{\sqrt{3}}\pi R$ which should be compared to the Plateau-Rayleigh limit of πR. Hence, pinning along a line stabilizes by over 15

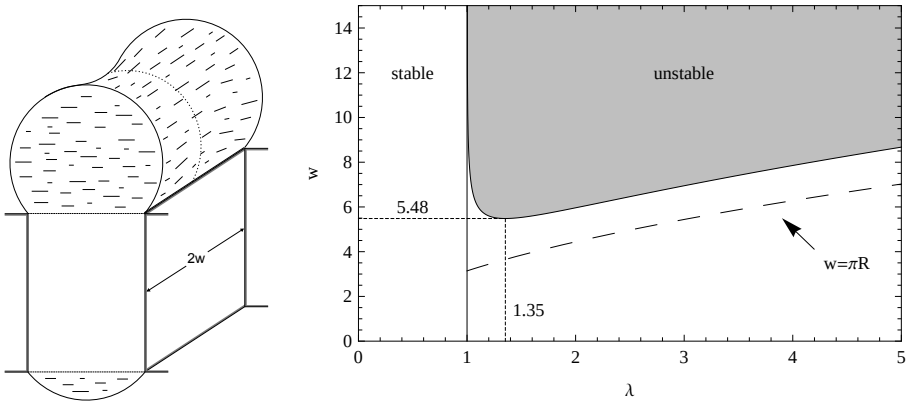

Figure 3.6: 3D stability: (left, sketch) Transverse disturbance which may lead to axial instability. (right) Critical slot halflength w_c above which a single cylindrical interface is unstable to axial disturbances, as it depends on volume $\lambda = V_1 + V_2$. Lens-like menisci $\lambda < 1$ are stable always and bead-like menisci $\lambda > 1$ unstable for sufficiently long beads. The boundary $\lambda = 1$ (solid line) and the classical Plateau-Rayleigh limit (dashed line) of $w = \pi R$ are indicated. The most dangerous fill-volume and geometry corresponds to $(\lambda_m, w_m) = (1.35, 5.48)$.

%, in agreement with previous reports e.g. [23]. Pinning also confers stability at finite volumes, as seen by comparing the Plateau-Rayleigh limit (dashed) with the stability envelope, Fig. [3.6].

During a nonlinear phase-plane oscillation, the volume of each meniscus varies as reported in Section [3.2.2]. During one period, each meniscus may spend some time in the axially unstable regime with finite growth rate. During these fractions of a period of axial instability, the disturbance will grow a certain amount. The net growth (or decay) of a disturbance will depend on the cumulative effect of growth and decay over the full period. To determine this would require a solution of the full dynamic equations which is beyond our scope. However, it can be anticipated that

for those volumes for which the separatrix is a trajectory of physically admissible menisci (e.g. Fig. [3.4], $\lambda = 2$), and for a sufficiently long slot, there will be a neighborhood of trajectories near the separatrix for which axial instability will dominate, in view of the very long periods for those orbits. In contrast, there will also likely be admissible orbits which are unstable over parts of their period but net-stable over the full period and these will likely be located far from the separatrix in the phase plane.

3.4 Conclusion

Inviscidly-coupled cylindrical-cap menisci exhibit small- and large-amplitude phase-plane oscillations. Near the two Lyapunov-stable equilibria, the closed orbits represent vibrations. Far from the equilibria, nonlinear orbits carry the system around all three equilibria in a large-amplitude motion. This variety of orbits is like that seen in the Duffing-oscillator or other conservative systems with a double-well energy potential. The 2D system is also subject to 3D axial instabilities, of the Plateau-Rayleigh kind. The (static) stability envelope where the system is susceptible to axial waves is presented, providing the limits of applicability of the dynamical 2D analysis. The phase-plane dynamics closely compare to previous work on coupled spherical-caps[77]. However, the range of physically-admissible disturbances and susceptibility to 3D instability make the two problems quite different. The 3D stability envelope is presented in a way that may be useful for rapid-solidification processing geometries. To the extent that, despite its simplifications, the model may be relevant to planar-flow spin-casting, the envelope

suggests that axial meniscus instability will not be an issue for lens-like volumes and/or slot widths less than 5.48 times the slot gap. Alternatively stated, meniscus instability can be an issue in casting thin-wide sheet of sufficient width.

3.5 Acknowledgements

This work was partially supported by NSF CMMI-0423794 and CMMI-0726813. The authors would also like to thank Dr. Eric Theisen for useful discussions.

3.6 Derivation of Dynamical System

Here, we present key equations in the derivation of the dynamical system given by Eq. [3.2]. We begin with Newton's second law, which states that

$$\frac{d\left(m\vec{v}\right)}{dt} = \sum Forces. \tag{3.9}$$

Here, we develop a dynamical model for the system of cylindrical menisci described in the manuscript and sketched in Fig. [3.2]. By our assumption that the menisci remain circular-caps, the motion of the center-of-mass remains one-dimensional. If the density is unchanging, we can rewrite the left-hand side (LHS) of Eq. [3.9],

$$\frac{d\left(m\vec{v}\right)}{dt} = \rho\frac{d^2}{dt^2}\left(V_t y_c\right), \tag{3.10}$$

where $V_t y_c = V_0 y_0 - V_1 y_1 + V_2 y_2$. Here, V_i and y_i are the volume and center-of-mass of component i, where $i = 0$ refers to the slot. Note that $y_0 \equiv 0$ and thus $V_0 y_0 \equiv 0$.

Based on the assumptions put forth in Sec. [1] of the manuscript, the only external forces are interfacial forces resulting from the curvature of each component interface. We may then express the right-hand side (RHS) of Eq. [3.9],

$$\sum Forces \equiv 2rw\sigma \left(2H_1 - 2H_2\right), \tag{3.11}$$

where H_i is the mean curvature of component i. If the interfaces are circular in cross-section, the mean curvature of component i related to the principle curvature associated with that circle by $2H_i \equiv 1/R_i^{-1}$. We can now write,

$$\rho \frac{d^2}{dt^2}\left(V_t y_c\right) = 2rw\sigma \left(\frac{1}{R_1} - \frac{1}{R_2}\right). \tag{3.12}$$

Scaling variables with length r, volume $v \equiv \pi r^2 w$ and time $\tau \equiv \sqrt{r^3 \rho/\sigma}$ results in a dimensionless variables $V_t \equiv v\tilde{V}_t$, $y_c \equiv r\tilde{y}_c$, $R_i \equiv r\tilde{R}_i$, and $t \equiv \tau\tilde{t}$. Rewriting Eq. [3.12] with these scaled variables and dropping the tilde ($\tilde{}$) yields,

$$\frac{d^2}{dt^2}\left(V_t y_c\right) = \frac{2}{\pi}\left(\frac{1}{R_1} - \frac{1}{R_2}\right). \tag{3.13}$$

For algebraic simplicity, we parameterize each component volume V_i and curvature R_i by meniscus height h_i where $2\pi V_i = h_i - 1/h_i + \left(h_i + 1/h_i\right)^2$ and $2R_i = h_i + h_i^{-1}$. We may also explicitly compute the component centers-of-mass (COMs), in terms of h_i. The distance of each component COM from its base is

given by $\frac{\langle yV\rangle_i}{V_i} = \frac{2}{3\pi V_i} + \frac{1}{2}\left(h_i - h_i^{-1}\right)$. The component COM from the center of the slot ($y = 0$) is then given by $y_i = \pm L \pm \frac{\langle yV\rangle_i}{V_i}$. The signs of the component COMs are opposite with $i = 1$ chosen to be negative, indicated by Fig. [3.2]. Combining the component COMs allows the system COM to be written,

$$V_t y_c = L\left(V_2 - V_1\right) + \langle yV\rangle_2 - \langle yV\rangle_1. \tag{3.14}$$

To analyze the stability of the system, it is convenient to define two new variables, the difference in component volumes $\theta \equiv V_1 - V_2$ and the total component volume $\lambda \equiv V_1 + V_2$. In this one-dimensional system, θ is the time-dependent variable and λ is a parameter. Component heights are then associated with the functions $h_1 = H_1(\theta;\lambda)$ and $h_2 = H_2(\theta;\lambda)$. A variable transform of the LHS of Eq. [3.13] results in the expression,

$$\frac{d}{dt}\left(\frac{dV_t y_c}{dt}\right) = \frac{d}{dt}\left[\left(\frac{\partial V_t y_c}{\partial H_1}\frac{\partial H_1}{\partial \theta} + \frac{\partial V_t y_c}{\partial H_2}\frac{\partial H_2}{\partial \theta}\right)\frac{d\theta}{dt}\right], \tag{3.15}$$

For brevity, we define $A(\theta;\lambda) \equiv \left(\frac{\partial V_t y_c}{\partial H_1}\frac{\partial H_1}{\partial \theta} + \frac{\partial V_t y_c}{\partial H_2}\frac{\partial H_2}{\partial \theta}\right)$. Substitution for V_t and y_c in terms of H_1 and H_2 and evaluating the derivatives further yields,

$$A\left(\theta;\lambda,L\right) = L + \frac{1}{2}\sum_{i=1}^{2}\left[\frac{3}{2}\left(H_i - H_i^{-1}\right) + \frac{\arctan(H_i)}{1 + \left(H_i - H_i^{-1}\right)\arctan(H_i)}\right] \tag{3.16}$$

Substituting for R_i in terms of H_i in the RHS of Eq. [3.13] results in the expression,

$$\frac{2}{\pi}\left(\frac{1}{R_1} - \frac{1}{R_2}\right) = \frac{4}{\pi}\left[\frac{\left(H_1 - H_2\right)\left(1 - H_1 H_2\right)}{\left(H_1^2 + 1\right)\left(H_2^2 + 1\right)}\right] \tag{3.17}$$

For brevity, we define $C(\theta;\lambda) \equiv -\frac{4}{\pi}\frac{(H_1-H_2)(1-H_1H_2)}{\left(H_1^2+1\right)\left(H_2^2+1\right)}$. Eq. [3.13] may then be rewritten as Eq. [2] from the manuscript,

$$\frac{d}{dt}\left[A(\theta;\lambda,L)\frac{d\theta}{dt}\right] + C\left(\theta;\lambda,L\right) = 0. \tag{3.18}$$

Chapter 4

Thermal Expansion of the Substrate in Planar-Flow Melt Spinning*

4.1 Introduction

The heat-up and subsequent expansion of the substrate in PFMS are known phenomena. The heat transfer into the wheel has been the subject of numerous studies[19, 45]. The connection to thermal expansion was made in a recent paper[76], and incorporated the effect of expansion on the fluid mechanics. As the wheel expands, the gap G between the wheel and nozzle lessens. This constriction

*Enhanced manuscript based on the work in this chapter will be submitted for publication as: B.L. Cox, M.J. Davis, A.L. Altieri and P.H. Steen, 'Thermal expansion of the substrate in Planar-flow Melt Spinning'.

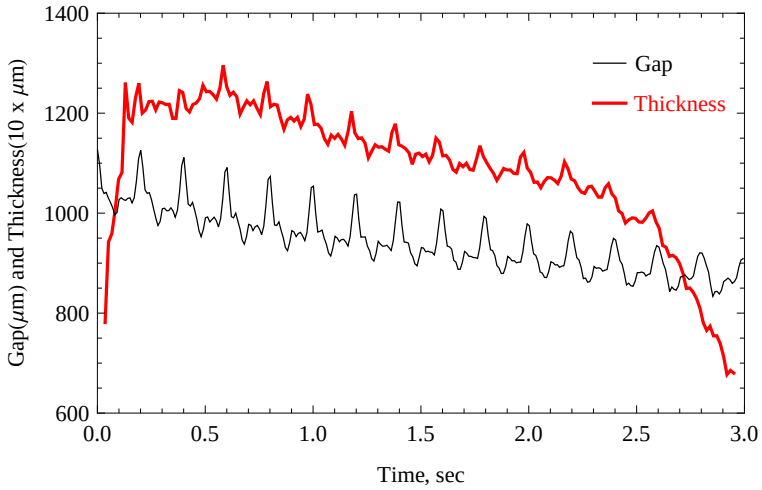

Figure 4.1: Plot demonstrating the coupling of gap (shown in μm) and thickness (in μm multiplied by 10 for scale), with a schematic representing the thermal and fluid mechanics coupling.

reduces flow into the puddle, reducing ribbon thickness. Decreased ribbon thickness reduces heat loading. Thickness and gap data from a cast are shown in Fig. [4.1]. Thus emerged a prediction of $G(t)$ throughout the cast from initial gap G^0.

Here, we aim to improve this model and develop a more precise prediction of $G(t)$. Previously, free volumetric thermal expansion was employed. In Sec. [4.2], we present a derivation of the stress-strain relationship more specific to the geometry of our wheel. Assumptions allow a reduction to the classical thin-walled vessel problem. The result is solved in the manner of [76] and compared to data.

The wheel is not perfectly round. The eccentricity results in a periodic initial gap $G^0(t)$. This fact was accounted for in [76] by a periodic term with an empirically-fit, linearly-decaying multiplier. A physically derived model of $G(t)$ incorporating this variation in G^0 requires adjustment to several assumptions of [76]. In Sec [4.5.1], we introduce an approach to account for this effect by dividing

the initial gap into freely expanding segments. This improved model results in a predictive equation incorporating a non-uniform initial wheel profile, and the non-uniform gap yields non-uniform expansion.

4.2 Thermo-elastic Mechanics of the Substrate

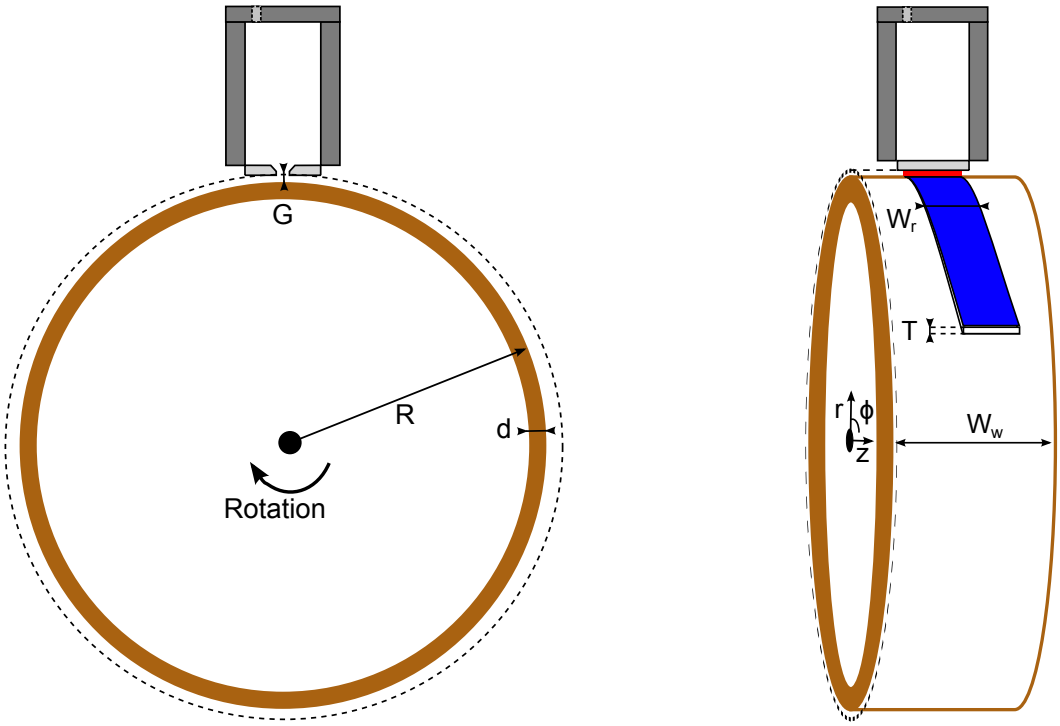

(a) (b)

Figure 4.2: (a) A side-view schematic of the wheel geometry, indicating the gap G, radius R, and thickness d. (b) A schematic representation of the wheel geometry showing ribbon product, indicating ribbon thickness T, ribbon width W_r, and wheel width W_w.

The casting substrate is a cylindrical wheel that is rotated about its axis at a constant RPM, shown in Fig. [4.2], with an outer radius $R = 0.3m$, a thickness

$d = 0.012m$ and an axial width $W_w = 0.135m$. This geometry lends itself to a cylindrical coordinate system, where (r, ϕ, z) are the radial, circumferential, and axial directions of the cylindrical wheel. The crucible nozzle is a constant distance R_{nozzle} from the axis of rotation. The gap $G \equiv R_{nozzle} - R$ is the distance between the nozzle and the outer radius of the wheel R. However, the wheel is absorbing heat from the solidifying metal. As the wheel temperature rises, it expands. Expansion of the outer circumference of the wheel $C \equiv 2\pi R$ decreases G. This expansion is given by the extensional strain, $\epsilon_i \equiv \Delta L_i / L_i^0$, where L_i^0 is the object's original length in the ith dimension, and $\Delta L_i \equiv L_i - L_i^0$ is the change in that length. For the circumferential strain, this may be simplified by $\epsilon_\phi \equiv \Delta C / C^0 = \Delta R / R^0$. We can then write an equation for ΔG,

$$\Delta G = -R^0 \epsilon_\phi. \tag{4.1}$$

The total strain is $\epsilon_i = \epsilon_i^e + \epsilon_i^t$, the sum of the elastic strain ϵ_i^e and the thermal strain ϵ_i^t. The thermal strain is $\epsilon_i^t = \alpha_L \Delta\theta$ for $i = (r, \phi, z)$, where α_L is the linear coefficient of expansion and $\Delta\theta = \theta - \theta^0$ is the change in temperature[28]. In the absence of boundary constraints, the rise in temperature results in volumetric thermal expansion, $\Delta V / V = 3\alpha_L \Delta\theta$. However, because the wheel is subject to geometric constraints, internal stresses develop. The isotropic elastic stress-strain relationship is given by [28] and is a system of three equations,

$$\epsilon_i^e = \frac{1}{E}\left(\sigma_{ii} - \nu \sum \sigma_{jj}\right), \tag{4.2}$$

for $i = (r, \phi, z)$ and $j \neq i$, where σ_{ii} is the isotropic stress in the ith direction, E

is Young's modulus and ν is the Poisson ratio. The shear strain is

$$\gamma_{ij} = \frac{1}{2G'}\sigma_{ij}, \tag{4.3}$$

for $i \neq j$, where σ_{ij} is the shear stress between the ith and jth directions, G' is the shear modulus. Here, we assume that the shear stresses, and thus the shear strains, are identically zero. That is, we assume that right angles are preserved during expansion. Thus, we only consider the isotropic stresses, denoted by σ_i after collapsing repeating indices.

The wheel is bound by two side-plates which are omitted from the schematic in Fig. [4.2]. The side-plates are affixed to axle, which constrains the rim from expanding axially, and justifying the assumption that $\epsilon_z \equiv 0$. This assumption allows us to eliminate an equation in Eq. [4.2] in favor of a system of two equations,

$$\epsilon_i^e = \frac{1}{E}\left[\sigma_i\left(1-\nu^2\right) - \sigma_j\left(\nu+\nu^2\right)\right], \tag{4.4}$$

for $i = (r, \phi)$ and $j \neq i$.

Noting that $d/r = 0.04 < 1/20$, we can use the familiar construction of a thin walled pressure vessel to determine the mechanical strains[58]. We assume that the stresses and strains are uniform throughout the rim thickness. The balance of circumferential forces is utilized to relate the internal pressure of the cylinder to the "hoop stress", given by $\sigma_\phi = \Delta P_w R^0/d$, where ΔP_w is the pressure difference between the inside and outside of the wheel. The balance of radial forces indicates that $|\sigma_r| \leq \Delta P$. Thus $|\sigma_r| << \sigma_\phi$, which justifies the assumption that $\sigma_r \equiv 0$.

This leads to the equations

$$\epsilon_r = -\left(\frac{\Delta P_w R^0}{d}\right)\left(\frac{\nu+\nu^2}{E}\right) + \alpha_L\left(1+\nu\right)\Delta\theta \tag{4.5}$$

and

$$\epsilon_\phi = \left(\frac{\Delta P_w R^0}{d}\right)\left(\frac{1-\nu^2}{E}\right) + \alpha_L\left(1+\nu\right)\Delta\theta. \tag{4.6}$$

It is apparent from these equations that if a pressure difference drives expansion (or contraction) of R, it will decrease (or increase) d, respectively. Thermal expansion increases both R and d, with identical thermal strain. In our experimental apparatus, the inside of the wheel is open to the air, and thus we assume that $\Delta P_w \equiv 0$. This is not necessarily the case for actively cooled wheels, where the inside of the wheel may be enclosed around a heat exchanger. Strain in each direction then reduces to $\epsilon_i = \alpha\left(1+\nu\right)\Delta\theta$, thermal expansion plus the thermal stress from the constrained axial direction. Note that $\Delta d/\Delta R = d^0/R^0 = 0.04$, and thus the absolute change in d is much smaller than that of R. If heating of the wheel is approximated as uniform circumferentially, as in [76], and expansion occurs quasi-statically, then we can write,

$$R\epsilon_\phi = R^0\alpha_L(1+\nu)\Delta\theta. \tag{4.7}$$

Substituting Eq. [4.7] into Eq. [4.1] yields,

$$\Delta G = -R^0 \alpha_L (1+\nu)\Delta\theta. \tag{4.8}$$

4.3 Fluid Flow into Contracting Gap

The amount of ribbon quenched by the substrate will dictate $\Delta\theta$. Therefore, it is necessary to relate the thickness of the ribbon T to G. Previous studies[18, 37] have found that T is related to G when mass and momentum are steady in the liquid in the puddle,

$$\frac{T}{G} = \frac{\rho_l}{\rho s}\left(\frac{2\Delta P}{\rho_l U^2}\right)^{1/2}. \tag{4.9}$$

Fig. [4.3] compares the measured thickness from a cast to T predicted by Eq. [4.9]. For this cast, prediction falls within 10% of the measurement in all but the first and last moments of the cast, where transients dominate thickness[11]. Through this prediction, we can relate G and T at any time. In the remaining sections, we relate $\Delta\theta$ to T, and then eliminate T by substituting Eq. [4.9].

4.4 Uniform Expansion

The heat that enters the wheel is proportional to the amount of metal quenched. This is shown by balancing the heat transfered between the wheel and the quenched metal ribbon, $Q_w + Q_r = 0$, where $Q_w = MC_p\Delta\theta$, where M and C_p are the mass and heat capacity of the wheel, and $Q_r = -M_r(C_{p,l}\Delta\theta_{sup} + \Delta H_f)$ where M_r is

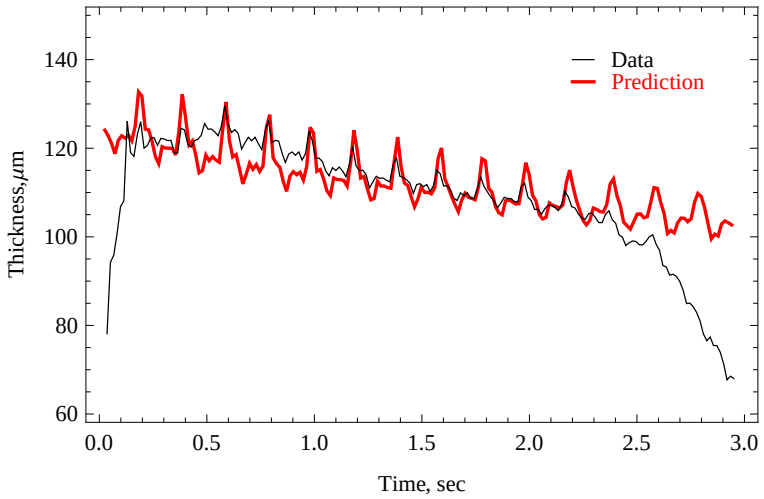

Figure 4.3: Plot comparing measured T with the value predicted by Eq. [4.9].

the total mass of ribbon solidified, $C_{p,l}$ is the heat capacity of the liquid metal, $\Delta\theta_{sup}$ is the difference between initial and melting temperatures of the liquid melt and ΔH_f is the heat of fusion of the metal. Note that this heat balance neglects any cooling below melting temperature (i.e. secondary quenching) and ambient or radiative losses of heat. The value of M_r from $t = 0$ to t is given by,

$$M_r = \rho_s W_r U \int_0^t T(s)ds \tag{4.10}$$

The resulting equation for the temperature rise in the substrate is,

$$\theta(t) - \theta^0 = \rho_s W_r U \left(\frac{\Delta H_f + C_{p,l}\Delta\theta_{sup}}{C_p M} \right) \int_0^t T(s)ds. \tag{4.11}$$

Substituting Eq. [4.11] into Eq. [4.8] yields

$$G(t) - G^0 = -k_t \int_0^t T(s)ds, \tag{4.12}$$

where $k_t = \rho_s W_r U R^0 \alpha_L (1+\nu)(\Delta H_f + C_{p,l}\Delta\theta_{sup})/C_p M$. By substituting Eq. [4.9] into Eq. [4.12] and defining $k_f = \rho_l/\rho s\sqrt{2\Delta P/\rho_l U^2}$, one obtains,

$$G(t) - G^0 = -k_t k_f \int_0^t G(s)ds. \tag{4.13}$$

The solution to Eq. [4.13] is $G(t) = G^0 e^{-k_t k_f t}$, which is plotted in Fig. [4.4] for three different casts. Physical values are taken from Tables [1.1] and [1.2]. The sensitivity to the choice of W_w is demonstrated in Fig. [4.4(a)]. As shown in the schematic in Fig. [4.2(b)], the ribbon only solidifies over a portion of the full wheel width, $W_w = 0.135m$. In [76], it was argued that the "heat-affected zone" of the wheel was width of the ribbon, i.e. $W_w \equiv W_r = 0.05m$. However, some of the heat absorbed by the wheel will diffuse axially, increasing the heat-affected zone. Therefore using $W_w \equiv 0.05m$ provides a lower bound for the mass of substrate expanding, and thus an upper bound on expansion, while using $W_w = 0.135m$ provides a lower bound on expansion. In fact, $W_w \equiv 0.11$ is a better fit for the cast shown in Fig. [4.4(a)]. Further study of the axial diffusion of heat and the effect on expansion is necessary to address this phenomenon physically. Here, we choose to use the actual wheel width $W_w \equiv 0.135$ for all remaining plots to avoid the introduction of a fitting parameter. In Fig. [4.4(b)], this width results in a much better prediction, whereas in Fig. [4.4(c)] it is only marginally better than in Fig. [4.4(a)].

A predictive equation for thickness is then obtained by substituting $G(t)$ into Eq. [4.9], yielding $T(t) = k_f G^0 e^{-k_t k_f t}$. The predicted values of $T(t)$ are plotted against measured T for three casts in Fig. [4.5].

The predicted G compares reasonably well with the center-line of the measured

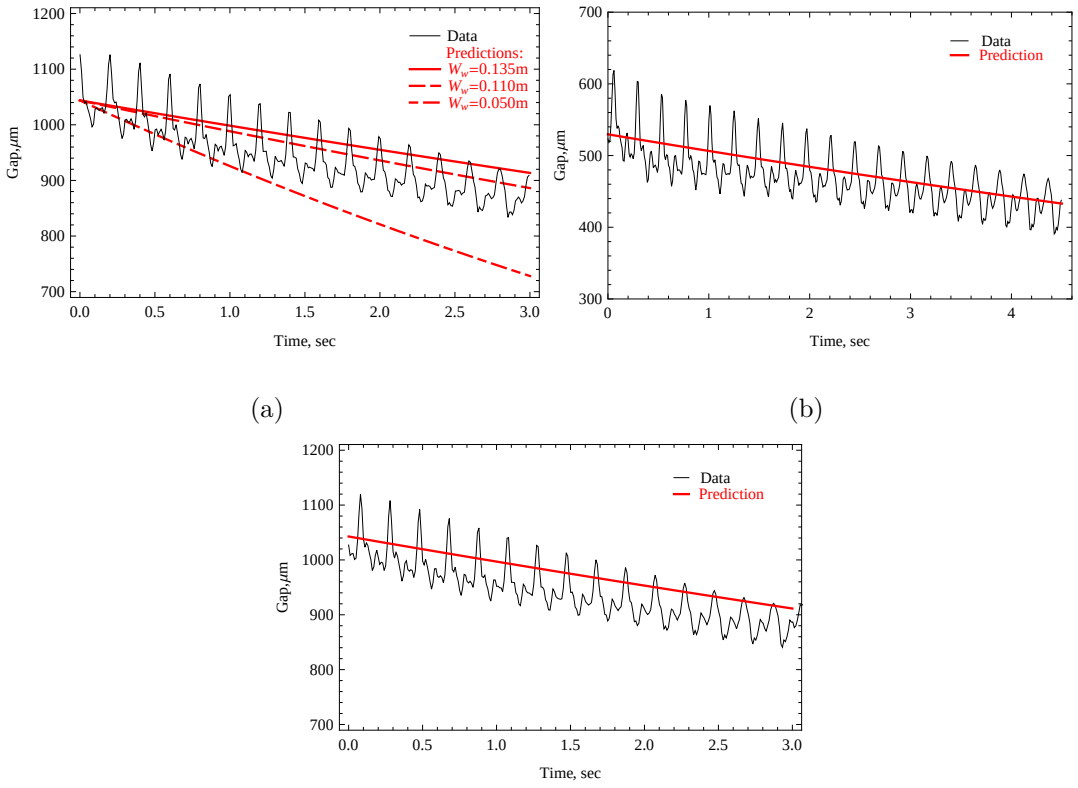

Figure 4.4: Plot of decay vs data, where: (a) $G(0) = 1044\mu m$, $k_t = 0.372459s^{-1}$, $0.457109s^{-1}$, and $1.00564s^{-1}$ for $W_w = 0.135m$ (solid), $W_w = 0.11m$ (dashed) and $W_w = 0.05m$ (double-dashed), respectively, and $k_f = 0.119$; (b) $G(0) = 530\mu m$, $k_t = 0.382s^{-1}$, $k_f = 0.144$, and $W_w = 0.135m$; and (c) $G(0) = 1043\mu m$, $k_t = 0.459s^{-1}$, $k_f = 0.120$, and $W_w = 0.135m$.

gap data. However, this model cannot incorporate the eccentricity of the wheel. In [76], a periodic, linearly decreasing term is added, $\delta(t)sin(\omega t)$ where $\delta(t) = \delta_i - kt$. In the semi-empirical function $\delta(t)$, δ_i is measured from the wheel out-of-roundness and k is fit. In the next section, we develop a non-empirical model for a non-uniform G^0.

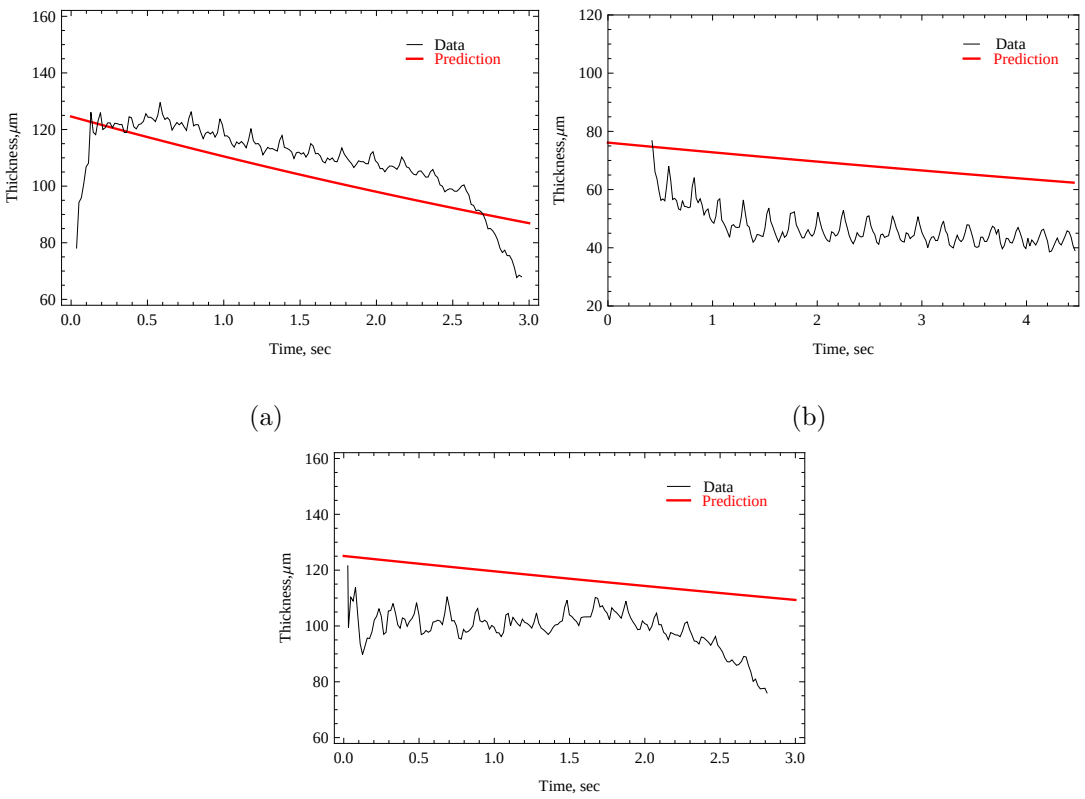

Figure 4.5: Plot of decay vs data, where: (a) $G(0) = 1044\mu m$, $k_t = 0.372459s^{-1}$, $0.457109s^{-1}$, and $1.00564s^{-1}$ for $W_w = 0.135m$ (solid), $W_w = 0.11m$ (dashed) and $W_w = 0.05m$ (double-dashed), respectively, and $k_f = 0.119$; (b) $G(0) = 530\mu m$, $k_t = 0.382s^{-1}$ $k_f = 0.144$, and $W_w = 0.135m$; and (c) $G(0) = 1043\mu m$, $k_t = 0.459s^{-1}$, $k_f = 0.120$, and $W_w = 0.135m$.

4.5 Non-uniform Expansion

The relationship found in Eq. [4.13] can only produce uniform contraction of the gap, since it is assumed that the heat spreads uniformly throughout the wheel. Recent modeling shows that the heat, in fact, penetrates radially much more than it diffuses circumferentially. This suggests that a circumferentially-resolved model

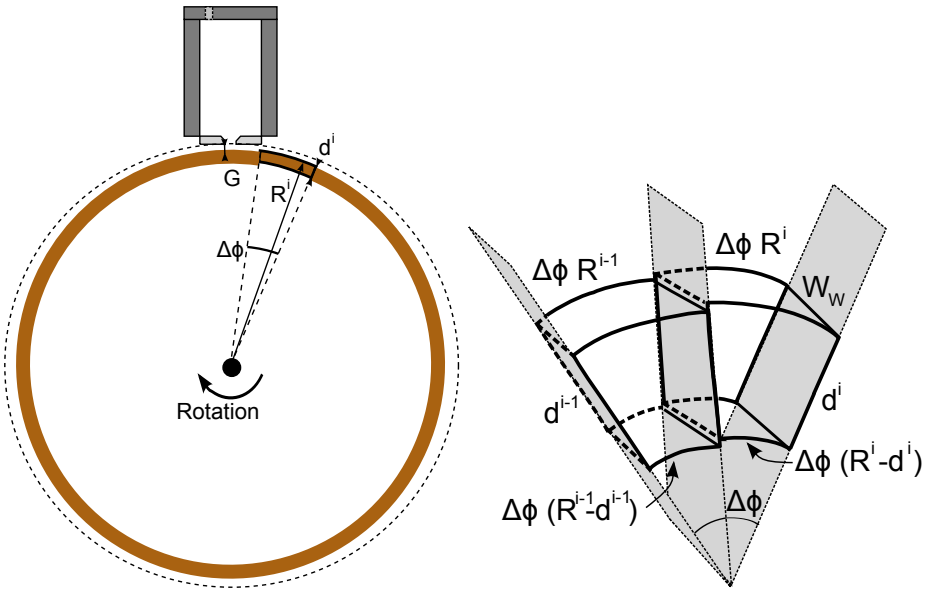

(a) (b)

Figure 4.6: (a) A schematic for the wheel subdivided into n_i wedges of length $\Delta\phi$ radians and radius R^i and thickness d^i for each wedge. The gap G is defined in the lab frame at the leading edge of the nozzle inlet. (b) A schematic for two adjacent wedges, the $i-1$th and ith, stretched in the radial direction for visualization. The thickness of each wedge is d^i, the outer arc length of each wedge is given by $\Delta\phi R^i$, and the inner arc length is $\Delta\phi\,(R^i - d^i)$. The width is W_w.

may be more appropriate. We revisit the original thermal-stress-strain balance with new assumptions. We model the wheel as n independent wedges, all with a common, unchanging width W_w. The ith wedge has thickness d^i and outer arc length C^i. Here, $C^i = \Delta\phi R^i$ and $\sum_i^n \Delta\phi = 2\pi$. The inner arc length is now $(R^i - d^i)\Delta\phi$, as shown in Fig. [4.6(b)].

If this wedge expands freely in the radial and circumferencial directions, while being constrained axially, then it can be considered part of an annulus of radius R^i with mass $M^i = \rho_W W_w \Delta\phi\,(R^i d^i - (d^i)^2/2)$. A second superscript is introduced

to indicate a quasi-static thermal expansion, denoted by j, and the outer radius of this wedge after a change in temperature of $\theta^{i,j} - \theta^{i,j-1}$ is then given by,

$$R^{i,j} - R^{i,j-1} = R^{i,j-1}\alpha_L(1+\nu)\left(\theta^{i,j} - \theta^{i,j-1}\right) \tag{4.14}$$

and corresponds to a change radial distance from the nozzle given by,

$$G^{i,j} - G^{i,j-1} = -R^{i,j-1}\alpha_L(1+\nu)\left(\theta^{i,j} - \theta^{i,j-1}\right). \tag{4.15}$$

Neglecting cooling and diffusion of heat between wedges, each wedge is heated only by ribbon solidified above it. The change in temperature of a segment follows Sec. [4.4], where the mass of ribbon solidifying above the ith segment on the jth revolution is $M_R^{i,j}$, which will be defined later. Thus, after m revolutions,

$$\theta^{i,m} - \theta^{i,0} = \left(\frac{\Delta H_f + C_{p,l}\Delta\theta_{sup}}{C_p M^i}\right)\sum_{j=0}^{m-1} M_R^{i,j} \tag{4.16}$$

4.5.1 Piece-wise Expansion

A simple estimate of $M_R^{i,j} = \rho_s W_r \Delta\phi R^{i,j} T^{i,j}$ allows Eq. [4.15] to be rewritten,

$$G^{i,m} - G^{i,0} = -\rho_s W_r R^{i,0}\alpha_L(1+\nu)\left(\frac{\Delta H_f + C_{p,l}\Delta\theta_{sup}}{C_p M^i}\right)\sum_{j=0}^{m-1}\Delta\phi R^{i,j}T^{i,j}. \tag{4.17}$$

Since $R^i >> d^i$, the mass of the wedge as $M^i \approx \rho_W W_w \Delta\phi R^{i,0} d^{i,0}$, and leads to,

$$G^{i,m} - G^{i,0} = -k_t^i \sum_{j=0}^{m-1} T^{i,j} R^{i,j} / R^{i,0}. \tag{4.18}$$

where $k_t^i \equiv \rho_s W_r R^{i,0} \alpha_L (1+\nu) \left(\Delta H_f + C_{p,l} \Delta\theta_{sup}\right) / \rho_W C_p W_w d^{i,0}$. As the length of the segment and the length of ribbon solidifying above the segment both depend linearly on $\Delta\phi$, this expression is independent of the choice of n_i. Note that for small strain, $R^{i,j}/R^{i,0} = 1 + \epsilon_\phi^{i,j} \approx 1$. Using this approximation, and Eq. [4.9] with $k_f = \rho_l / \rho_s \sqrt{2\Delta P / \rho_l U^2}$ allows us to write,

$$G^{i,m} - G^{i,0} = -k_f k_t^i \sum_{j=0}^{m-1} G^{i,j}. \tag{4.19}$$

which may be solved, yielding,

$$G^{i,m} = (1 - k_f k_t^i)^m G^{i,0} \tag{4.20}$$

This solution is plotted in Fig. [4.7], with the approximation $k_t^i = k_t^0$ where $R^{0,0}$ and $d^{0,0}$ are the average outer radius and thickness of the wheel. All physical parameters are taken from Tables [1.1] and [1.2]. The gap profile is taken from rotations of the wheel prior to the beginning of the cast. Eq. [4.20] compares well with the gap evolution early in the cast. As the cast progresses and the wheel deforms more, the prediction deviates significantly from the data. This is likely owing to our assumption that $\epsilon_\phi << 1$ and will be discussed in Sec. [4.6]. This phenomenon was mentioned in [76] and has been verified here.

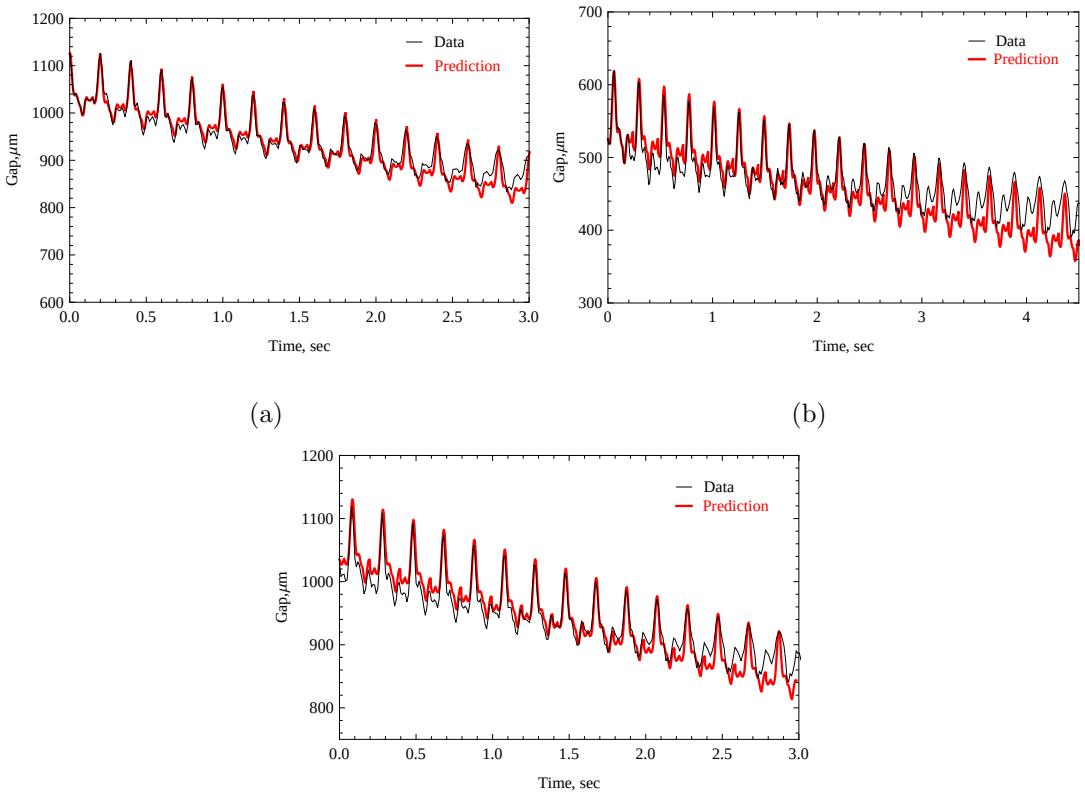

Figure 4.7: Plot of decay vs data, with $k_t^0 = 0.244$ and (a) $k_f = 0.119$, (b) $k_f = 0.144$ and (c) $k_f = 0.119$.

4.5.2 Continuous Non-uniform Expansion

In this section, the goal is to derive the continuous analog of Eq. [4.19]. First, we define a continuous time-sequenced gap $G(t, \phi(t))$ between the nozzle and the wheel. First, we define a reference angle $\phi(t) \equiv \phi_0 + \int_0^t (d\phi/dt)dt$, such that the angle ϕ is directly beneath the upstream nozzle edge at time t. The integrand $d\phi/dt$ is the angular velocity, $\omega \equiv d\phi/dt \equiv U/R(\phi)$, which we assume to be constant, i.e. $\phi(t) = \phi_0 + \omega t$. This assumes that the changes in the radius of the wheel at $\phi(t)$, i.e. $R(t, \phi(t))/R^0(\phi(t))$ are small, an assumption which will be made later in this section, as well. The linear shift ϕ_0 represents the location underneath the nozzle

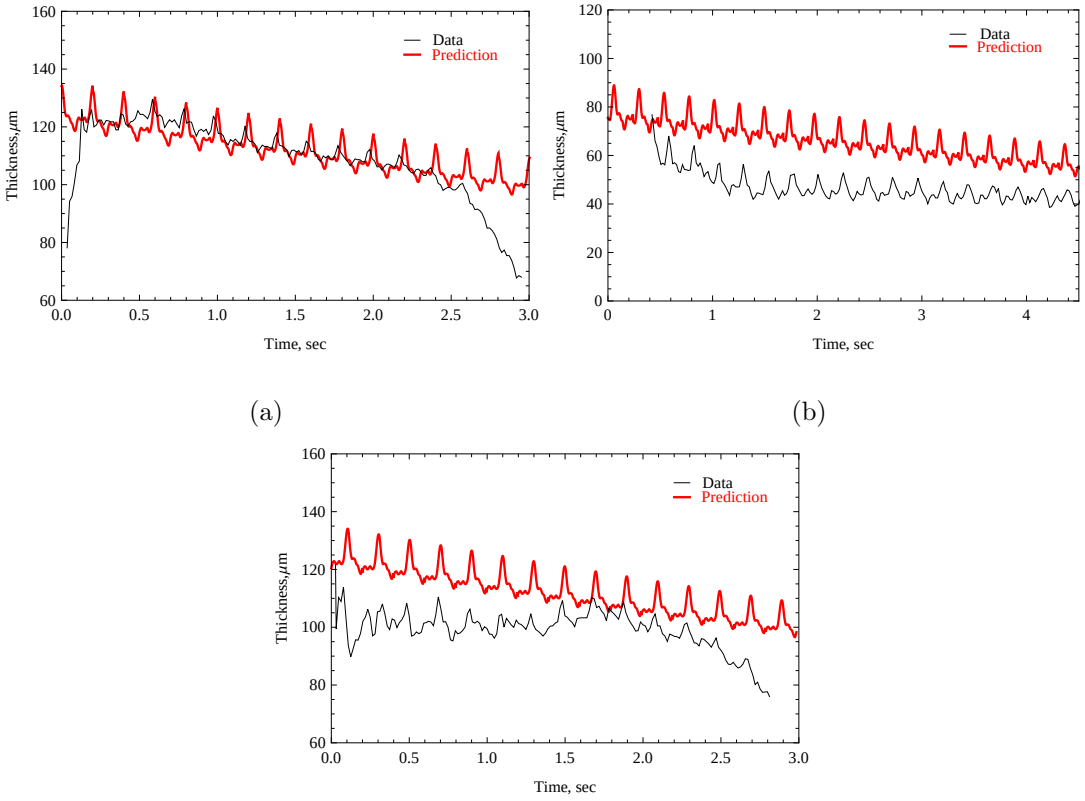

Figure 4.8: Plot of decay vs data, with $k_t^0 = 0.244$ and (a) $k_f = 0.119$, (b) $k_f = 0.144$ and (c) $k_f = 0.119$.

at time $t = 0$. For algebraic simplicity, we will take $\phi_0 \equiv 0$. From this, we define $G(t, \phi(t))$ as the deviation of this initial gap profile evaluated at $\phi(t)$. Explicitly,

$$G(t, \phi(t)) = G^0(\phi(t)) + \int_0^t \frac{dG}{ds} ds. \tag{4.21}$$

where $dG(t, \phi(t))/dt$ is rate of change of the gap for the infinitesimal wedge of the wheel beneath the nozzle inlet at time t. Initial quantities such as $G^0(\phi(t))$ and $R^0(\phi(t))$ have implicit time-dependence through $\phi(t)$, whereas dynamic quantities such as $G(t, \phi(t))$ and $R(t, \phi(t))$ have both implicit and explicit t-dependence.

Henceforth, the argument in $G(t, \phi(t)$ is shortened to $G(t, \phi)$, where the evaluation of ϕ is always performed at the explicit value of t. If expansion is quasi-static, as in Eq. [4.8], then we can write,

$$G(t, \phi) - G^0(\phi) = -\alpha_L(1 + \nu)R^0(\phi) \int_0^t \frac{d\theta}{ds} ds. \tag{4.22}$$

where $d\theta(t, \phi)/dt$ is rate of change in temperature at $\phi(t)$ and t. Since the dynamics of the gap at the inlet are of interest, the dynamics of the gap in the wheel-frame over the course of a revolution are neglected. It is assumed that heat conducts radially into the wheel and the resulting expansion has occured in the segment of the wheel before it returns to the nozzle. The cummulative heat up of the wheel is derived from the sensible heat balance in Sec. [4.4], given by,

$$\int_0^t \frac{d\theta}{ds} ds = \left(\frac{\Delta H_f + C_{p,l} \Delta\theta_{sup}}{2\pi\rho_w C_p W_w R^0(\phi) d^0(\phi)} \right) \int_0^t \frac{dM_r(\phi)}{ds} ds, \tag{4.23}$$

where $M_r(\phi)$ is the total mass of ribbon solidified at $\phi(t)$.

The derivative of $M_r(\phi)$ with respect to ϕ is found by analogy to Sec. [4.5.1]. For this purpose, we define the total mass of ribbon solidified in a revolution, $M_r'(\Phi)$ where $\Phi \in [0, 2\pi)$. The amount of ribbon solidified above some small segment of the wheel at radius $R(\Phi)$ and arclength $\Delta\Phi R(\Phi)$ is,

$$M_r'(\Phi + \Delta\Phi) - M_r'(\Phi) = \rho_s W_r \int_{\Phi}^{\Phi+\Delta\Phi} \int_{R(s)}^{T(s)+R(s)} r dr ds. \tag{4.24}$$

The integral is approximated as $M_r'(\Phi + \Delta\Phi) - M_r'(\Phi) \approx \rho_s W_r \Delta\Phi (R(\Phi)T(\Phi) +$

$T(\Phi)^2/2)$. In PFMS, ribbon is very thin relative to the radius of the wheel, i.e. $R(\Phi) >> T(\Phi)$, allowing further simplification to $M_r'(\Phi + \Delta\Phi) - M_r'(\Phi) \approx \rho_s W_r \Delta\Phi R(\Phi) T(\Phi)$. The limit of $\Delta\Phi \to 0$ recovers a differential equation for the amount of ribbon solidified above an infinitesimal wedge of the wheel during a revolution,

$$\frac{dM_r'}{d\Phi} \approx \rho_s W_r T(\Phi) R(\Phi). \tag{4.25}$$

The total mass solidified at $\phi(t)$ is the sum of the mass solidified at the infinitesimal wedge corresponding to $\phi(t)$ each prior revolution, i.e. $M_r(\phi) = \sum_{j=1}^{n_{rev}} \left(M_r'(\Phi)\right)_{\Phi=\Phi_j}$, where $\Phi_j \equiv \phi(t - j\tau)$ for $t \in [(j-1)\tau, j\tau)$ and $\Phi_j \equiv 0$ for t outside the interval. Also, $\tau = 2\pi/\omega$ is the period of a revolution, and $n_{rev} = floor(t/\tau)$ is the number of revolutions the wheel has completed at time t. Thus, $dM_r/d\phi$ can be written in terms of $dM_r'/d\phi$,

$$\left(\frac{dM_r}{d\phi}\right)_{\phi(t)} \approx \sum_{j=1}^{n_{rev}} \left(\frac{dM_r'}{d\Phi_j}\frac{d\Phi_j}{d\phi}\right)_{\phi(t-j\tau)}. \tag{4.26}$$

In Eq. [4.22], dM_r/dt can be rewritten $(dM_r/d\phi)(d\phi/dt)$. Substituting this after evaluating Eq. [4.26] yields,

$$G(t,\phi) - G^0(\phi) \approx -\frac{k_t(\phi)}{R^0(\phi)} \int_0^t \left[\sum_{j=1}^{n_{rev}} \left(T(s,\Phi_j) R(s,\Phi_j) \frac{d\Phi_j}{d\phi}\right)_{\Phi_j=\phi(s-j\tau)}\right] ds. \tag{4.27}$$

where $k_t(\phi) \equiv \alpha_L(1+\nu)\omega R^0(\phi)\rho_s W_r(\Delta H_f + C_{p,l}\Delta\theta_{sup})/(2\pi\rho_w C_p W_w d^0(\phi))$.

The integral spans $[0, t)$, however for each term in the sum, $d\Phi_j/d\phi$ is only non-zero for $[t-(j+1)\tau, t-j\tau)$, and thus the integral of each term only contributes in this interval. Since these intervals are adjacent and non-overlapping, the summation collapses into a single integral,

$$G(t,\phi(t)) - G^0(\phi(t)) \approx -\frac{k_t(\phi)}{R^0(\phi)} \int_0^t T(s-\tau,\phi)R(s-\tau,\phi)ds, \tag{4.28}$$

Further substituting Eq. [4.9] into Eq. [4.28] yields,

$$G(t,\phi(t)) - G^0(\phi(t)) \approx -\frac{k_f k_t(\phi)}{R^0(\phi)} \int_0^t G(s-\tau,\phi)R(s-\tau,\phi)ds. \tag{4.29}$$

The formulation arrived at in Eq. [4.29] is then substituted into Eq. [4.21] yields,

$$G(t,\phi) \approx G^0(\phi) - \frac{k_f k_t(\phi)}{R^0(\phi)} \int_0^t G(s-\tau,\phi)R(s-\tau,\phi)ds. \tag{4.30}$$

Since $R(t)$ changes much less than $G(t)$, we assume that $R(t) \equiv R(t-j\tau) = R^0(\phi)$. Thus we can rewrite Eq. [4.30],

$$G(t,\phi) \approx G^0(\phi) - k_f k_t(\phi) \int_0^t G(s-\tau,\phi)ds. \tag{4.31}$$

The solution to this nonlinear delay-integral equation is not sought here. However, the assumption made between Eq. [4.30] and Eq. [4.31] is qualitatively similar to the assumption between Eq. [4.18] and Eq. [4.19], specifically, $R(t,\phi)/R^0(\phi) = 1 + \epsilon_\phi(t,\phi) \approx 1$.

4.6 Discussion and Conclusion

Here we address the effect of the assumption $1 + \epsilon_\phi \approx 1$. As the wheel radius increases, both the gap is constricted and the circumference grows. As the gap shrinks, less fluid enters the region due to hydrodynamic resistance. As the circumference grows, a competing effect is seen, as this region of the wheel increases in length relative to other sections, and thus has a longer segment of ribbon solidify above it.

This competition may be numerically represented by the ratio of increasing length to decreasing thickness for an equal change in gap, $-2\pi\Delta R/\Delta T = 2\pi k_f$. This ratio is around 0.75 for the casts in Figs. [4.7(a)] and [4.7(c)], and 0.9 for the cast in Fig. [4.7(b)]. This perhaps explains why the prediction worsens more rapidly in Fig. [4.7(b)]. The primary differences between the first and third casts and the second cast are the wheel speed and the cast length. The slower wheel speed exacerbates the expected error, as the ratio given is proportional to $\sqrt{\Delta P}/U$. The longer cast length simply allows for greater eventual deviation due to any errors present.

Despite this assumption, the results presented here are an improvement over previous model as the need for empirical fitting is eliminated, and non-uniform expansion is allowed. The prediction is particularly good early in the cast. This prediction could be made prior to the cast if the initial gap data were collected. Also, future analysis of formulation presented in Sec. [4.5.2] may lead to a more precise understanding of the nonlinearities evident in the gap dynamics.

4.7 Acknowledgements

Experiments were supported by NSF Grant Nos. CMMI-0423791 and CMMI-0726813 and NSF sponsored REUs. The authors thank Si Chen, Jeffrey Fisher, Bo Hu, Chris Jakobson and Brian Carroll for help with experiments and measurements used in this study. We also thank ALCOA for supplying materials for these experiments.

Chapter 5

Experimental Apparatus and Methodology

5.1 Background

The casting machine consists of a wheel, motor, furnace-box and super-structure supporting the furnace-box. The machine was originally designed and documented by JK Carpenter[16]. Modifications to this design and operating procedure have been recorded[79, 38, 40, 63]. Significant modifications to the super-structure and furnace-box were performed by CJ Byrne and EA Theisen in 2003[75, 10]. A photograph of the current casting machine is shown in Fig. [5.1]. The induction heater on the left of the casting machine is on the left in this photograph. The motor is on the right. Major modifications to the apparatus and methodology between Spring 2007 and Spring 2010 are described in the following sections.

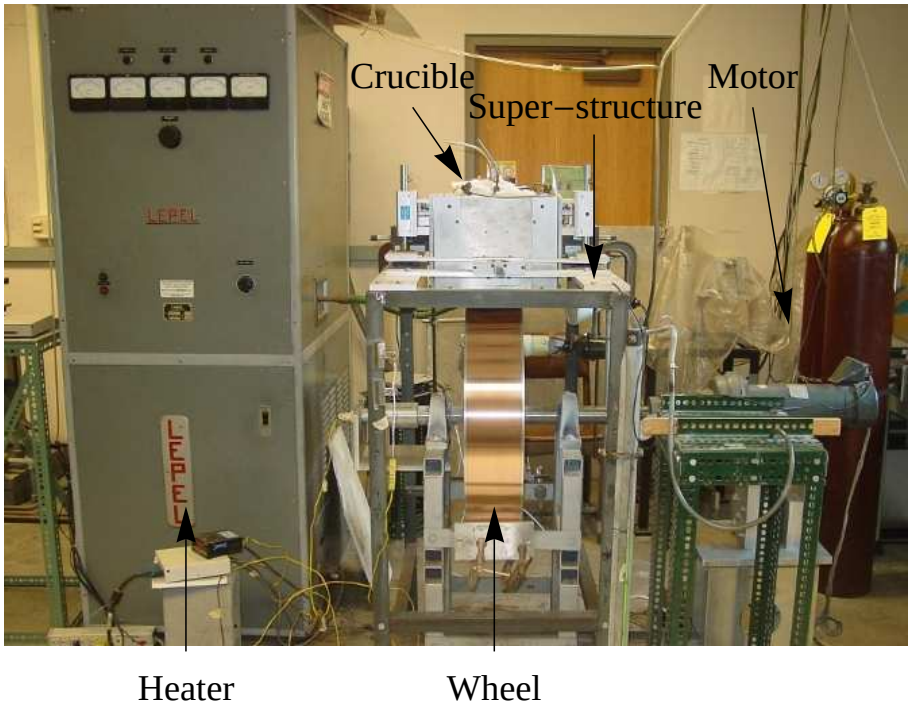

Figure 5.1: Image of Olin Hall 101 casting apparatus.

5.2 *In Situ* Debris Removal

Non-uniform or incomplete release of the ribbon product from the substrate results in debris affixed to the wheel. That debris circulates on the wheel and reenters the puddle region, as shown in Fig. [5.2]. Debris formation destabilizes the USM and is often concurrent with streaks on both sides of the ribbon product. These streaks appear in the direction of the cast and comrpomise the strength and uniformity of the ribbon product. Throughout the course of a cast, the debris deposited on the wheel accumulates, compromising (a) the contact between the heat sink (wheel) and the solidifying metal and (b) the stability of the upstream meniscus. This debris also makes imaging of the puddle difficult, as previously observed[75]. Since

2006, several measures have been tested to prevent the debris from circulating on the wheel.

The first of these methods was a spinning brush (commercial paint roller affixed to an electric motor). This brush was placed upstream of the puddle, at slightly less than 45 degrees from the apex of the wheel (9 o'clock position). The brush successfully removed debris from the wheel, but often sent this debris through the air, into the puddle region, leading to more serious destabilization of the USM and worse imaging issues than in the absence of the brush.

The second of these methods was a rubber scraper afixed to the bottom of the wheel assembly, shown in Fig. [5.3]. The rubber scraper was placed firmly against the wheel before setting the RPM, immediately prior to casting. This squeegie was very successful at preventing the circulation of debris and has remained in use.

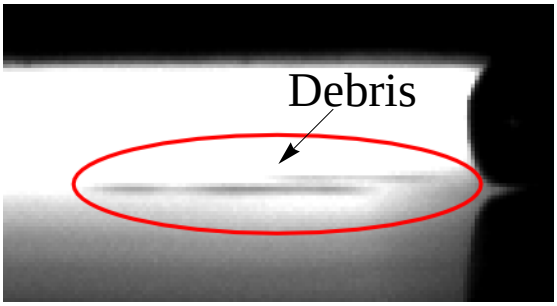

Figure 5.2: Debris on wheel from high-speed image.

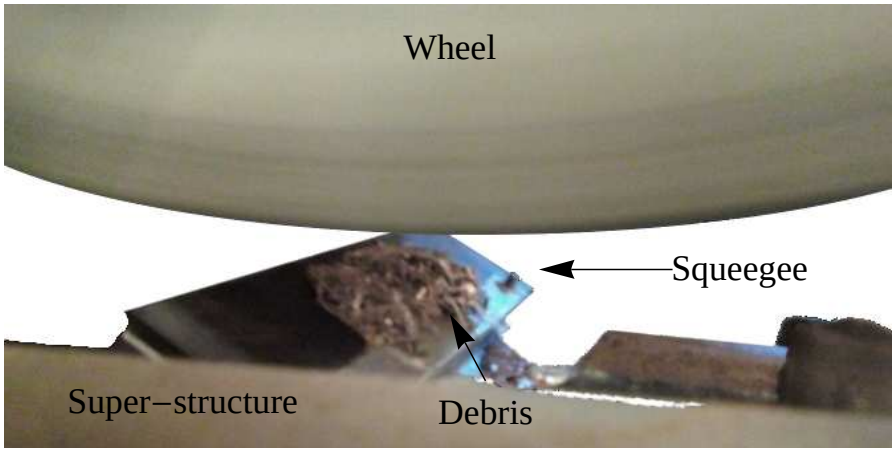

Figure 5.3: Image of rubber scraper with debris from a cast. The scraper is pressed against the wheel during a cast.

5.3 Imaging

Prior to the summer of 2008, motion of the puddle was observed using a Kodak EktaPro high-speed video system, shown in Fig. [5.4(a)], capable of recording at up to 6000 frames per second (fps) and with 2 GB of storage capacity. The maximum resolution of images captured by the Kodak is approximately 0.15 mm per pixel at 6000 fps and with the full puddle in view. A higher ratio of mm per pixel can be achieved with a smaller field of view. This video must then be retrieved from the video system using analog RF (composite) signal capture, which is then redigitized by a computer.

During the summer of 2008, a Redlake MotionXtra HG-XL was acquired, shown in Fig. [5.4(b)]. This camera is capable of recording up to 100,000 fps onto 16 GB of storage. The maximum resolution of images captured by the Redlake is approximately 0.03 mm per pixel with the full puddle in view, providing a five-fold increase over the Kodak EktaPro. At higher frame rates, the exposure time of

(a) (b)

Figure 5.4: High-speed imaging systems used in 101 Olin Hall. (a) Kodak EktaPro high-speed video system. (b) Redlake MotionXtra HG-XL high-speed video camera.

the CCD is decreased, and thus the demand for light increases. The 300 Watt light bulb that was sufficient for 6000 fps allows video capture only up to around 20,000 fps with the HG-XL, however special lighting loaned from Del Imaging Systems has allowed casts to be successfully imaged at as high as 50,000 fps, with full puddle images at 30,000 fps. Video is retrieved in digital form via a TCP/IP connection. An image captured with the HG-XL is shown in Fig. [5.5].

Both cameras have since been used simultaneously, allowing for puddle imaging while also capturing high-speed images of the ribbon departing the substrate.

5.3.1 Video Analysis

High-speed images are subsequently analyzed using a variety of software. National Instruments Vision Assistant software and Xcitex ProAnalyst software are used for their edge-finding algorithms, and further image analysis is performed in Matlab

Figure 5.5: Raw image of FHSU08-32 captured at 5000 fps. Labels were superimposed to indicate the USM, DSM and liquid puddle. A white dashed line was added at the wheel/puddle interface to distinguish the puddle from its shadow.

and Mathematica. An example raw image from Cast ID FHSU08-32 is shown in Fig. [5.5].

5.3.2 Contact Angle Measurements

Matlab code, written by HB van Lengerich for the analysis of the motion of liquid bridges, was modified to follow the upstream meniscus of the puddle. The angle of the substrate-puddle-gas contact-line was measured for several casts of varying wheel speed, gap and surface tension, as shown in Fig. [5.6]. The contact-angle was not observed to vary consistently with either wheel speed or gap, and for the typical Al-7% Si alloy cast, the angle was found to lie most often between 140 and 160 degrees, to be compared to a literature estimate of 150 degrees[14]. The addition of bismuth to the alloy, however, rapidly decreases the surface tension and results in an observed decrease in the mean contact-angle. The mean contact-angle was near 130 degrees for Al-7 % Si 4.5% Bi ($\sigma \approx 0.46$ N m^{-1}) and near 120 degrees for Al-7 % Si 6.9% Bi ($\sigma \approx 0.43$ N m^{-1}) (surface tensions were approximated from binary alloy data in literature[34]). The contact-line velocity was also measured for several casts in an attempt to characterize the relationship of the contact-angle

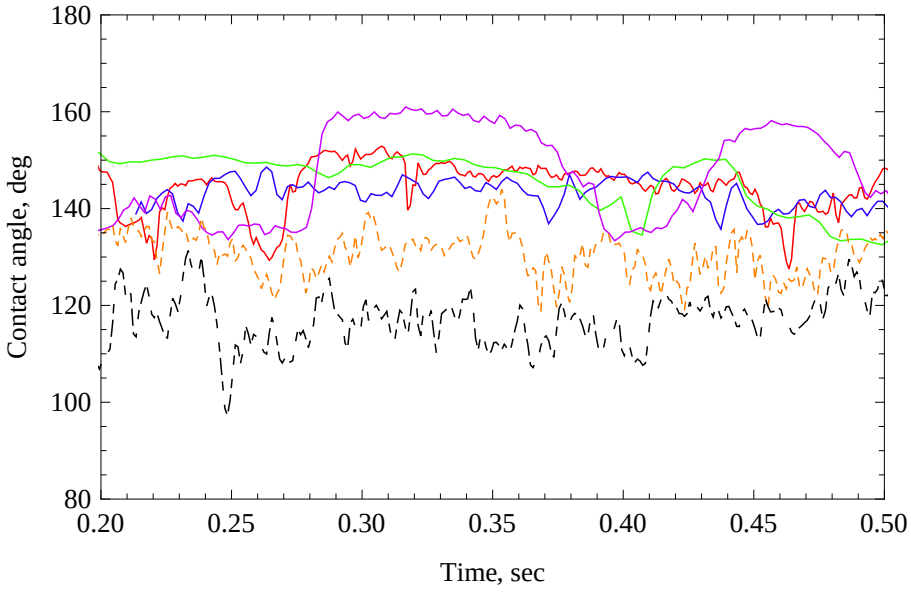

Figure 5.6: Contact-angle results from video analysis of ACSU08-09, FHSU08-20, FHSU08-25 and FHSU08-32 (Al-7% Si, $\sigma = 0.86$ N m^{-1}), and CJSU09-30 (Al-7% Si 4.5% Bi, $\sigma = 0.46$ N m^{-1}), and CJSU09-38 (Al-7% Si 6.9% Bi, $\sigma = 0.43$ N m^{-1}) at wheel speeds between $6 - 10$ m s^{-1} and gaps of $0.75 - 1$ mm. Standard surface tension casts are shown in solid lines. CJSU09-30 and CJSU09-38 are dashed and double-dashed, respectively. Surface tensions are estimated from literature tables[34].

versus capillary number, $Ca = \mu U_{CL}/\sigma$, where U_{CL} is the measured contact-line speed, as shown in Fig. [5.7]. The plot suggests that contact-angle and capillary number are independent of one another.

5.3.3 Puddle Length Measurements

The puddle length L, the length above the substrate over which solidification is occuring, is an important but difficult to measure quantity. For instance, it has

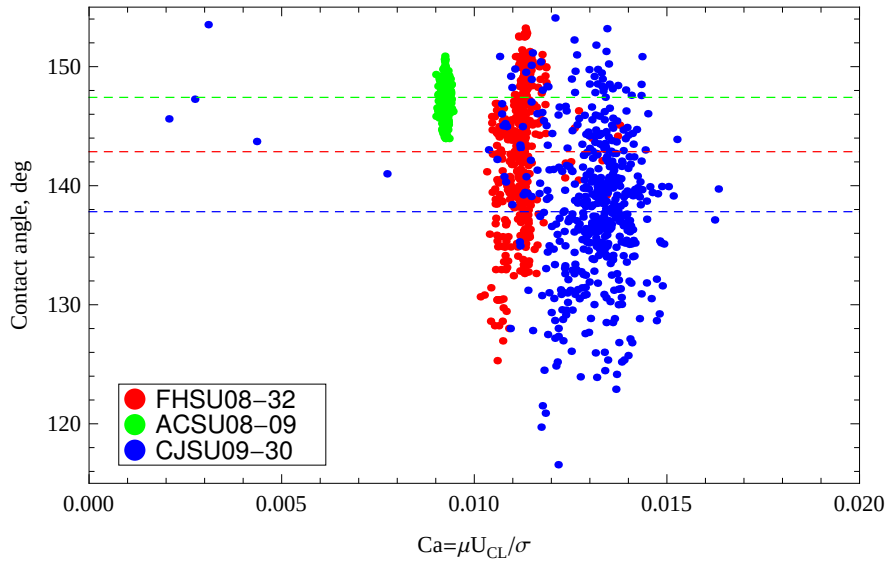

Figure 5.7: Contact-angle versus capillary number, $Ca = \mu U_{CL}/\sigma$, where U_{CL} is the measured contact-line speed, from video analysis of FHSU08-32 and ACSU08-09 (both Al-7% Si), along with CJSU09-30 (Al-7% Si 4.5% Bi). Mean contact-angles are by dashed lines, 142.9, 147.4, and 137.8 respectively. Values for FHSU08-32, ACSU08-09 and CJSU09-30 are shown in red, green and blue, respectively.

been shown that the solidification velocity can be inferred from $V = TU/L$, where T and U are easily measured[76]. However, L may be measured directly only by high-speed imaging. A method for measurement of L has been presented for the study of solidification velocity[75, 76]. This method measures the length from the USM to the DSM along a single row of pixels. The longest row of these pixels that appears to correspond to DSM (instead of ribbon) is converted from pixels to length and recorded as L. However, the location of the tri-junction between liquid melt, solid ribbon and the gas is challenging to pin-point, and due to the gentle slope of the DSM. Subsequently, the method of [75, 76] will systematically understimate L. Further, any variation from a square view of the puddle by the camera will

significantly alter the measured L. Left-, right-, and downward-looking images of the puddle will result in an underestimation of L, while an upward-looking image will result in an overestimation of L.

In an effort to make these measurements more robust, a new methodology is proposed. The idea is illustrated in Fig. [5.8]. Note that light and dark are converted to binary black and white in this side view. The image is then inverted such that black represents the back-light shining through and white represents the dark silhouette of the puddle and nozzle. The same row-scanning algorithm as [75, 76] is used to determine the locations of the USM and DSM, given by the green squares in Fig. [5.8]. The DSM is then fit to a line, $h(x,t) = m(t)x + b(t)$, demonstrated by the red line in Fig. [5.8], where t is time associated with the image. $t = 0$ represents the beginning of the cast. The time-course of the value of the lowest USM point, and all four DSM points, are given in Fig. [5.9]. For the fit of $h(x,t)$, only the higher 3 rows are used, as the lowest point on the DSM (longest length) likely moves below the tri-junction at times during the cast. The coefficients for this fit are averaged over the time associated with a thickness measurement, U/L_R. The intersection of this line with the height of ribbon, $T(t) - (G(t) - G(0))$, is then taken to be the location of the tri-junction, $x^*(t) = (T(t) - G(t) + G(0) - b(t))/m(t)$, shown in Fig. [5.10].

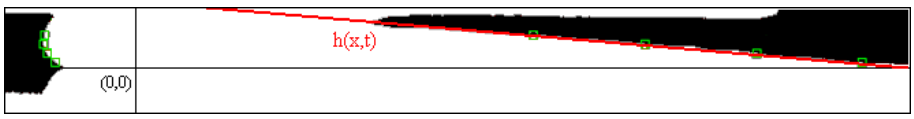

Figure 5.8: Image illustrating the points of the USM and DSM located by edge-finding software (green squares). The fit of the DSM points, $h(x,t)$ is shown as a red line.

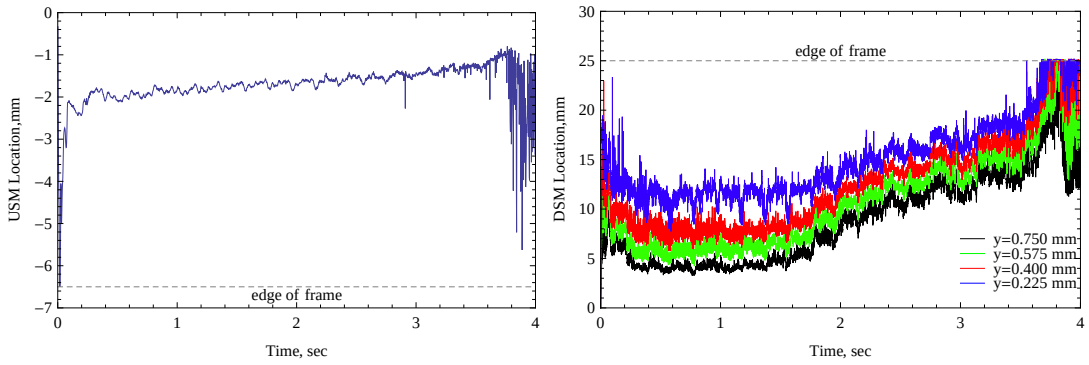

(a) (b)

Figure 5.9: Location of the (a) USM, in mm, L and (b) DSM in mm for four different heights above the initial gap.

The length L is then the distance from the USM to $x^*(t)$. In Fig. [5.11(a)], L_{new} is calculated using this methodology and compared to L_{old}, acquired using the old methodology. Note that $L_{new} > L_{old}$, but that the dynamics are qualitatively identical. We may also now plot $V = TU/L$ using this data, shown in Fig. [5.11(b)], again giving a qualitatively unchanged V_{new}. Thus the conclusions of Theisen 2010 are still be correct, despite a systematic underestimation in L and overestimation of V.

5.3.4 Profilometry and Surface Roughness Measurements

The profile of the ribbon surface ribbon surface was measured in the manner described by Byrne, et al[14], using a MicroXam Interferometric Profilometer (ADE Phase Shift, Tuscon, AZ). Measurements are filtered and stitched together by MapVue (Ade Phase Shift) and the results are plotted in Matlab (The Mathworks, Natick, MA) shown in Fig. [2.5(b)]. Single-axis profiles were also acquired using a Mitutoyo Surftest SJ-301 Surface Roughness Analyzer (courtesy of Hitachi-

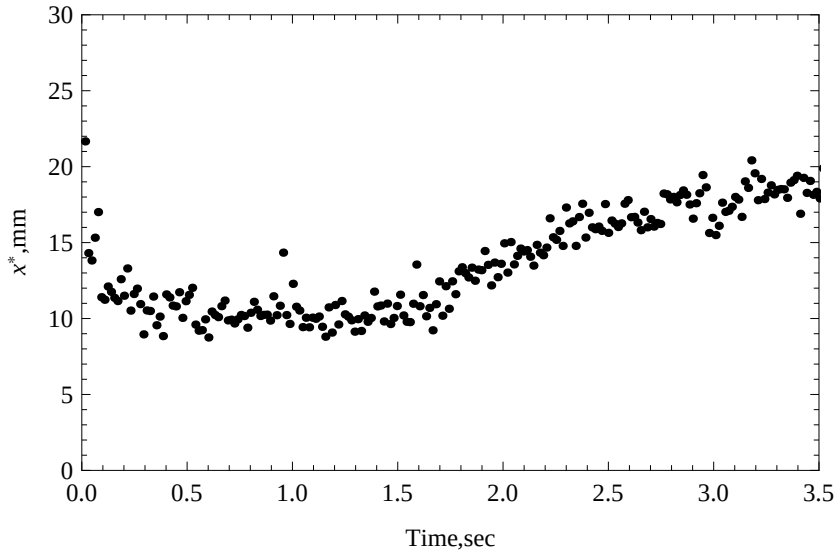

Figure 5.10: Calculated $x^*(t)$.

Metglas, Inc). The Surftest SJ-301 can filter and print data to tape, or output raw data through an RS-232C connection. The raw data of 4 mm in the stream-wise direction of ribbon exhibiting herringbone defect is shown in Fig. [5.12]. Scans of the filtered printout for a different 4 mm stream-wise scan of HB is shown in Fig. [5.13]. At the time of this thesis, the SRA is being used in a study of defect depth as a function of cast parameters. Prior measurements were acquired using optical profilometry (c.f. Sec. [2.3]). The preliminary results of this study are briefly recounted here.

The morphology of HB was acquired using a MicroXam Interferometric Profilometer (ADE Phase Shift, Tuscon, AZ). Three pieces of ribbon from different times in the cast were analyzed. Sections of 3 mm x 2.5 mm containing at least two defect lines were scanned. The filtered results were then analyzed using MatLAB. The lines (referred to here as 'trenches') associated with each defect were traced, with a sample shown in Fig. [5.14(a)]. The trench depths were measured and

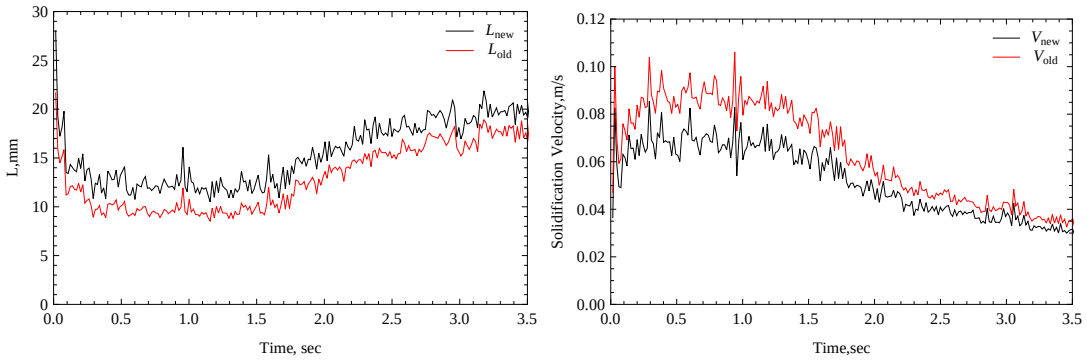

(a) (b)

Figure 5.11: Comparison of old and new methods for (a) inferring puddle length, L and (b) calculating solidification velocity, $V = TU/L$.

plotted as a function of cross-stream displacement. A sample plot of these profiles is shown in Fig. [5.14(b)]. The mean and median trench depth in μm are shown as horizontal dashed lines (lowest-valued dashed line and middle-valued dashed line, respectively), for comparison to the to the global mean interface height (highest-valued dashed line). The mean and median depth for all lines on each section are averaged and plotted as a function of cast time t, shown in Fig. [5.15].

5.4 Ribbon Detachment

5.4.1 Background

Study of the mechanism and dynamics of ribbon-substrate adhesion and detachment in PFMS began with the original patent[55]. Anticipating the location of detachment from the wheel is important for design purposes. Perhaps the greatest motivation for such studies is a phenomenon where by the ribbon suddenly fails

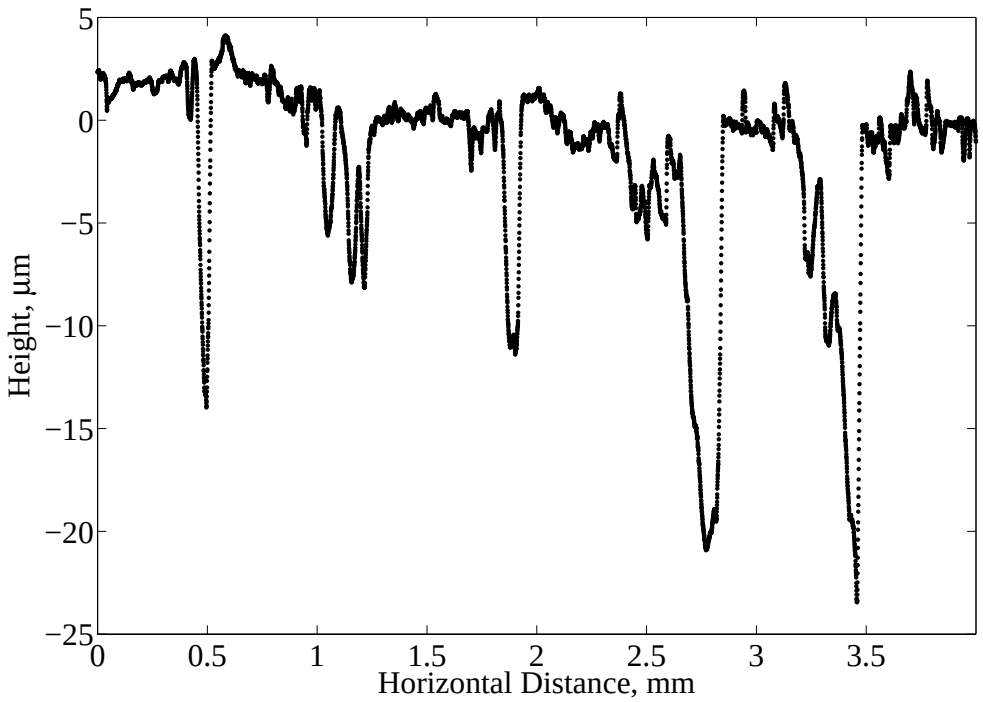

Figure 5.12: Height variation versus distance along the cast direction, in μm, as measured by the Mitutoyo Surftest SJ-301.

to detach from the substrate, known as "catastrophic sticking". Initial studies speculated that "centrifugal force" is the cause of detachment[48] but was later ruled out by a scaling argument[51]. A mechanical means of stripping the product from the substrate was developed (e.g. gas stripper) to prevent sticking[48]. However, the reduced product/substrate contact time and added stresses associated with forced removal have negative consequences, such as non-uniform release of the product[51].

Later studies have established through a simple argument of scales that the only mechanism with sufficient strength to break the bond is thermal stress release[51]. Once the ribbon exits the puddle, it begins to cool below melting temperature.

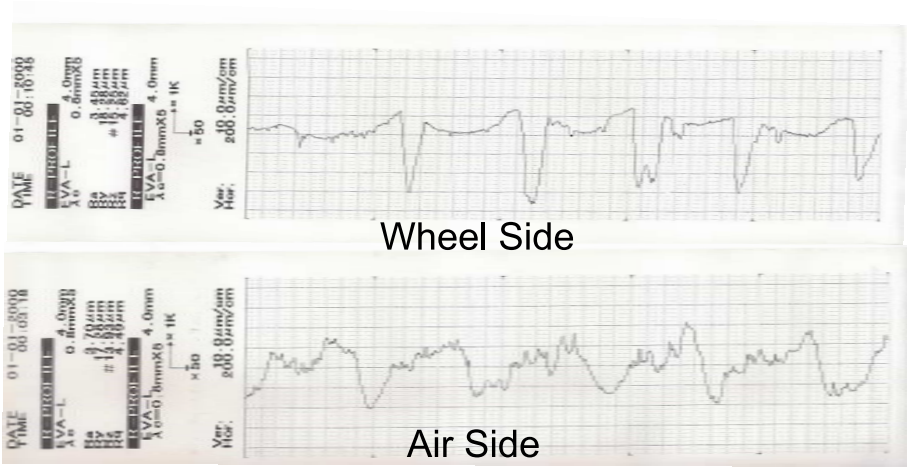

Figure 5.13: Height versus distance along the cast direction as measured by the Mitutoyo Surftest SJ-301.

This cooling leads to the accumulation of thermal stress in the cross-stream direction of the ribbon. At sufficiently high stress, the ribbon overcomes adhesive forces and departs from the wheel. The conclusion of this study was that the following physical parameters all contribute to the heat flow into the substrate (and thus the cooling): (i) substrate surface temperature, (ii) substrate surface chemistry, (iii) substrate surface geometry, (iv) substrate velocity, (v) substrate surface maintenance procedures, (vii) melt superheat and (viii) ambient atmospheric conditions.

Drop-splat experiments were performed that controlled all but parameter (i), substrate surface temperature. These experiments found a critical detachment temperature T_c for each melt/substrate pair. If the substrate temperature rose above T_c, detachment did not occur. T_c was explained as the ribbon temperature at which sufficient thermal stress accumulates to overcome adhesive forces. Since the ribbon cannot cool below the substrate temperature, it is when the substrate reaches T_c that detachment does not occur. Thus, catastrophic sticking occurs

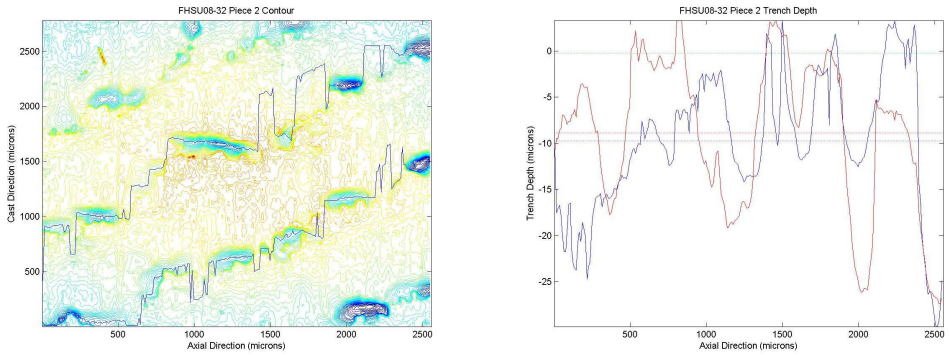

(a) (b)

Figure 5.14: (a) Contour plot of a 3 mm x 2.5 mm section of the wheel-side of ribbon from FHSU08-32. The contour is plotted in Matlab with a line indicating the path of the local minimum across the cross-stream direction. (b) The depth of the local minima as a function of cross-stream distance.

when the substrate temperature exceeds T_c.

In practice in PFMS, (ii) and (iii) should not vary much if (v) does not, and (iv) and (vii) are cast parameters. Thus, the two uncontrolled parameters are (viii) atmospheric conditions, which are presumably not greatly varying, and (i) substrate surface temperature. Thus, it is anticipated that for PFMS, the detachment length will depend primariy upon substrate surface temperature and the time for the ribbon to reach T_c, and catastrophic sticking is expected if the surface temperature of the substrate reaches T_c. This potentially explains why catastrophic sticking was observed in our laboratory when casting on a steel substrate[10]. In particular, the thermal diffusivity of steel is significantly smaller than that for CuBe, and thus the surface temperature would be expected to increase much more rapidly.

The experimental studies in literature are limited to the two aforementioned articles, neither of which provides sufficient data to predict a detachment length.

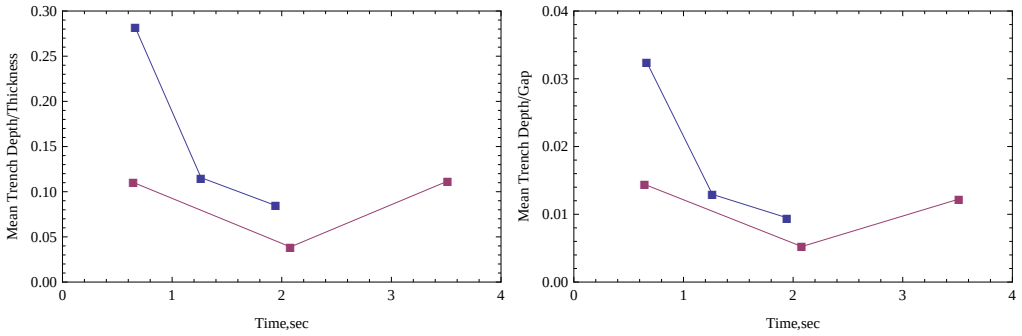

(a) (b)

Figure 5.15: (a) Mean trench depth normalized by thickness T. (b) Mean trench depth normalized by gap G.

Previous investigations of detachment length have had little success as catastrophic sticking is not reproducible and the dynamics of the increase of detachment length occurs very rapidly[48, 10]. However, some recent progress in this direction is outlined in the next two sections.

5.4.2 Detachment Temperature Measurement

Interest in the temperature at which the ribbon departs the wheel T_f arises from several perspectives. First, detachment occurs when the ribbon cools sufficiently to accumulate thermal stresses that exceed adhesive forces, i.e. $T_f \equiv T_c$. Also, T_f is one of two possible fates of heat in the overall heat balance of the PFMS process, which we now present.

The molten metal prior to the cast is "charged" with an amount of thermal energy. Throughout the course of a cast, a portion of the initial thermal energy is imparted into the wheel. The remaining thermal energy remains in the ribbon after it detaches. To determine the extent of the portion that is quenched by the sub-

strate, a heat balance is performed over a rectangular control-volume in the puddle region, as shown in Figure [5.16]. The result is $Q_5 + Q_6 = Q_7 + \Delta Q_{2-1} + \Delta Q_{4-3}$, where the energies are defined by: $\Delta Q_{2-1} \equiv Q_2 - Q_1 = M_{cast} C_{p,s} \left(T_m - T_f\right) / t_{cast}$, the sensible heat lost in the liquid; $\Delta Q_{4-3} \equiv Q_4 - Q_3 = M_{cast} C_{p,s} \left(T_m - T_f\right) / t_{cast}$, the sensible heat lost in the solid; Q_5, the heat conducted to wheel; Q_6, the heat conducted to nozzle or air (assumed to be 0); and $Q_7 = M_{cast} \Delta H_f / t_{cast}$, the heat generated by solidification. The heat conducted between liquid and solid Q_8 is a flux within the control volume and does not appear in the overall balance. Knowl-

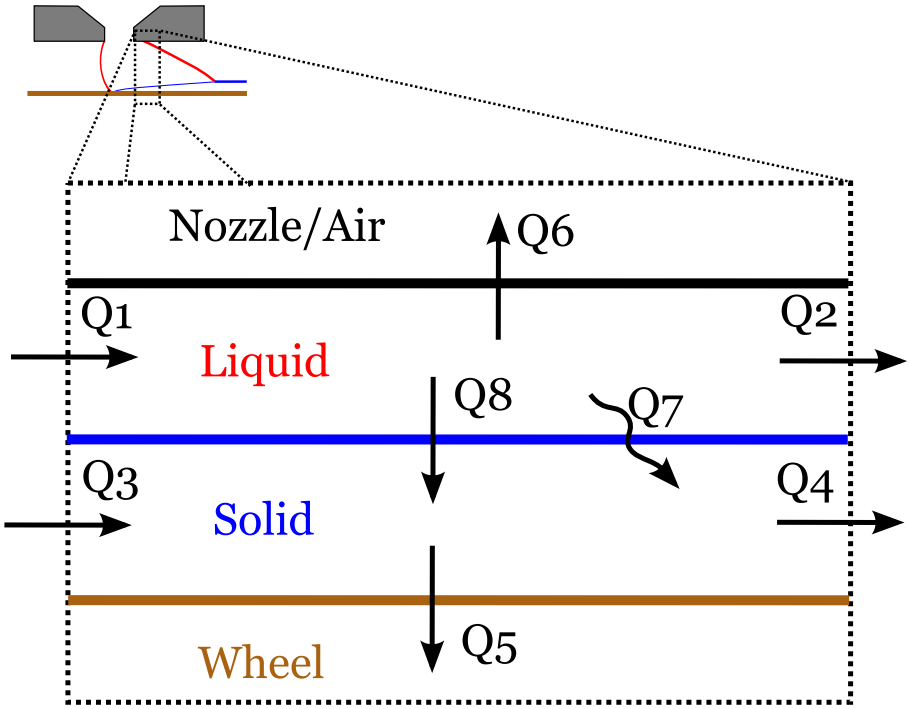

Figure 5.16: Heat balance for a typical control-volume slice of the puddle, where $Q_2 - Q_1$ is the sensible heat lost in the liquid, $Q_4 - Q_3$ is the sensible heat lost in the solid, Q_5 is the heat conducted to wheel, Q_6 is the heat conducted to nozzle or air, Q_7 is the latent heat generation and Q_8 is the heat conducted between liquid and solid.

edge of the material parameters and the mass and duration of the cast along with T_f would allow Q_5 to be determined.

However, the measurement of T_f has been elusive. Non-contact measurement of ribbon temperature requires precise targeting of the ribbon departure location and a rapid sampling time. While equipment recently acquired (courtesy of Hitachi-Metglas, Inc.) may eventually enable measurement of T_f, these challenges have yet to be overcome. In the meantime, a simple calorimetry experiment is devised to measure the cast-average of T_f.

Ribbon was cast into an insulated bath which was then covered and allowed to reach thermal equilibrium. The rise in temperature of the calorimeter ΔT_{cal} was then measured. This indicated the total heat absorbed $Q_{cal} = (mC_p\Delta T)_{cal}$. From Q_{cal} was calculated the entering temperature of the ribbon, $T_{ribbon,0} = T_{ribbon,1} + Q_{cal}/(mC_p)_{Al}$. As the Biot number of the ribbon in air was low ($Bi = hL/k_s \approx 10^{-5}$ for a flat plate where h=82 W m^{-2} K^{-1}, k=220 W m^{-1} K^{-1}, L = 10^{-4} m), the change in temperature in flight from the wheel to the bath $\Delta T_{flight} = T_f - T_{ribbon,0}$ was estimated using a lumped-parameter analysis to give a characteristic cooling time of 5 seconds. From this, T_f was calculated using data from 9 experiments, shown in Figure [5.17]. The mean T_f, $\bar{T_f}$ was 509 $\pm$ 11 °C, which compares favorably to numerical predictions of 512 °C and 520 °C for two (different) casts fit to a computational model by the Brian Thomas group.

There were notable sources of error despite the simplicity of these experiments. The largest source of error was likely heat loss. The ribbon wound and knotted as it collected in the calorimeter, and much of it remained above the level of the bath in initial attempts. In order to ensure that all of the ribbon be completely

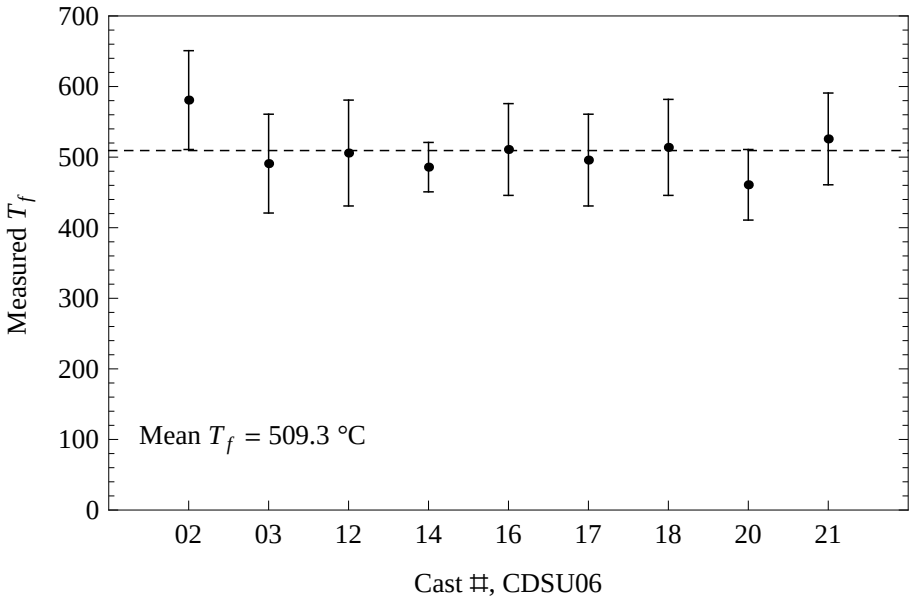

Figure 5.17: The results of 9 calorimetry experiments. The mean of T_f is 509 °C, shown dotted. Error bars shown result from the standard deviation of final bath temperature. Only for the first measurement is the mean excluded from range of error, and only by 0.3 %.

submerged in the bath, boron nitride strips were painted on the wheel to cut the ribbon into strips shorter than the length of the calorimeter. Strips that did not land entirely in the bath were removed prior to equilibriation and not counted in the total mass of aluminum. Also, the following demands on the fluid in the calorimeter were difficult to meet. The fluid had to be non-volatile to minimize heat loss to evaporation, have a high flash point for safety, have a high thermal diffusivity to allow for quick equilibration and have a high viscosity to minimize splashing. Corn oil was ultimately decided upon and used for all trials, but some evaporation and splashing were still observed. Nevertheless, heat loss contributed solely to negative error, and its major sources, such as those mentioned above, were qualitatively evident. Thus, trials where this was significant were apparent

and were deemed failures. Ultimately, 7 of 16 trials were excluded from the data for this reason. Most of these trials were preliminary attempts, and 5 of the last 6 casts were retained.

5.4.3 Detachment Length Measurements

The donation of a second video camera by Hitachi-Metglas freed up the Kodak EktaPro to be used for detachment length measurement. In the summers of 2009 and 2010, the EktaPro was used to capture ribbon detachment of many casts at up to 125 frames per second, a significant improvement over the camcorder used in previous attempts. This work began as a summer project for Brian Carroll, an undergraduate in the lab. Preliminary results suggest that detachment length varies proportionally with ribbon thickness. This seems consistent with the predictions of [51], as the mass of the ribbon should govern cooling time, but a full analysis of this data is currently under preparation.

5.5 Modified Nozzle Experiments

The effect of nozzle geometry on puddle stability has been studied previously[36], as has the effect of geometry on the pressure profiles within the puddle[10]. Here, we describe two types of modified nozzles designed to probe the relationship between defect formation and pinning of the USM.

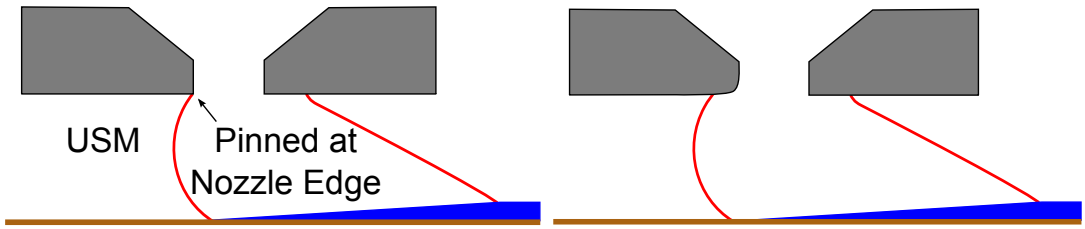

(a) (b)

Figure 5.18: Schematic representation of the puddle when (a) the nozzle is a sharp corner (unmodified) and the meniscus is pinned and (b) the nozzle corner is rounded (modified) which inhibits pinning.

5.5.1 Half-rounded Upstream Edge

Half of the nozzle's upstream edge was sanded to produce a smooth, round boundary upon which the meniscus cannot pin. This is shown schematically in Figure [5.18], where (a) represents the cross-section on the unmodified half and (b) shows the cross-section with a rounded edge. These casts were performed in the regime of HB, and exhibited the HB defect on the unmodified side, but exhibited either CW or interrupted HB formation on the rounded side, as shown in Figure [5.19]. This experimental realization of simultaneous CW and HB patterns implies that pinning is necessary for HB. More detail about this cast is given in Chapter [2].

5.5.2 Notched Upstream Edge

For a second set of experiments, a rectangular section of the upstream edge was removed across the length of the slot, producing an L shaped notch in the inlet nozzle. A photograph of a nozzle with a notch of 1.8 x 4.2 mm is shown in Figure

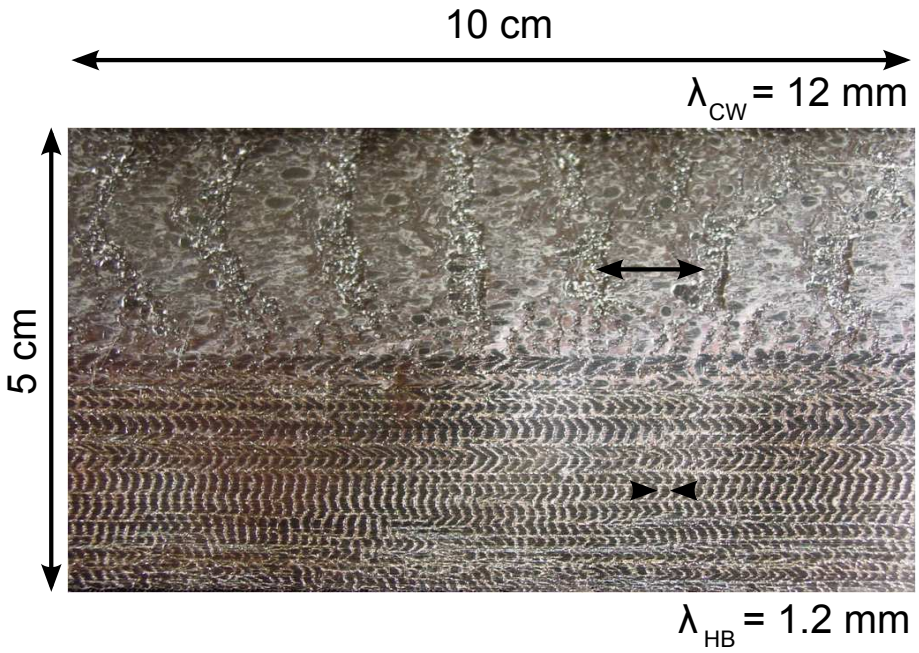

Figure 5.19: Ribbon product exhibiting both crosswave (upper-half) and herringbone (lower-half) defects.

[5.20(a)], and a schematic of the puddle with a notched nozzle is shown in Figure [5.20(b)]. These casts were performed in the regime of HB formation, but exhibited CW defect for the majority of the cast, as shown in Figure [5.21], where the data for the notched casts is compared to HB and CW. In the high-speed video of the puddle, the USM appeared to remain pinned throughout the cast, but this is difficult to confirm with complete confidence. This result suggests that pinning is not sufficient for the appearance of the HB defect. The specific mechanism for HB inhibition remains unclear. The modified nozzle inserts could not be cleaned and reused, so only 3 such casts were performed, with measured notch heights and lengths of 2.3 x 2.2 mm (CJSU10-05), 1.7 x 3.8 mm (CJSU10-06) and 1.8 x 4.2 mm (CJSU10-07).

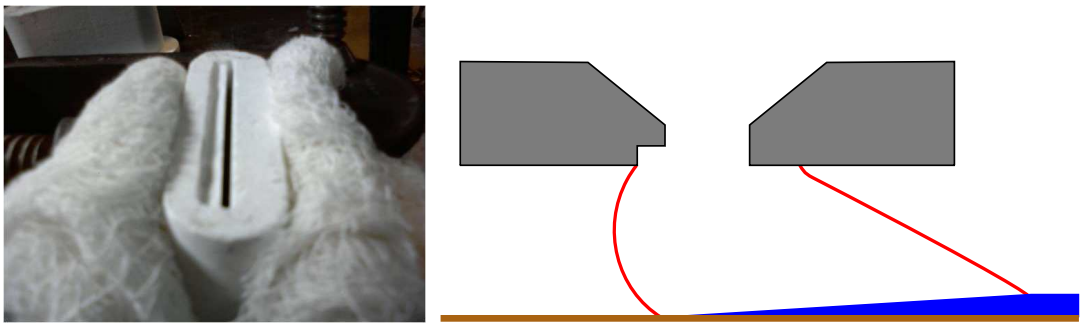

(a) (b)

Figure 5.20: (a) A photograph of a nozzle with a 1.8 mm high by 4.2 mm long notch removed and (b) a schematic of the puddle with a notched nozzle.

5.6 Conclusion

In summation, changes to experimental methodology and the acquisition of new equipment has allowed for both new and more precise measurement of many cast parameters. The introduction of a mechanical scraper has improved ribbon quality. The acquisition of a new camera has improved video analysis, allowing for improved measurement of directly observable geometric parameters. The additional camera has also allowed simultaneous high-speed video capture at both puddle and cast scale, elucidating the dynamics of ribbon detachment. Simple calorimetry experiments have further informed the study of ribbon detachment and leaving temperature. Finally, modified nozzle inserts have provided insight into the physical influences on defect formation.

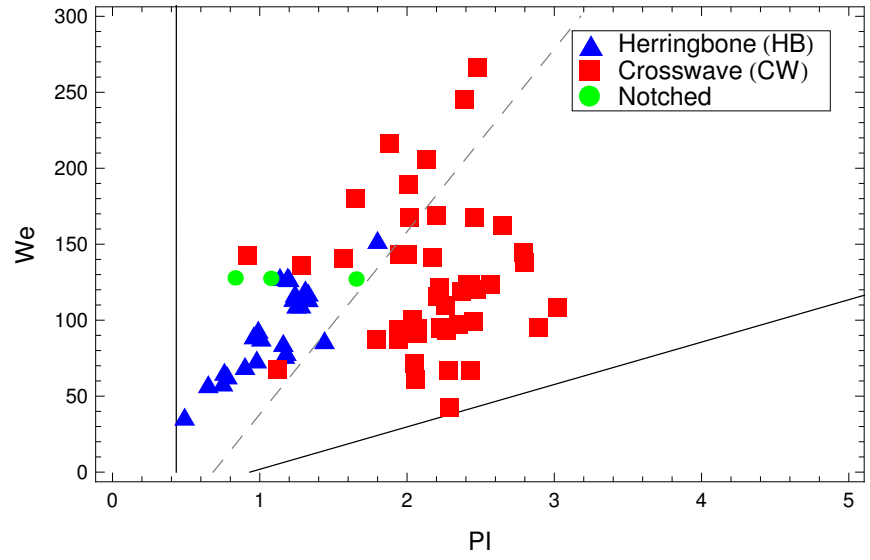

(a)

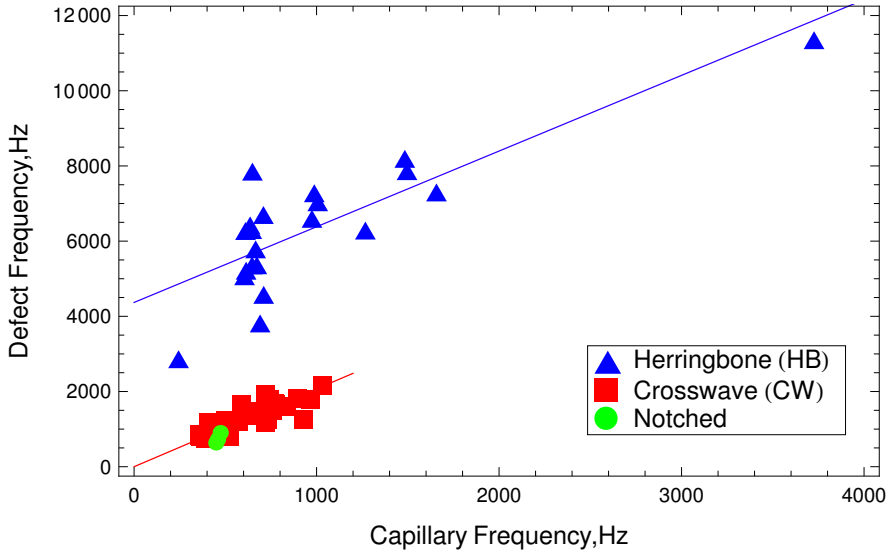

(b)

Figure 5.21: Notched casts compared to HB and CW data w.r.t. (a) the We vs PI operating window and (b) capillary frequencies.

Chapter 6

Conclusion

6.1 High-Frequency Defect Formation

Chapter [2] examines where in parameter-space and at what frequency the herringbone casting-defect appears through comparison to the crosswave casting-defect. Experiments suggest that pinning of the upstream meniscus is a necessary condition for HB. When the upstream meniscus cannot pin, CW appears. Pinning may be prevented by the geometry of the nozzle, and it is experimentally shown that a rounded nozzle, which should not allow pinning, results in CW. The USM may also become unpinned if the pressure of the fluid is sufficiently high to wet the nozzle. A semi-empirical threshold for this pressure is presented, based on We and PI. It is shown that experiments in the $(We, PI) - plane$ on one side of this threshold exclusively exhibit the CW defect, whereas on the other, both HB and CW appear. The frequency of HB scales with $f_c = \sqrt{\sigma/\rho G^3}$ like CW, but this scaled frequency is proportional to We, indicating an influence of inertia that is not

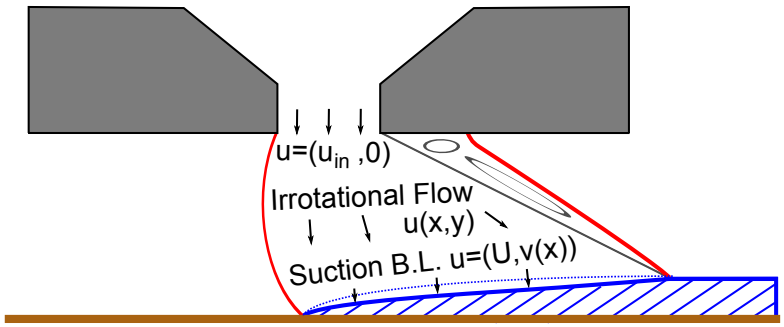

(a)

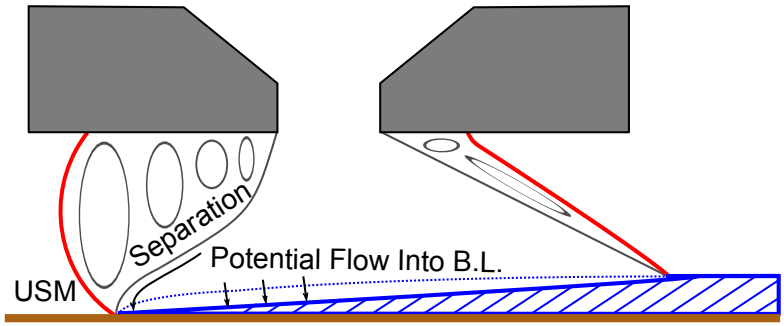

(b)

Figure 6.1: Schematic representation of the puddle when (a) flow is not separated and (b) flow is separated in the upstream and downstream. Separation lines represent the streamlines dividing the flow in the puddle region. Region I is conserved from (a) but Regions II and III (shaded) emerge as distinct hydrodynamic regions.

present in CW. The decoupling of CW from *We* is likely related to the separation of flow adjacent to the meniscus that likely coincides with de-pinning. Here, we briefly discuss how this separation can influence the local physics.

This discussion merits some comments about the relationship between solidification, the meniscus, and flow. There are two possibilities regarding the nature of the meniscus and the substrate: either the metal contacts the wheel as a liquid, in which case there is a dynamic contact line and a tri-junction, or the liquid feeds directly into the solidification front, and no moving contact line is formed[71]. As

the solidification is extremely rapid, it is likely that the metal solidifies upon contact with the substrate, and no dynamic contact line is present. The fluid flow, heat transfer, and solidification near tri-junctions were studied in depth by Anderson and Davis[1]. Their investigations revealed local geometric requirements for the flow based on the mass and heat transfer requirements at the solidification front. For a steady solidification front, the feed rate must be given by $\rho_l u = \rho_s U$ to balance the mass. I.e. as $\rho_s/\rho_l > 1$, the feed rate must be greater than U. Additionally, any flow adjacent the meniscus must be tangent to the interface for the meniscus to be stationary. The scaling analysis indicates that the dominant flow interacting with surface tension in the oscillation is proportional to U. If the flow is separated in the upstream puddle region, the meniscus will not experience this flow, and no such We dependence should be expected. Thus, for this interpretation to be viable, the selection mechanism between the crosswave and herringbone defects should be the separation of the flow in the upstream region. This is represented in Fig. [6.1(b)], to be constrasted with the unseparated case in Fig, [6.1(a)].

A model directly related to PFMS yielding this scaling has not been established. However, if is reorganized into $\lambda/G = (C_{HB}\sqrt{We})^{-1}$, a familiar scaling emerges. Christodoulou and Scriven found a comparable dependence in a study of slide coating, a process used in manufacture of photographic products[20]. They solved the Navier-Stokes equation for the base flow down the slide, as represented in Fig. [6.2]. Linearized perturbations to the base state showed that for $Re >> 1$, standing waves persist for long distances upstream. The estimated wavelength of these standing waves is $\lambda/h_0 = (C_0\sqrt{We_0})^{-1}$, where $C_0 = 18/25\pi$, h_0 is the height of the fluid in the direction normal to the plane, $We_0 = \rho U_0^2 h_0/\sigma$ and U_0 is

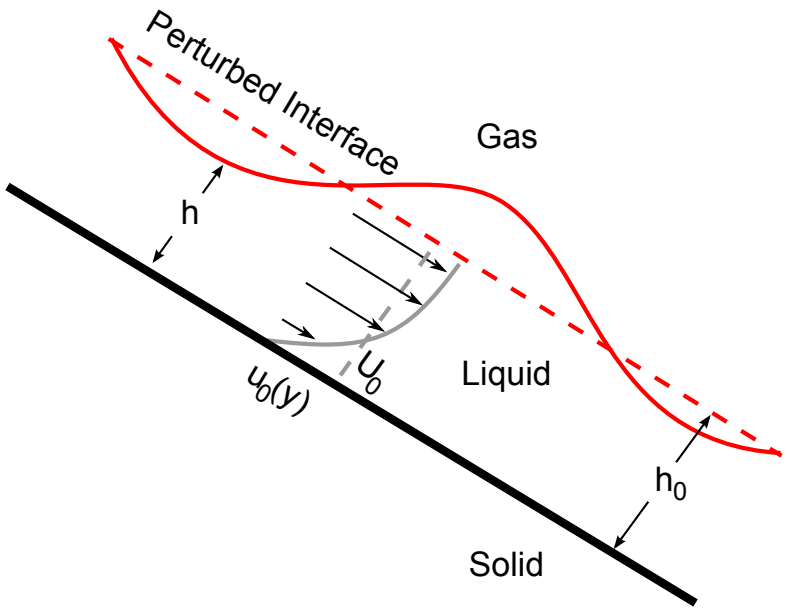

Figure 6.2: Schematic of flow down a slide as examined by Christodoulou & Scriven[20]. A free interface, with height h is perturbed from its planar base state (dashed), with height h_0. The fully developed flow on the slide is a function $u(x, y)$ (represented by arrows) whose mean is U_0.

the average velocity in the fluid on the slide. Observe that if We_0 were rewritten assuming h_0 is equivalent to G and U_0 is equivalent to U, then $We_0 = 2We$ and the proportionality constants are only off by ten percent, as $1/C_{HB} = 12.5$ and $2/C_0 \approx 11.48$. This scenario differs somewhat from the USM in PFMS, but the important physics in slide coating may be able to inform the essential physics required for successful modeling of this mechanism.

In Chap. [2], we showed the surface topology of both HB and CW acquired by optical profilometry.

6.2 Dynamics of Coupled Cylindrical Menisci

Chapter [3] examines the stability and dynamics of coupled cylindrical-cap menisci, and the regime for which this two-dimensional analysis should be valid is reported. This study was motivated by the oscillations of the USM seen in the CW defect. While the 2D static stability and phase-plane dynamics closely compare to previous work on coupled spherical-caps, the weakly nonlinear analysis of finite amplitude dynamics is new, and may be adapted to similar geometries. The scaled frequencies range from $0 - 1.6$, where the frequency of 1.6 appears for the limit of zero-volume and the frequency of 0 appears at the semi-circular limit. These frequencies are all smaller than the CW frequency of $1.9 - 2$.

Further, this model only captures center-of-mass (COM) motions. Byrne et al observed that the average deviation of the USM had 2 nodes (i.e. deviations from the equilibrium profile exhibited 2 crossings of the equilibrium shape). Thus, it is not expected that COM motions should capture the frequency of the observed oscillations.

6.3 Gap Expansion

Chapter [4] seeks to elucidates the dynamics of gap expansion, first through a careful treatment of the mechanics leading to previous models, and then by adapting the governing equations to capture higher-order dynamics observed in the data. Variations in the gap lead to variations in thermal loading of the substrate, and this results in variable expansion of the wheel, a phenomenon previously captured

through empirical fitting.

The piece-wise expansion model developed in Sec. [4.5.1] captures the decaying amplitude of oscillations which result from differential expansion. However, this model does not capture the increasing amplitude of the secondary oscillations apparent in $G(t)$. It is likely that this secondary oscillation results from the relative expansion of the length of each segment neglected by assuming that $1+\epsilon_\phi \approx 1$. This claim is supported by the increasing deviation between predicted and observed $G(t)$ as the throughout the cast. The nonlinear effect of the small-strain assumption might be captured by a full solution to Eq. [4.19] in Sec. [4.5.1] or Eq. [4.30] in Sec. [4.5.2].

6.4 Experimental Apparatus and Methodology

Chapter [5] documents the changes made to the experimental methodologies and the new equipment that has been acquired. The new high-speed imaging system (HSIS) and surface roughness analyzer (SRA) (both courtesy of Hitachi-Metglas, Inc.) should further elucidate the dynamics of the melt puddle.

The HSIS has dramatically improved puddle imaging capabilities. Most notably, both spatial and temporal resolution can be increased by an order of magnitude. Increased resolution will undoubtedly improve sensitive measurements of dynamic geometric quantites, e.g. puddle length and contact angle. In Sec. [5.3.3], it was demonstrated how increased image resolution can improve the study of important puddle physics captured by inferred properties, such as solidification velocity.

Image analysis may also reveal transitions to the topology of flow in the puddle, as predicted by previous studies (c.f. Appendix [B]). In Sec. [5.3.2], a preliminary study of contact angle dynamics was performed. A parametric study of dynamic contact angle should reveal whether it is determined by the melt/substrate wetting or solidification, as discussed in Sec. [6.1].

The SRA is being used in a current study of defect morphology as a function of cast parameters. Determining the parametric dependence of micron-scale defect morphology should elucidate the relationship between micrometer-, millimeter- and meter-scale physics as they relate to defect formation. The previous study of CW proposed that oscillations of the USM resulted in heat-transfer interruptions[12]. For this to be true, surface tension and inertia should effect micrometer-scale dynamics. In contrast, if defect morphology is independent of the currently known defect physics, then micrometer-scale disturbances likely lead to the macroscopic oscillations.

Appendices

Appendix A

Experimental Data

Table A.1: Table of experimental data for PFMS in OH 101 since Spring 2007.

Cast ID	U (m/s)	G (mm)	T (mm)	$Mass$ (kg)	We	PI
ACSU10-01	5.73	1.016	0.225	492	44.56	1.146
ACSU10-02	5.73	0.762	0.067	492	33.63	0.986
ACSU10-03	7.00	0.508	0.138	441	34.14	0.766
ACSU10-04	9.55	1.016	0.119	402	127.13	1.325
ACSU10-05	9.55	1.016	0.102	385	127.7	1.347
ACSU10-06	9.55	1.016	0.095	393	127.12	1.351
ACSU10-07	9.55	1.016		428	127.42	1.588
ACSU10-08	9.55	1.016	0.123	425	127.41	1.345
ACSU10-09	9.55	1.016		334	127.45	1.47
ACSU10-10	9.55	1.016		394	127.69	1.527
ACSU10-11	9.55	0.762		345	95.15	
ACSU10-12	9.55	0.762		485	95.88	
ACSU10-13	9.55	0.762		440	96.12	
ACSU10-14	9.55	0.762		295	95.65	

Notes:
[i] 99% Al; [ii] 13.2, [iii] 14.8, [iv] 18.1 and [v] 21% Si (for Al-x Si);
[vi] Al-7% Si-3.5% Mg; [vii] W = 2.5 mm; [viii] B = 3 mm;
[ix] 3.5, [x] 4.5, [xi] 4.8, [xii] 5 and [xiii] 7% Bi (for Al-7% Si-x Bi);
[xiv] Rounded, [xv] notched and [xvi] slanted upstream nozzle edge.

Continued on next page

Table A.1 – continued from previous page

Cast ID	U (m/s)	G (mm)	T (mm)	$Mass$ (kg)	We	PI
ACSU10-15	9.55	0.762		462	95.53	
CJSU10-01	4.78	0.508		492	16.33	0.619
CJSU10-02	4.78	0.508	0.156	621	16.32	0.565
CJSU10-03	4.78	0.508	0.107	481	15.98	0.612
CJSU10-04	9.55	1.016	0.122	688	126.71	1.332
CJSU10-05	9.55	1.016	0.119	527	127.51	1.075
CJSU10-06[xiv]	9.55	1.016	0.088	443	127.84	0.833
CJSU10-07[xiv]	9.55	1.016	0.123	349	127.11	1.335
CJSU10-08	4.78	1.016	0.227	346	31.81	1.219
CJSU10-09	4.78	1.016	0.147	484	31.49	1.207
CJSU10-10	5.73	1.016	0.191	514	46.69	1.232
CJSU10-11	5.73	0.762	0.115	432	34.2	1.254
CJSU10-12	9.55	1.016	0.094	419	127.59	1.186
CJSU10-13	5.73	0.762	0.097	357	34.48	0.919
CJSU10-14	5.73	0.762	0.086	554	34.23	0.852
CJSU10-15	7.00	1.016	0.110	441	68.58	1.313
CJSU10-16	7.00	1.016	0.112	393	51.33	1.022
CJSU10-17	11.46	1.016	0.095	448	175.46	1.591
CJSU10-18	11.46	1.016	0.076	383	184.26	1.173
CJSU10-19	11.46	1.016	0.086	415	183.54	1.345
CJSU10-20	6.05	0.762	0.211	432	38.17	1.157
CJSU10-21	6.05	0.762	0.145	418	38.36	1.014
CJSU10-22	7.00	0.508	0.068	470	34.41	0.843
CJSU10-23	9.55	1.016	0.112	502	127.51	1.368
CJSU10-24	9.55	0.254	0.052	403	31.95	0.438
CJSU10-25	9.55	0.254	0.044	397	31.72	0.419
CJSU10-26	9.55	0.508	0.069	344	63.83	0.777
CJSU10-27	9.55	0.508	0.054	308	63.42	0.798
CJSU10-28	9.55	0.381	0.073	435	47.68	0.643
CJSU10-29	9.55	0.381	0.055	371	48.06	0.641
CJSU10-30	9.55	0.508	0.045	498	63.8	0.867
CJSU10-31	9.55	1.016		397	127.23	1.648
CJSU10-32	9.55	1.016		402	127.42	1.554
CJSU10-33	7.96	1.016		357	88.74	1.539
CJSU10-34	7.00	1.016		433	68.6	1.581

Notes:
[i] 99% Al; [ii] 13.2, [iii] 14.8, [iv] 18.1 and [v] 21% Si (for Al-x Si);
[vi] Al-7% Si-3.5% Mg; [vii] W = 2.5 mm; [viii] B = 3 mm;
[ix] 3.5, [x] 4.5, [xi] 4.8, [xii] 5 and [xiii] 7% Bi (for Al-7% Si-x Bi);
[xiv] Rounded, [xv] notched and [xvi] slanted upstream nozzle edge.

Continued on next page

Table A.1 – continued from previous page

Cast ID	U (m/s)	G (mm)	T (mm)	$Mass$ (kg)	We	PI
CJSU10-35	9.55	1.016		450	127.61	2.268
CJSU10-36	9.55	1.016		353	127.39	1.342
CJSU10-37	9.55	1.016		549	128.08	2.157
CJSU10-38	9.55	1.016		534	127.91	1.652
CJSU10-39	9.55	1.016	0.14	283	127.42	1.197
ACSU09-01	7.96	1.905		288	166.93	1.859
ACSU09-02	7.96	1.905	0.156	224	164.12	1.796
ACSU09-03[ii]	9.55	1.016	0.121	351	126.49	1.165
ACSU09-04[iii]	9.55	1.016	0.121	416	126.41	1.277
ACSU09-05[iv]	9.55	1.016	0.096	528	126.4	1.327
ACSU09-06[v]	9.55	1.016	0.086	416	127.2	1.295
ACSU09-07	6.05	2.54		404		
ACSU09-08	7.96	1.905		360		
ACSU09-09	6.05	2.54		307		
ACSU09-10	11.94	0.254		404		
ACSU09-11	11.94	0.254		347		
ACSU09-12[xi]	9.55	0.762	0.094	603	180.16	1.883
ACSU09-13[xii]	10.35	0.762	0.110	559	216.44	1.876
ACSU09-14	9.55	0.762		430		
ACSU09-15	9.55	0.762	0.115	414	96.55	1.101
ACSU09-16	7.96	0.508		525		
ACSU09-17[ix]	7.96	0.508	0.084	454	80.94	0.897
ACSU09-18	7.96	0.610		446		
ACSU09-19	9.55	1.016	0.102	469	128.68	1.191
ACSU09-20	9.55	1.016	0.112	501	127.73	1.196
ACSU09-21	9.55	1.016	0.093	510	127.88	1.185
ACSU09-22	7.96	0.508	0.054	434	59.04	0.802
ACSU09-23	7.96	0.762		453		
CJSU09-01	9.55	1.016	0.151	338	124.06	1.23
CJSU09-02	9.55	1.016	0.119	345	126.87	
CJSU09-03	9.55	1.016		532	128.2	1.171
CJSU09-04	9.55	1.016	0.144	361	127.43	1.232
CJSU09-05	9.55	1.016	0.115	375	126.7	1.236
CJSU09-06	9.55	1.016	0.122	349	128.19	1.248
CJSU09-07	7.96	1.016		398		

Notes:
[i] 99% Al; [ii] 13.2, [iii] 14.8, [iv] 18.1 and [v] 21% Si (for Al-x Si);
[vi] Al-7% Si-3.5% Mg; [vii] W = 2.5 mm; [viii] B = 3 mm;
[ix] 3.5, [x] 4.5, [xi] 4.8, [xii] 5 and [xiii] 7% Bi (for Al-7% Si-x Bi);
[xiv] Rounded, [xv] notched and [xvi] slanted upstream nozzle edge.

Continued on next page

Table A.1 – continued from previous page

Cast ID	U (m/s)	G (mm)	T (mm)	$Mass$ (kg)	We	PI
CJSU09-08	7.96	1.016		528		
CJSU09-09	7.96	1.016		360		
CJSU09-10	6.37	1.016		345		
CJSU09-11	6.05	2.54		365		
CJSU09-12	6.37	1.016		376		
CJSU09-13	4.78	1.016		324		
CJSU09-14	4.78	1.016		378		
CJSU09-15	3.18	1.016	0.365	335	13.96	1.058
CJSU09-16	3.18	1.016		334		
CJSU09-17	6.05	1.905		342		
CJSU09-18	3.18	1.016		358		
CJSU09-19	9.55	0.610		386		
CJSU09-20	9.55	0.610		352		
CJSU09-21	6.37	0.610		354		
CJSU09-22	6.37	0.610		385		
CJSU09-23	6.37	0.610		419		
CJSU09-24	6.37	0.610		326		
CJSU09-25	9.55	0.610		436		
CJSU09-26	9.55	0.610		426		
CJSU09-27	9.55	0.457		386		
CJSU09-28	9.55	0.762		379		
CJSU09-29	9.55	0.762		586		
CJSU09-30[x]	6.37	1.016	0.197	558	109.73	2.261
CJSU09-31[ix]	9.55	1.016	0.143	613	245.09	2.392
CJSU09-32	9.55	1.016		464		
CJSU09-33	9.55	1.016	0.103	390	128.53	1.137
CJSU09-34	9.55	1.016		599		
CJSU09-35	7.96	0.762		386		
CJSU09-36	7.96	0.762		564		
CJSU09-37[xiv]	7.96	0.762	0.125	356	66.65	0.733
CJSU09-38[xiii]	7.96	1.016	0.169	409	173.11	1.989
CJSU09-39[xiii]	7.96	1.016	0.161	579	169.62	1.943
ACSP09-01	9.55	0.762		324		
ACSP09-02	9.55	0.762		320		
CJSP09-01	9.55	0.762		324		

Notes:
[i] 99% Al; [ii] 13.2, [iii] 14.8, [iv] 18.1 and [v] 21% Si (for Al-x Si);
[vi] Al-7% Si-3.5% Mg; [vii] W = 2.5 mm; [viii] B = 3 mm;
[ix] 3.5, [x] 4.5, [xi] 4.8, [xii] 5 and [xiii] 7% Bi (for Al-7% Si-x Bi);
[xiv] Rounded, [xv] notched and [xvi] slanted upstream nozzle edge.

Continued on next page

Table A.1 – continued from previous page

Cast ID	U (m/s)	G (mm)	T (mm)	$Mass$ (kg)	We	PI
ACFA08-01	9.55	0.457	0.074	240	57.98	1.138
ACFA08-02[i]	9.55	0.762	0.077	496	96.54	1.309
ACSU08-01	7.96	1.016	0.116	397	87.81	1.109
ACSU08-02[xv]	9.55	1.016		428	127.55	1.094
ACSU08-03[xv]	9.55	1.016	0.100	407	128.61	0.693
ACSU08-04[xv]	9.55	1.016	0.127	397	127.46	1.203
ACSU08-05	9.55	1.016	0.123	384	127.53	1.138
ACSU08-06	9.55	1.016	0.082	438	95.9	1.02
ACSU08-07	7.96	1.016	0.104	608	89.03	1.024
ACSU08-08	7.00	0.762	0.085	399	38.06	0.708
ACSU08-09	7.96	1.016	0.098	386	50.75	0.898
ACSU08-10	9.55	1.016	0.069	599	126.87	1.109
ACSU08-11	9.55	1.016		440		
ACSU08-12	7.96	1.016	0.109	419	87.96	1.019
ACSU08-13	9.55	1.016	0.082	376	50.75	1.056
ACSU08-14	9.55	1.016	0.118	418	128.27	0.962
ACSU08-15	9.55	0.762	0.076	552	97.58	1.224
ACSU08-16	7.96	0.762	0.09	451	66.88	1.24
ACSU08-17	7.96	1.016	0.116	415	88.34	1.58
ACSU08-18	7.96	0.762	0.071	623	66.3	1.173
ACSU08-19	9.55	0.254		547		
ACSU08-20	9.55	0.508	0.074	230	31.79	0.555
FHSU08-01	7.96	1.016	0.105	351	89.99	0.987
FHSU08-02	7.96	1.016	0.122	345	89.25	1.196
FHSU08-03	7.96	1.016	0.113	359	88.84	0.973
FHSU08-04	7.96	1.016	0.138	436	89.07	1.492
FHSU08-05	7.96	1.016		431	81.61	1.744
FHSU08-06	7.96	1.016		421	111.16	3.385
FHSU08-07	9.55	1.016	0.108	440	126.43	1.346
FHSU08-08	9.55	1.016	0.095	469	125.55	1.321
FHSU08-09	9.55	1.016	0.093	447	130.06	1.341
FHSU08-10	9.55	1.016		453	133.06	1.113
FHSU08-11	9.55	0.787	0.089	419	98.08	1.008
FHSU08-12	9.55	0.610	0.069	419	75.6	0.789
FHSU08-13	9.55	0.610	0.074	411	77.63	0.718

Notes:
[i] 99% Al; [ii] 13.2, [iii] 14.8, [iv] 18.1 and [v] 21% Si (for Al-x Si);
[vi] Al-7% Si-3.5% Mg; [vii] W = 2.5 mm; [viii] B = 3 mm;
[ix] 3.5, [x] 4.5, [xi] 4.8, [xii] 5 and [xiii] 7% Bi (for Al-7% Si-x Bi);
[xiv] Rounded, [xv] notched and [xvi] slanted upstream nozzle edge.

Continued on next page

Table A.1 – continued from previous page

Cast ID	U (m/s)	G (mm)	T (mm)	$Mass$ (kg)	We	PI
FHSU08-14	9.55	0.762	0.085	465	94.77	0.979
FHSU08-15	9.55	0.762	0.074	392	100.33	0.986
FHSU08-16	9.55	0.762	0.112	308	97.49	0.875
FHSU08-17	9.55	0.762	0.076	393	95.95	1.017
FHSU08-18	9.55	0.762	0.077	416	96.6	1.053
FHSU08-19	9.55	0.762	0.091	468	95.15	
FHSU08-20	6.05	1.016	0.121	441	50.75	0.974
FHSU08-21	7.00	0.762	0.086	399	51.12	0.71
FHSU08-22	7.00	0.762	0.100	399	51.12	0.71
FHSU08-23	7.96	1.016	0.091	546	87.92	1.026
FHSU08-24	9.55	1.016	0.094	407	127.44	1.086
FHSU08-25[xvi]	6.37	1.016	0.148	457	58.53	0.99
FHSU08-26[xvi]	6.37	1.016	0.193	376	57.24	0.921
FHSU08-27	9.55	1.016		365	50.75	1.048
FHSU08-28	9.55	1.016	0.113	377	126.21	1.228
FHSU08-29[viii]	9.55	1.016	0.079	429	126.52	1.001
FHSU08-30[xvi]	9.55	1.016	0.112	393	126.06	0.949
FHSU08-31	9.55	1.016	0.078	441	117.96	1.107
FHSU08-32	9.55	0.762	0.077	445	98.56	0.98
FHSU08-33	7.96	0.762	0.110	519	65.62	1.149
FHSU08-34	7.96	0.762	0.100	448	66.11	1.213
FHSU08-35	7.96	0.762	0.106	411	66.74	1.194
FHSU08-36	7.96	1.016	0.138	389	88.22	1.528
FHSU08-37	7.96	0.762	0.102	427	63.99	0.84
FHSU08-38	6.05	0.762	0.113	427	39.58	0.742
CDSP08-01	7.96	0.762	0.103	402	65.76	0.71
CDSP08-02	7.96	0.762		503	66.27	0.862
CDSU07-01	7.96	0.610	0.079	728	53.42	0.63
CDSU07-02	7.96	0.787		705	67.97	1.006
CDSU07-03	7.96	0.787		415	68.37	0.841
CDSU07-04	7.96	0.787		405	69.	0.835
CDSU07-05	7.96	0.787		623	68.37	0.959
CDSU07-06	7.96	0.787	0.099	669	68.14	0.805
CDSU07-07	7.96	0.787	0.094	663	68.48	0.8
CDSU07-08	7.96	0.787	0.09	664	69.	0.808

Notes:
[i] 99% Al; [ii] 13.2, [iii] 14.8, [iv] 18.1 and [v] 21% Si (for Al-x Si);
[vi] Al-7% Si-3.5% Mg; [vii] W = 2.5 mm; [viii] B = 3 mm;
[ix] 3.5, [x] 4.5, [xi] 4.8, [xii] 5 and [xiii] 7% Bi (for Al-7% Si-x Bi);
[xiv] Rounded, [xv] notched and [xvi] slanted upstream nozzle edge.

Continued on next page

Table A.1 – continued from previous page

Cast ID	U (m/s)	G (mm)	T (mm)	$Mass$ (kg)	We	PI
CDSU07-09	7.96	0.787		378	68.5	0.82
CDSU07-10	7.96	0.787		371	68.67	0.816
CDSU07-11	7.96	0.787		377	68.22	0.819
CDSU07-12	7.96	0.787		644	68.4	0.971
CDSU07-13	7.96	0.787		362	68.45	0.81
CDSU07-14	7.96	0.787		374	68.4	0.817
CDSU07-15	7.96	0.787		370	68.25	0.815
CDSU07-16	7.96	0.787		367	68.4	0.813
CDSU07-17	7.96	0.787		357	68.14	0.808
CDSU07-18	7.96	0.787		628	68.67	1.582
CDSU07-19	7.96	1.041		645	90.69	1.285
CDSU07-20	7.96	0.787		334	67.97	0.795
CDSU07-21	7.96	0.787		318	68.3	0.785
CDSU07-22	6.37	0.610	0.082	649	33.82	1.118
CDSU07-23	6.37	0.787	0.105	655	43.44	0.831
CDSU07-24	8.18	0.787		613	61.62	0.953
CDSU07-25	8.75	0.787	0.152	467	76.8	1.879
CDSU07-26	7.8	0.787	0.094	560	65.65	1.608
CDSU07-27	6.69	0.787	0.138	622	63.31	1.516
CDSU07-28	8.69	0.787	0.124	702	81.5	1.505
CDSU07-29	7.96	0.787	0.137	623	68.65	0.79
CDSU07-30	7.96	0.457	0.119	647	39.28	1.299
CDSU07-31	7.96	0.457	0.094	625	39.47	1.419
CDSU07-32	7.96	0.787	0.12	689	68.66	1.222
CDSU07-33	7.96	0.787	0.137	564	69.39	1.556
CDSU07-34	7.96	0.610	0.118	598	66.71	1.643
CDSU07-35	7.96	0.610	0.09	600	68.93	1.649
CDSU07-36	7.8	0.610	0.115	604	50.78	1.373
CDSU07-37	7.96	0.610	0.091	611	67.02	1.758
CDSU07-38	7.96	0.610	0.098	582	52.11	1.311
CDSU07-39[vii]	7.96	0.610	0.087	355	53.07	1.245
CDSU07-40[vii]	7.96	0.610	0.108	339	52.89	1.225
CDSU07-41[vii]	7.96	0.610	0.108	232	52.84	1.348
CDSU07-42	6.37	0.762	0.149	497	41.95	1.46
CDSU07-43	6.37	0.762	0.13	555	42.2	1.563

Notes:
[i] 99% Al; [ii] 13.2, [iii] 14.8, [iv] 18.1 and [v] 21% Si (for Al-x Si);
[vi] Al-7% Si-3.5% Mg; [vii] W = 2.5 mm; [viii] B = 3 mm;
[ix] 3.5, [x] 4.5, [xi] 4.8, [xii] 5 and [xiii] 7% Bi (for Al-7% Si-x Bi);
[xiv] Rounded, [xv] notched and [xvi] slanted upstream nozzle edge.

Continued on next page

Table A.1 – continued from previous page

Cast ID	U (m/s)	G (mm)	T (mm)	$Mass$ (kg)	We	PI
CDSU07-44	6.37	0.762	0.187	562	42.22	1.518
CDSU07-45	6.37	0.762	0.162	561	38.54	1.377
CDSU07-46	6.37	0.762	0.158	575	42.47	1.536
CDSU07-47	6.37	0.762	0.148	452	42.41	1.613
CDSU07-48	6.37	0.762	0.191	448	35.25	1.609
CDSU07-49[vii]	9.55	0.762	0.083	266	95.43	1.252
CDSU07-50	6.37	0.762	0.159	593	43.61	1.562
CDSU07-51	9.55	0.508	0.105	600	61.58	1.282
CDSU07-52	6.37	0.762	0.168	604	42.31	1.473
CDSU07-53	6.37	0.762	0.125	523	41.23	1.168
CDSP07-01	5.73	0.610	0.116	556	28.08	
CDSP07-02	9.55	0.610		567	76.92	0.717
CDSP07-03	6.37	0.787		580	44.16	0.935
CDSP07-04	6.37	0.610		473	34.19	0.676
CDSP07-05	6.37	0.610		469	34.19	0.675
CDSP07-06	6.37	0.610		490	34.19	0.684
CDSP07-07	6.37	0.610		507	34.19	0.691
CDSP07-08	7.96	0.610	0.086	540	53.42	0.581
CDSP07-09	7.96	0.610	0.072	657	53.42	0.615

Notes:
[i] 99% Al; [ii] 13.2, [iii] 14.8, [iv] 18.1 and [v] 21% Si (for Al-x Si);
[vi] Al-7% Si-3.5% Mg; [vii] W = 2.5 mm; [viii] B = 3 mm;
[ix] 3.5, [x] 4.5, [xi] 4.8, [xii] 5 and [xiii] 7% Bi (for Al-7% Si-x Bi);
[xiv] Rounded, [xv] notched and [xvi] slanted upstream nozzle edge.

Appendix B

Detachment of the Downstream Meniscus

Previous studies have predicted the slope of the DSM[63, 5]. The development of [63] is briefly recapitulated. If the puddle is quasi-steady, the flow within may be represented by the schematic in Fig. [B.1]. A mass balance about the puddle obtains puddle-averaged velocities required to meet the mass flow rate of

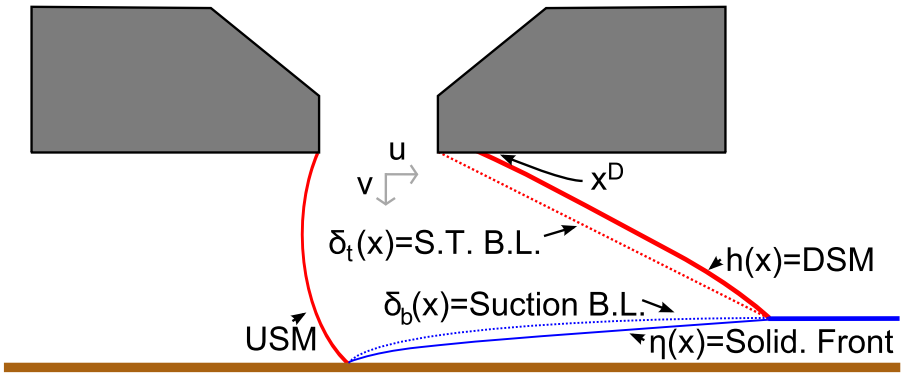

Figure B.1: Schematic of the puddle when flow is quasi-steady.

product, $\rho_s TU$. Fluid enters the puddle with an average velocity of $(u_x, u_y) = (0, u_{in} = TU/B)$, and thus, the initial fluid momentum in the x-direction is zero. The bulk of the fluid turns downstream reaching an average horizontal velocity of $\bar{u} = \rho_{sl} TU/G$. This bulk feeds two boundary layers, an upper surface tension boundary layer where fluid approaches the DSM and a lower suction boundary layer feeding the solidification front, where fluid must accelerate to $u_x = U$. As $U >> \bar{u}$, the force placed upon the flow from this boundary layer is appreciable, but the high Re indicates that the viscous length scale is small relative to the convection of momentum, so the effect on the bulk flow may still be small. To first order, the x-momentum balance in the bulk is

$$\frac{d}{dx}\int_{\eta(x)+\delta_b(x)}^{h(x)-\delta_t(x)} \rho_l u_x^2 dy + \int_{\eta(x)+\delta_b(x)}^{h(x)-\delta_t(x)} \frac{\partial P}{\partial x} dy - \rho_l \left(u_x u_y\right)_{h+\delta_b} = 0. \tag{B.1}$$

A scaling analysis of the mass balance indicates three unknown scales, u, δ_b and $u_y|_{h+\delta_b}$. Assuming $Re >> G/T$ and $U >> \bar{u}$ shows that $\delta_b, \delta_t << T$; i.e. $H(x) >> \delta_b$ and $h(x) >> \delta t$. The mass balance in the y-direction reveals that $u_y|_{h+\delta_b} \approx -\rho_{sl} U dh/dx$. Neglecting terms of $O(\bar{u})$ or smaller, Eq. [B.1] becomes

$$\frac{d}{dx}\int_{\eta(x)}^{h(x)} \rho_l u^2 dy + \int_{\eta(x)}^{h(x)} \frac{\partial P}{\partial x} dy - \rho_s U \frac{dh}{dx} u|_h = 0. \tag{B.2}$$

The y-momentum balance, not shown here, is dominated by the pressure terms, and to leading order is simply $P_h - P_\eta = 0$[63]. Thus there is no appreciable dependence of P on y, or $\partial P/\partial x \equiv dP/dx$. Further development leads to the first order solution for the DSM,

$$h_0(x) = 1 + \frac{\rho_s}{\rho_l \bar{u}(x^D)}(\eta_0(x^D) - \eta_0(x)). \tag{B.3}$$

where $\bar{u}(x^D) = G\sqrt{2\Delta P/\rho_l U^2}$ is given by a well-known Bernoulli-based correlation [37, 39]. The detachment point x^D may be extrapolated from the measurement of $h(x,t) = m(t)x + b(t)$ in Sec. [5.3.3], and is shown in Fig. [B.2].

The DSM appears to detach from the inlet nozzle midway through the cast. This detachment coincides with the deviation of the slope of Eq. [B.3], $dh_0/dx = \rho_s T/\rho_l \bar{u}(x^D)L$, from the measured slope, $\partial h/\partial x = m(t)$, as shown in Fig. [B.3]. As the scaling result should remain unchanged, the simultaneous detachment and failure of the predicted DSM slope suggests that detachment coincides with a failure of $\bar{u}(x^D) = G\sqrt{2\Delta P/\rho_l U^2}$. Reed 2001 proposes that the streamwise pressure gradient becomes zero at leading order below the detachment point, and Bichi 2008 suggests that this results in vortex shedding. These conditions are consistent with the failure of the irrotational assumption that allows the Bernoulli balance to predict the pressure gradients, and supports the streamlines predicted by previous studies; however, further experimental investigation is necessary before any strong conclusions can be made.

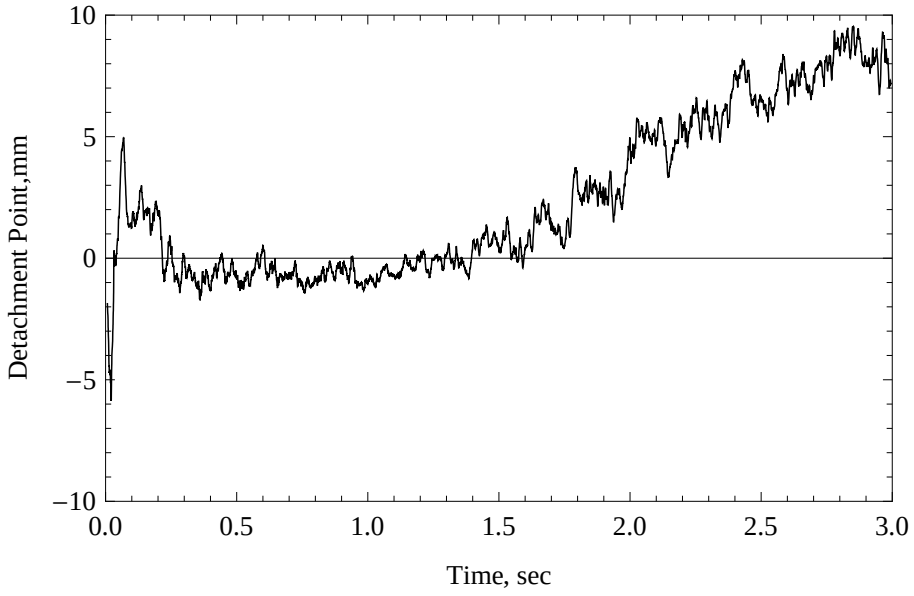

Figure B.2: Calculated $x^D(t)$.

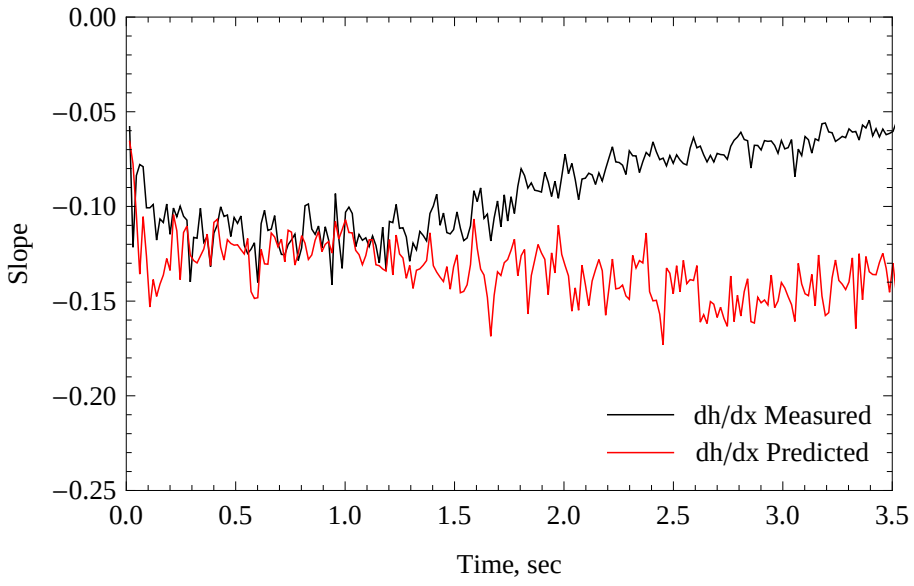

Figure B.3: Measured slope of $h(x,t)$ versus prediction from Bernoulli balance.

Appendix C

Dynamics of a Conservative Oscillator with Gravity- and Capillary-Induced Forces.

C.1 Overview

Conservative oscillators are a frequently studied and heavily documented subject, and simple models often provide insight into the behavior of complicated systems. A fairly simple potential function may exhibit complicated bifurcation behavior upon variation of parameters. Here we develop a simple model to explore the physics of a particular pairing of forces: gravity acts upon a liquid in one region of the fluid, and capillary forces are dominant in another region. We do so in search of frequencies near those of a common defect in a metal casting process.

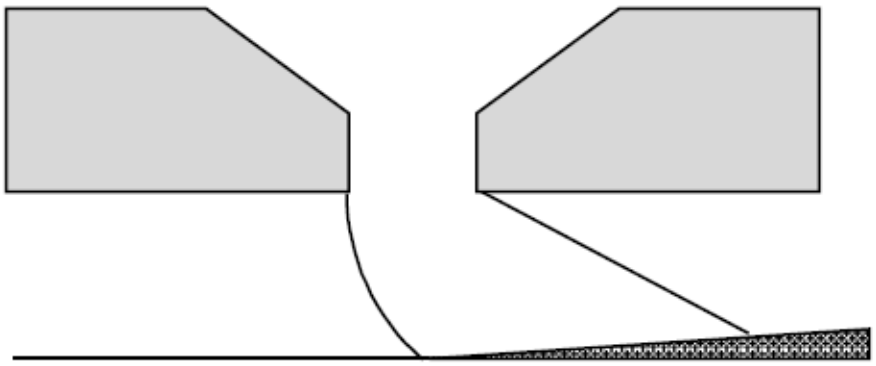

Figure C.1: Representative sketch of contact zone during a cast with low over-pressure[12].

C.2 Motivation

A metal casting process known as planar-flow melt spinning involves the forced extrusion of molten metal from a reservoir onto a moving substrate. A puddle of liquid is formed in the contact zone. Experiments show that the herringbone casting-defect often occurs in casts in which a low (but greater than atmospheric) pressure is applied to the liquid reservoir [12]. In this regime, the liquid-gas interface often forms a constrained meniscus in the puddle region, justifying a pinned contact condition with a surface energy dominated by capillary force. Also, when the applied pressure is low, the hydrostatic pressure of the liquid reservoir is more likely to contribute to the behavior of the fluid in the puddle region.

To examine the aforementioned behavior, a simplified system is imagined, in which a reservoir of liquid sits above a confined puddle. The reservoir of liquid is taken to have constant radius, and be acted upon by the force of gravity. Solid-liquid and liquid-gas interactions are neglected at interfaces of the reservoir for

simplicity. This does not depart greatly from the experimental scenario, as the typical capillary pressure on the liquid reservoir is small relative to hydrostatic pressure, on the orders of 10 and 1000 Pa, respectively, only reaching comparable magnitudes in the final stages of the cast[10].

The confined puddle is imagined as a squat cylindrical plug of liquid, with a large radius-to-height ratio. Volume and momentum are exchanged freely with the reservoir. When acted upon by the hydrostatic pressure from the reservoir, its interface deforms to a corresponding pressure value. The deformed interface shapes are confined to circular cap cross-sections acted upon by a Young-Laplace force, for simplicity of calculations. The small height of the puddle places the surface in a capillary dominated regime, allowing us to neglect the effects of gravity in this region.

In the following section, a model is proposed from these assumptions, neglecting viscosity and all other irreversible energy losses.

C.3 Dynamical System

The simplified model for the puddle region is sketched in Fig. (C.2). The system is taken to be axisymmetric for ease of calculation. Newton's law for the center-of-mass takes the form $\frac{d}{dt}\left(m\frac{dy_c}{dt}\right) = \sum Forces$, where y_c is the center-of-mass of the system. For simplicity, the system is divided into two elements, the puddle and the reservoir, with volumes V_1 and V_2 and centers-of-mass y_1 and y_2, respectively. Total volume $V_T = V_1 + V_2$ is taken to be constant, and the liquid is assumed

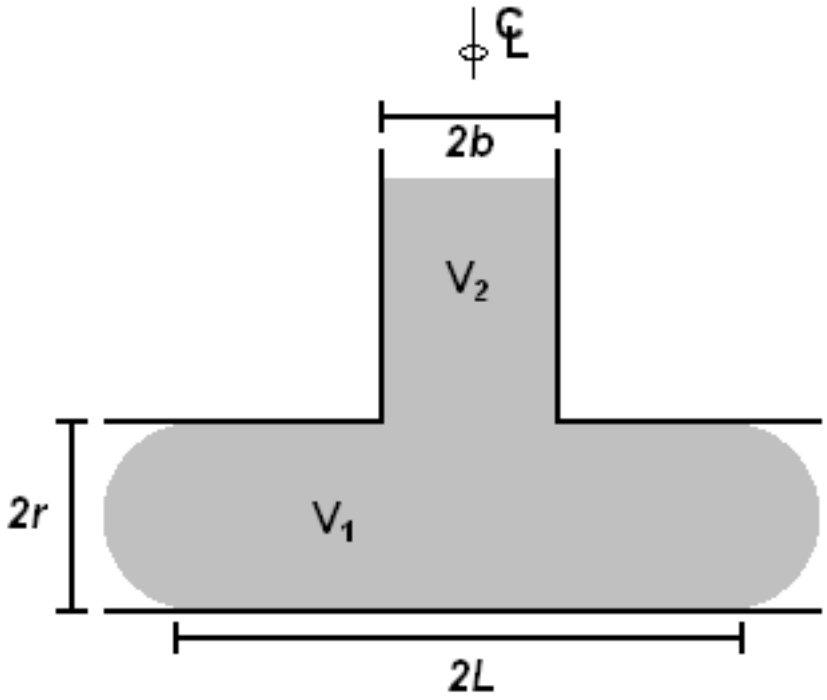

Figure C.2: Physical sketch of model system.

incompressible and of constant density, ρ, so the inertial term may be rewritten $\rho\frac{d^2}{dt^2}(V_T y_c)$. Note that $y_c = \frac{V_1 y_1 + V_2 y_2}{V_T}$, and that $y_1 = r$ and $y_2 = 2r + \frac{V_2}{2\pi b^2}$. Taking these facts with the constant volume constrant, the inertial term may be rewritten in terms of V_1 and system parameters.

The forces acting upon the center-of-mass, motivated in §C.2, may be represented as $\sum Forces = \frac{2\pi L r \sigma}{R_1} - \rho g V_2$, where R_1 is the radius of curvature of the circular cap cross section of element 1, σ is the surface tension associated with that interface, and g is the gravitational acceleration acting on element 2. It is convenient to redefine the system in terms of $V = V_1 - 2\pi L^2 r$, where V is the volume between the gas-liquid interface of element 1 and the cylinder defined by $2\pi L^2 r$. All volumes are scaled by $2\pi L^2 r$, time by $\sqrt{\rho r^2 L/\sigma}$, a capillary time scale, and lengths

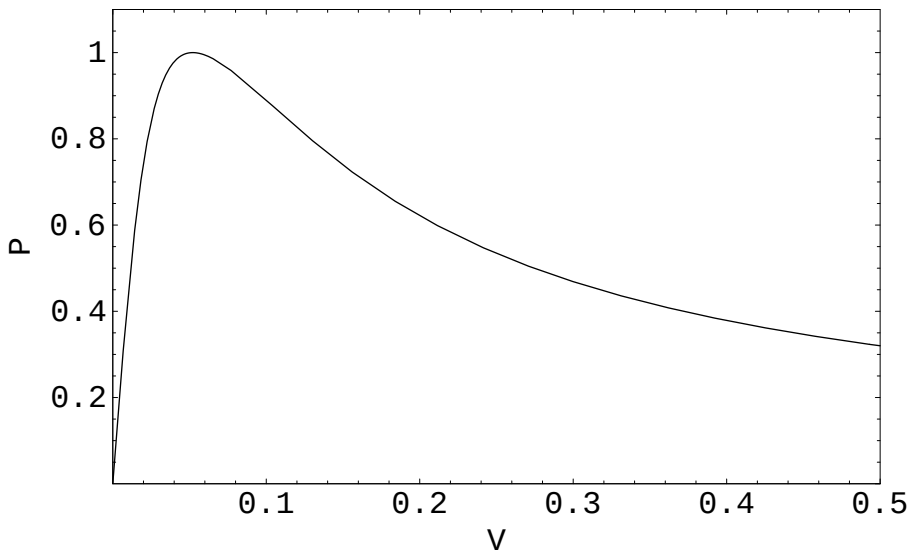

Figure C.3: Pressure versus volume, V.

by r. Newton's law becomes $\frac{d}{dt}\left[\left(1+\beta^2\left(\mu_2-V\right)\right)\dot{V}\right]=\mu_1\left(\mu_2-V\right)-P\left(V\right)$.

Here, $\beta=2L/b$ is constant and positive, $\mu_1=\rho rLg/\sigma$, $\mu_2=V_2+V$, and $P\left(V\right)$ is a nonlinear function of V. For our purposes, it was sufficient to construct $P(V)$ by numerical interpolation of pairs of $V(R_1)$ and $P(R_1)$ at a fixed $L=10$ and $r=1$. A plot of $P(V)$ is shown in Fig. (C.3). μ_1 represents a ratio of hydrostatic and capillary pressures, while μ_2 is the volume available to be exchanged between V and V_2.

C.4 Phase Plane

It is convenient to define $U = (1 + \beta^2 (\mu_2 - V)) \frac{dV}{dt}$. The dynamical system may then be written,

$$\begin{aligned} \dot{V} &= \frac{U}{(1 + \beta^2 (\mu_2 - V))} \\ \dot{U} &= \mu_1 (\mu_2 - V) - P(V) \end{aligned}$$

or $\dot{x} = f(x; \mu_1, \mu_2)$. The system admits equilibria when $U = 0$ and $\mu_1 (\mu_2 - V) - P(V) = 0$. Note, it is possible for multiple equilibria, but not gauranteed. In the following sections we explore these equilibria, and their stability. The system of equations has an associated Jacobian, $D_x f$. At equilibrium values of $f(x; \mu_1, \mu_2)$, $tr(D_x f) = 0$ and $det(D_x f) = -\frac{\mu_2 + D_V P}{1 + \beta^2 (\mu_2 - V)}$. The fact that $tr(D_x f) = 0$ is due to the conservative nature of the oscillator. As a result, there are purely imaginary eigenvalues when $det(D_x f) > 0$, but no Hopf bifurcations are observed. When $det(D_x f) > 0$, the associated equilibrium point is a center, and when $det(D_x f) < 0$, it is a saddle. A saddle-center bifurcation occurs when $D_x f$ becomes singular, or $\frac{\mu_2 + D_V P}{1 + \beta^2 (\mu_2 - V)} = 0$. The criteria that $f(x; \mu_1, \mu_2) = 0$ and $det(D_x f) = 0$ may be combined to parameterize the equilibria in terms of μ_2, $\mu_2 = V + \frac{P(V)}{\mu_1}$, which is plotted for several values in Fig. (C.4).

From this function, it is evident that for some values of μ_1, there exists an interval of μ_2 for which there are two equilibria. At small μ_2, a single center exists. As μ_2 is increased, a saddle-center bifurcation occurs, provided that $\frac{d\mu_2}{dV}$ passes smoothly through zero. In this region, three equilibria exist: two stable centers separated by a saddle. The stable and unstable manifolds of the saddle are connected by two homoclinic loops, forming a separatrix. Increasing μ_2 further

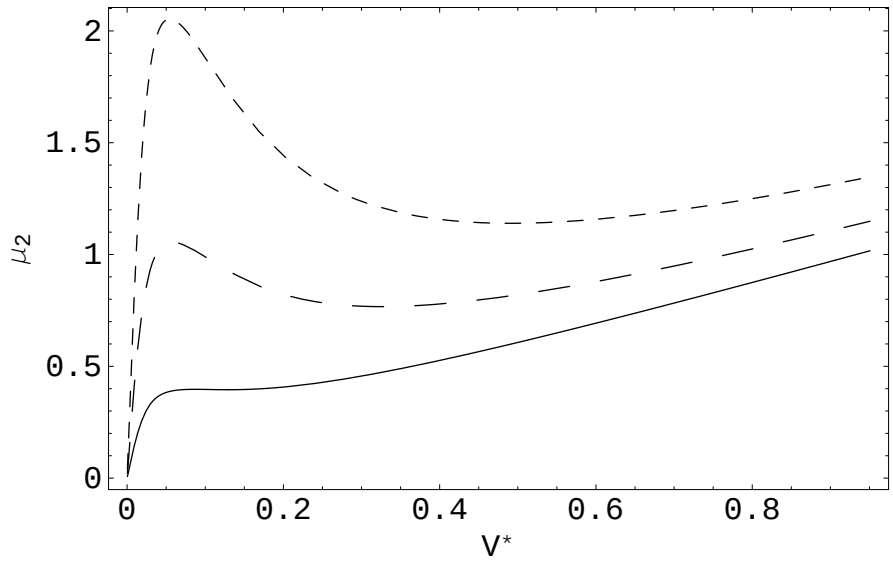

Figure C.4: Volume versus μ_2 for several values of μ_1. $\mu_1 = (0.5, 1, 3)$ as dashing increases.

will lead to the annihilation of the smaller two equilibria, leaving again a single center, but of relatively large magnitude. Characteristic phase portraits appear in Fig. (C.5).

A codimension 2 bifurcation is observed. The values of (μ_1, μ_2) at which these saddle-center bifurcations occur are given by the maxima and minima of the function $\mu_2(V)$ shown in Fig. (C.5). Finding these values, one recovers a cusp, shown in Fig. (C.6). Inside of the cusp, are the parameter values in which 3 equilibria coexist. Outside of the cusp, only one.

The frequencies of oscillation near each center, the ultimate goal of this analysis, may be estimated by linearizing the system around the equilibrium points, resulting in the estimate, $\omega(V^*) = \sqrt{\frac{\mu_1 + dP/dV(V^*)}{1+\beta^2(\mu_2 - V^*)}}$. The maximum frequency for small meniscus shapes is calculated to be two orders of magnitude less than those of the physical inspiration, and thus the physical pairing explored here is not likely

the cause.

C.5 Conclusion

It is evident from the model equations that variation of several other parameters may result in further unfolding of the system. Specifically, the value of L mediates the pressure term, which might ultimately result in a codimension 3 bifurcation of the cusp. These dynamics were not explored here.

The simple model developed here was shown to exhibit complicated dynamics on the phase plane, but much more complicated dynamics might be possible upon introduction of viscous damping. It seems the addition of a term effecting $tr(D_x f)$ may easily induce a Hopf bifurcation, and allow for the possibility of further degeneracy. Upon the addition of periodic forcing, one would expect the homoclinic loops, a structurally unstable feature, to disconnect, allowing the possibility of chaotic behavior in some regions of parameter space, homoclinic tangles may occur. The approach of Melnikov may be utilized to explore this possibility.

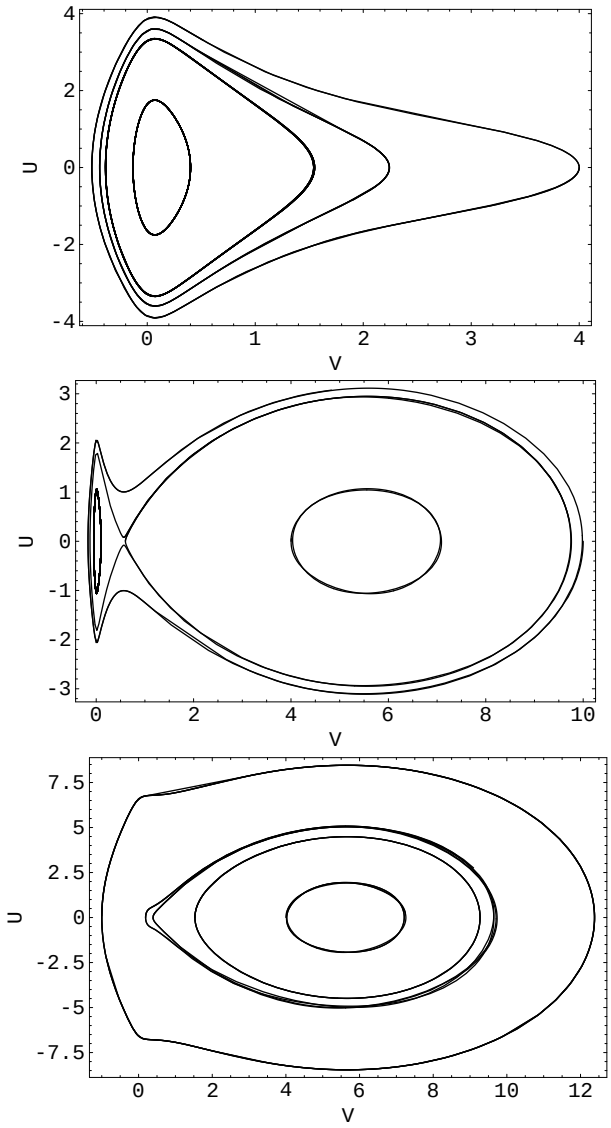

Figure C.5: Phase portraits with one small equilibrium, three equilibria, and one large equilibrium.

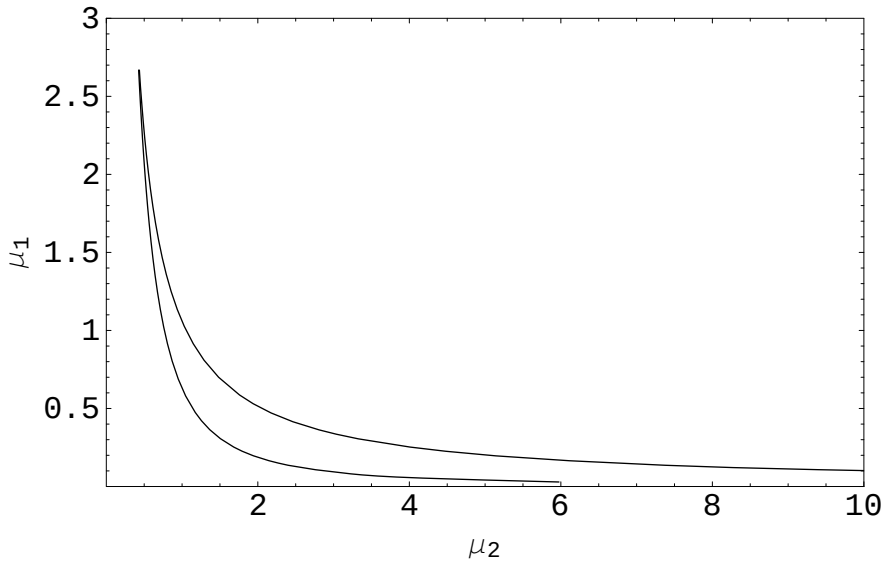

Figure C.6: Cusp diagram of the two parameters, (μ_1, μ_2). Inside of the cusp, three equilibria exist, while outside of the cusp, only one is found.

Bibliography

[1] D.M. Anderson and S.H. Davis. Fluid flow, heat transfer, and solidification near tri-junctions. *J. Crystal Growth*, 142(1-2):245–252, 1994.

[2] V. I. Arnold. *Ordinary Differential Equations*. The MIT Press, 1978.

[3] TB Benjamin and JC Scott. Gravity-capillary waves with edge constraints. *J. Fluid Mech.*, 92(2):241–267, 1979.

[4] A.S. Bhandar, M.J. Vogel, and P.H. Steen. Energy landscapes and bistability to finite-amplitude disturbances for the capillary bridge. *Phys. Fluids*, 16:3063, 2004.

[5] A.B. Bichi, W.R. Smith, and J.G. Wissink. Solidification and downstream meniscus prediction in the planar-flow spin casting process. *CES*, 63(3):685–695, 2008.

[6] T.D. Blake. The physics of moving wetting lines. *J. Colloid Interface Sci.*, 299(1):1–13, 2006.

[7] J.B. Bostwick and P.H. Steen. Stability of constrained cylindrical interfaces and the torus lift of Plateau-Rayleigh. *J. Fluid Mech.*, 647:201–219, 2010.

[8] R.A. Brown and L.E. Scriven. On the multiple equilibrium shapes and stability of an interface pinned on a slot. *J. Colloid Interface Sci.*, 78:528–542, 1980.

[9] M. Bussmann, J. Mostaghimi, DW Kirk, and JW Graydon. A numerical study of steady flow and temperature fields within a melt spinning puddle. *Int. J. Heat and Mass Transfer*, 45(19):3997–4010, 2002.

[10] C.J. Byrne. *Planar-flow melt spinning: Process stability and microstructural control*. PhD thesis, Cornell University, 2007.

[11] C.J. Byrne, A.M. Kueck, S.P. Baker, and P.H. Steen. In situ manipulation of cooling rates during planar-flow melt spinning processing. *Mat. Sci. Eng. A*, 459(1-2):172–181, 2007.

[12] C.J. Byrne, E.A. Theisen, B.L. Reed, and P.H. Steen. Capillary puddle vibrations linked to casting-defect formation in planar-flow melt spinning. *Metall. Mater. Trans. B*, 37B:445–456, 2006.

[13] C.J. Byrne, E.A. Theisen, B.L. Reed, and P.H. Steen. Capillary puddle vibrations linked to casting-defect formation in planar-flow melt spinning. *Metall. Mater. Trans. B*, 37B:445–456, 2006.

[14] C.J. Byrne, S.J. Weinstein, and P.H. Steen. Capillary stability limits for liquid metal in melt spinning. *CES*, 61(24):8004–8009, 2006.

[15] B. Cantor and K. O'Reilly. *Solidification and casting*. Taylor & Francis, 2003.

[16] J.K. Carpenter. *Processing of molten metals by planar flow spin casting: modelling and experiments*. PhD thesis, Cornell University, 1990.

[17] J.K. Carpenter and P.H. Steen. On the heat transfer to the wheel in planar-flow melt spinning. *Metall. Trans. B*, 21B:279–283, 1990.

[18] J.K. Carpenter and P.H. Steen. Planar-flow spin-casting of molten metals: process behaviour. *J. Mater. Sci.*, 27(1):215–225, 1992.

[19] J.K. Carpenter and P.H. Steen. Heat transfer and solidification in planar-flow melt-spinning: high wheelspeeds. *Int. J. Heat Mass Tran.*, 40(9):1993–2007, 1997.

[20] K.N. Christodoulou and L.E. Scriven. The fluid mechanics of slide coating. *J. Fluid Mech.*, 208:321–354, 1989.

[21] M.G. Chu, A. Giron, and D.A. Granger. Microstructure and heat flow in melt-spun aluminum alloys. In *Rapidly Solidified Materials: Proceedings of an International Conference, San Diego, California, USA, February 3-5, 1986*. ASM, 1986.

[22] A. Clarke. Coating on a rough surface. *AIChE J.*, 48(10):2149–2156, 2002.

[23] S.H. Davis. Moving contact lines and rivulet instabilities. Part 1. The static rivulet. *J. Fluid Mech.*, 98:225–242, 1980.

[24] P.G. de Gennes. Wetting: statics and dynamics. *Rev. Mod. Phys.*, 57(3):827–863, 1985.

[25] F. Durst and H. Wagner. *Liquid film coating*, chapter Slot coating, pages 401–426. Champan & Hall, 1997.

[26] E.B. Dussan. On the spreading of liquids on solid surfaces: static and dynamic contact lines. *Ann. Rev. Fluid Mech.*, 11(1):371–400, 1979.

[27] J. Eggers, J. Meunier, and E. Rolley. Wetting and spreading. *Rev. Mod. Phys.*, 81(2):739–805, 2009.

[28] Y.C. Fung and P. Tong. *Classical and Computational Solid Mechanics*. World Scientific, 2001.

[29] A.G. Gillen and B. Cantor. Photocalorimetric cooling rate measurements on a ni-5wtreapidly solidified by melt spinning. *Acta Metall.*, 33(10):1813, 1985.

[30] Z. Gong, P. Wilde, and E. Matthys. Numerical modeling of the planar flow melt-spinning process and experimental investigation of its solidification puddle dynamics. *Int. J. Rapid Solid.*, 6:1–28, 1991.

[31] J.B. Grotberg and O.E. Jensen. Biofluid mechanics in flexible tubes. *Annu. Rev. Fluid Mech.*, 36:121–147, 2004.

[32] R. Hasegawa. Present status of amorphous soft magnetic alloys. *J. Mag. Magn. Mater.*, 215:240–245, 2000.

[33] R. Hasegawa and D. Azuma. Impacts of amorphous metal-based transformers on energy efficiency and environment. *J. Mag. Magn. Mater.*, 320(20):2451–2456, 2008.

[34] J.E. Hatch. *Aluminum: properties and physical metallurgy*. Asm Intl, 1984.

[35] G. Herzer. Magnetic materials for electronic article surveillance. *J. Mag. Magn. Mater.*, 254:598–602, 2003.

[36] B.G. Higgins and L.E. Scriven. Capillary pressure and viscous pressure drop set bounds on coating bead operability. *CES*, 35(3):673–682, 1980.

[37] S.C. Huang. The effect of melt delivery conditions on the casting of amorphous metal ribbons. In *Proceedings of the Fourth International Conference on Rapidly Quenched Metals: Sendai, Japan, August 24-28, 1981*. The Japanese Institute of Metals, 1982.

[38] T. Ibaraki. *Fluid and heat flow in planar-flow melt-spinning*. PhD thesis, Cornell University, 1996.

[39] T. Ibaraki and P.H. Steen. *Melt-Spinning, Strip Casting and Slab Casting*, chapter Fluid and heat flow in planar-flow melt-spinning: Experiments and modeling, pages 159–171. TMS, 1996.

[40] M. Kahn. Unsteady behavior of the planar flow spin-casting process. Master's thesis, Cornell University, 2001.

[41] C. Karcher and P.H. Steen. High-Reynolds-number flow in a narrow gap driven by solidification. I. Theory. *Phys. Fluids*, 13:826, 2001.

[42] C. Karcher and P.H. Steen. High-Reynolds-number flow in a narrow gap driven by solidification. II. Planar-flow casting application. *Phys. Fluids*, 13:834, 2001.

[43] S. Kavesh. Principles of Fabrication(of Metallic Glasses). In J.J. Gillman and Leamy H.J., editors, *Metallic Glasses. ASM, Metals Park, Ohio. 1978*, pages 36–73, 1978.

[44] S.F. Kistler and P.M. Schweizer. *Liquid film coating*. Chapman & Hall London, 1997.

[45] J. Kukura, K. Ford, A. Singh, P.H. Steen, and T. Ibaraki. *Simulations of Materials Processing: Theory, Methods, and Applications*, chapter Measurement

of heat transfer coefficient in planar flow casting, pages 1153–1157. Balkema, 1995.

[46] G. Li and B. Thomas. Transient thermal model of the continuous single-wheel thin-strip casting process. *Met. Mater. Trans. B*, 27B(3):509–525, 1996.

[47] H. Liebermann. Casting in an exothermic reducing flame atmosphere, 1986.

[48] HH Liebermann. Ribbon-substrate adhesion dynamics in chill block melt-spinning processes. *Metall. Trans. B*, 15B:155–161, 1984.

[49] C.A. López and A.H. Hirsa. Fast focusing using a pinned-contact oscillating liquid lens. *Nature Photonics*, 2(10):610–613, 2008.

[50] B.J. Lowry and D.B. Thiessen. Fixed contact line helical interfaces in zero gravity. *Phys. Fluids*, 19:022102, 2007.

[51] R.E. Maringer. Solidification on a substrate. *Mat. Sci. Eng.*, 98:13–20, 1988.

[52] DH Michael. Meniscus stability. *Annu. Rev. Fluid Mech.*, 13(1):189–216, 1981.

[53] H. Mühlbach, G. Stephani, R. Sellger, and H. Fielder. Cooling rate and heat=transfer coefficient during planar flow casting of microcrystalline steel ribbons. *Int. J. Rapid Solid.*, 3(2):83–94, 1987.

[54] A.D. Myshkis, V.G. Babskii, N.D. Kopachevskii, L.A. Slobozhanin, A.D. Tyuptsov, and R.S. Wadhwa. *Low-gravity fluid mechanics*. Springer, 1987.

[55] M.C. Narasimhan. Continuous casting method for metallic strips, 1979. US Patent 4,142,571.

[56] Y. Ogawa, M. Naoe, Y. Yoshizawa, and R. Hasegawa. Magnetic properties of high Bs Fe-based amorphous material. *J. Mag. Magn. Mater.*, 304(2):e675–e677, 2006.

[57] R. L. Panton. *Incompressible Flow*. Wiley, 2005.

[58] A.R. Paul, P. Roy, and S. Mukherjee. *Mechanical Sciences: Engineering Mechanics and Strength of Materials*. PHI Learning, 2005.

[59] C. Pozrikidis. Inviscid drops with internal circulation. *J. Fluid Mech.*, 209:77–92, 1989.

[60] T.J. Praisner, J.S.J. Chen, and A.A. Tseng. An experimental study of process behavior in planar flow melt spinning. *Metall. Mater. Trans. B*, 26(1):1199–1208, 1995.

[61] N.H. Pryds and J.H Hattel. Numerical modelling of rapid solidification. *Modelling Simul. Mater. Sci. Eng.*, 5:451–472, 1997.

[62] L. Rayleigh. On the capillary phenomenon of jets. *Proc. R. Soc. Lond.*, 29:71–97, 1879.

[63] B. Reed. *Planar-flow spin casting: momentum transport, vorticity transport, and texture formation*. PhD thesis, Cornell University, 2001.

[64] B.L. Reed, A.H. Hirsa, and P.H. Steen. Vorticity transport in solidification boundary layers. *J. Fluid Mech.*, 426:397–406, 2001.

[65] O.J. Romero, LE Scriven, and M.S. Carvalho. Effect of curvature of coating die edges on the pinning of contact line. *AIChE journal*, 52(2):447–455, 2006.

[66] R.V. Roy and L.W. Schwartz. On the stability of liquid ridges. *J. Fluid Mech.*, 391:293–318, 1999.

[67] K.J. Ruschak. Limiting flow in a pre-metered coating device. *CES*, 31(11):1057–1060, 1976.

[68] K.J. Ruschak. Coating flows. *Ann. Rev. Fluid Mech.*, 17(1):65–89, 1985.

[69] H. Schlichting. *Boundary Layer Theory.* McGraw-Hill Series in Mechanical Engineering, 1960.

[70] L.W. Schwartz, H.M. Princen, and A.D. Kiss. On the motion of bubbles in capillary tubes. *J. Fluid Mech.*, 172:259–275, 1986.

[71] P.H. Steen, J.K. Carpenter, and H. Yu. Fluid mechanics of the planar-flow melt-spinning process. *AIChE J.*, 34(10):1673–1682, 1988.

[72] P.H. Steen and C. Karcher. Fluid Mechanics of Spin Casting of Metals. *Ann. Rev. Fluid Mech.*, 29:373–397, 1997.

[73] P.H. Steen and C. Karcher. Fluid mechanics of spin casting of metals. *Annu. Rev. Fluid Mech.*, 29:373–397, 2003.

[74] K. Takeshita and P.H. Shingu. Thermal contact during the cooling by the single roller chill block casting. *Trans. Jpn. Inst. Met.*, 27(6):454–462, 1986.

[75] E.A. Theisen. *Transient behavior of the planar-flow melt spinning process with capillary dynamics.* PhD thesis, Cornell University, 2007.

[76] E.A. Theisen, M.J. Davis, S.J. Weinstein, and P.H. Steen. Transient behavior of the planar-flow melt spinning process. *CES*, 65(10):3249–3259, 2010.

[77] E.A. Theisen, M.J. Vogel, C.A. López, A.H. Hirsa, and P.H. Steen. Capillary dynamics of coupled spherical-cap droplets. *J. Fluid Mech.*, 580:495–505, 2007.

[78] J.M.T. Thompson and H.B. Stewart. *Nonlinear Dynamics and Chaos*. John Wiley & Sons Inc, 2002.

[79] G.M. Tierny. Planar flow melt spinning: Process operability and liquid puddle dynamics. Master's thesis, Cornell University, 1993.

[80] J.A. Tsamopoulos and R.A. Brown. Nonlinear oscillations of inviscid drops and bubbles. *J. Fluid Mech.*, 127:519–537, 1983.

[81] M.J. Vogel, P. Ehrhard, and P.H. Steen. The electroosmotic droplet switch: Countering capillarity with electrokinetics. *Proc. Natl. Acad. Sci.*, 102(34):11974, 2005.

[82] M.J. Vogel and P.H. Steen. Capillary-based switchable adhesion. *Proc. Natl. Acad. Sci.*, 107(8):3377–3381, 2010.

[83] G.-X. Wang and E. Matthys. Mathematical simulation of melt flow, heat transfer and non-equilibrium solidification in planar-flow casting. *Mod. Sim. in Mat. Sci. Eng.*, 10:35–55, 2002.

[84] S.J. Weinstein and K.J. Ruschak. Coating flows. *Ann. Rev. Fluid Mech.*, 36(1):29–53, 2004.

[85] MM Weislogel and S. Lichter. A spreading drop in an interior corner- Theory and experiment. *Microgravity Sci. Tech.*, 9(3):175–184, 1996.

[86] X. Yin and S. Kumar. Lubrication flow between a cavity and a flexible wall. *Phys. Fluids*, 17:063101, 2005.

[87] Daniel Zwillinger. *CRC Standard Mathematical Tables and Formulae*, volume 31. CRC Press, 2003.